Università di Pavia
Dottorato di ricerca in Fisica - Ciclo XXXVIII

Interferometric Couplers for the Control of Quantum Light in Integrated Resonators

Alice Viola

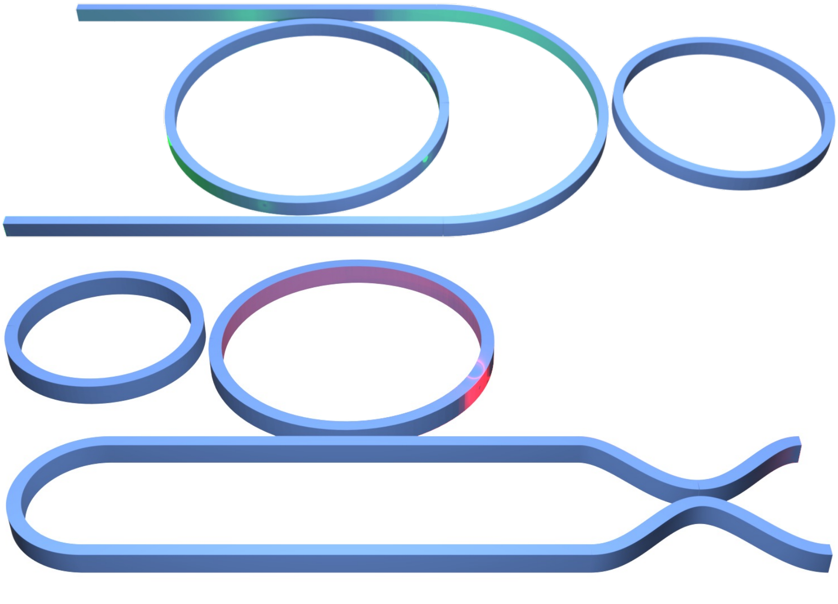

Tesi per il conseguimento del titolo

UNIVERSITÀ
DI PAVIA

Università degli Studi di Pavia
Dipartimento di Fisica

DOTTORATO DI RICERCA IN FISICA - XXXVIII CICLO

Interferometric Couplers for the Control of Quantum Light in Integrated Resonators

Alice Viola

Submitted to the Graduate School of Physics in partial
fulfillment of the requirements for the degree of
DOTTORESSA DI RICERCA IN FISICA
DOCTOR OF PHILOSOPHY IN PHYSICS
at the
University of Pavia

Supervisor: Marco Liscidini

Cover: Illustration of two resonant interferometric couplers.

Interferometric Couplers for the Control of Quantum Light in Integrated Resonators
Alice Viola
PhD thesis - University of Pavia
Pavia, Italy, 2025

A mia Madre, Davide e mio Padre.
Ciascuno di loro mi ha dato
i due schiaffi di cui avevo bisogno
per capire che salute, affetti, e gioia
valgono più di ogni bel lavoro
prima che affogassi sotto questa tesi.

Abstract

Nonclassical states of light are an essential resource for quantum technologies. Yet, practical applications demand reconfigurable, low-loss integrated sources to support the large-scale deployment of these technologies. In this thesis, we explore how integrated ring resonators and interferometric couplers enable precise control in quantum light generation. We start by critically reviewing and developing theoretical models for on-chip quantum light generation. Within this framework, we design a Mach-Zehnder resonant interferometric coupler that selectively tunes the quality factor of individual ring resonances. This enables optimized spontaneous four-wave mixing, producing high-purity heralded single photons in a single-pump configuration and high-gain degenerate squeezing in a dual-pump setting. The device is further refined by selecting materials and geometries that enhance the nonlinearity while balancing dispersion and losses. Beyond squeezed light generation, the same coupler architecture is adapted to investigate bound states in the continuum, demonstrating its versatility. Finally, we introduce a Sagnac-interferometer-based resonant coupler to control spontaneous single-photon emission from a dipole, illustrating the broad potential of resonant interferometric coupling strategies in quantum photonics.

Contents

Introduction

Integrated photonic circuits are emerging as a promising platform for quantum technologies. The ability of integrated resonators to confine light in both space and time enhances light-matter interactions while maintaining scalability and compactness. This makes them a viable candidate for generating nonclassical states of light, with applications ranging from quantum computing and secure communications to precise metrology and sensing. However, the practical realization of high-purity quantum light sources, such as squeezed states or single photons, remains constrained by fundamental limitations in conventional resonator designs, including parasitic nonlinear processes, losses, and restricted tunability.

In this thesis, we will address these challenges by introducing novel interferometric coupler architectures that mitigate the constraints of traditional resonator systems. Alongside these designs, we will develop a theoretical framework for modeling quantum light generation in nonlinear integrated resonators, which will enable the quantitative evaluation of nonclassical light sources under realistic conditions.

In Chapter 1, we will set a theoretical framework for modeling integrated photonic circuits, employing a scattering matrix formalism to analyze essential building blocks for our designs. Ring resonators confine light on resonance, enhancing light-matter interaction and increasing the efficiency of nonlinear quantum processes; Mach-Zehnder interferometers provide reconfigurable routing and precise interference control of optical fields; while Sagnac interferometers enable interactions between counterpropagating modes. To model quantum light generation, we will review the quantization of the electromagnetic field, accounting for nonlinearities and dispersion in integrated structures.

Focusing on the generation of squeezed states via spontaneous four-wave mixing, in Chapter 2, we will review the properties of squeezed light and present three complementary methods to compute generation rates, squeezing levels, and spectral correlations. The first method relies on a Lorentzian approximation of the ring resonances, yielding accurate numerical results in both low- and high-gain regimes, provided that losses, noise, or interactions between different modes do not degrade the resonance shape. The second method expands the fields on a complete basis of modes that are solutions to Maxwell's equations in the absence of quantum or nonlinear interactions. This decomposition separates the description of linear classical propagation from that of quantum dynamics, yielding analytical results in the low-gain regime even for split or noisy resonances. We will combine the strengths of these two approaches into a *local-fields formalism*. By performing a change of basis from the asymptotic fields to a set of modes that are spectrally restricted to individual ring resonances and spatially confined to small sections of the resonator, the local-fields approach renders the full equations of motion numerically tractable, enabling accurate predictions across both low- and high-gain regimes for a broad class of integrated devices.

A major challenge in generating quantum light with conventional ring resonators arises from their identical resonances. On the one hand, the resulting spontaneous four-wave mixing process lacks spectral tunability, limiting the purity of heralded single photons to 93%. On the other hand, in the high-gain regime, unwanted ring resonances enhance parasitic processes, introducing noise that limits the squeezing to 3 dB. To overcome these constraints, in Chapter 3, we will introduce a *Mach-Zehnder resonant interferometric coupler*, an architecture combining two ring resonators with a Mach-Zehnder interferometer. This structure, achieves selective control over the linewidths of individual resonances, enabling precise tuning of the spectral correlations in the generated state. Experimental results confirm this enhanced control, showing a heralded single-photon purity up to 98.67%. We will then move to the high-gain regime, proposing a reconfigured setup of the MZ-RIC that selectively suppresses the unwanted resonances, yielding a squeezing level of 6.49 dB.

In Chapter 4, we will further refine this design by addressing platform optimization. By using finite-difference time-domain simulations to study dispersion engineering, propagation losses, and backscattering as functions of waveguide geometry and sidewall roughness, we will develop a design methodology that balances performance metrics, such as generation rate and extraction efficiency, against practical fabrication constraints.

In Chapter 5, still building on the Mach-Zehnder interferometric coupler architecture, we will also explore the realization of bound states in the continuum. By decouplig a single resonance, we will propose a method to create and study a bound state in a spontaneous four-wave mixing experiment. This configuration will allow one photon from a pair to remain detectable while remaining correlated to its confined companion. We will adapt the asymptotic-field formalism to include dark modes, enabling the calculation of generation rates in the presence of a bound state in the continuum.

Beyond spontaneous four-wave mixing, in Chapter 6, we will explore a distinct quantum process: spontaneous emission from a dipole embedded in a resonator. Using the asymptotic-field formalism, we will first recover the results of the Purcell effect and then extend the treatment beyond conventional cavity quantum electrodynamics, demonstrating enhanced emission rates even for non-Lorentzian resonances. An analysis of backscattering reveals that, beyond the expected reduction in the rate due to losses, a controlled interaction between counterpropagating fields can direct photon emission into specific modes. To harness this effect, we will introduce a *Sagnac resonant interferometric coupler*, which leverages the natural interference between clockwise and counterclockwise modes in a Sagnac loop to select the emission mode and rate.

The theoretical and practical developments presented in the following chapters will provide a foundation for understanding and optimizing quantum light generation in integrated photonic platforms.

Chapter 1

Modeling Photonic Circuits for Quantum Light Control

Before exploring the design of interferometric couplers for quantum light generation, it is essential to understand the fundamental physics governing both linear and nonlinear light propagation in integrated structures. Photonic integrated circuits (PICs) are a cornerstone technology for manipulating and processing light by combining multiple optical components onto a single substrate. The concept was first proposed by Miller in 1969 [1], who envisioned the possibility of creating optical circuits analogous to electronic integrated circuits.

Today, the field has evolved to integrate thousands of photonic components on single chips [2], with the ultimate goal being the realization of large-scale, optical systems that leverage the scalability and cost effectiveness of Complementary Metal-Oxide-Semiconductor (CMOS) fabrication processes [3]. PICs find applications in high-bandwidth interconnects for data centers [4], optical sensors [5], and photonic computing [6]. Additionally, the ability to confine light to wavelegth and subwavelength dimensions enhances light-matter interactions, enabling efficient processes which are crucial for quantum technologies [7, 8].

In this chapter, we define a theoretical framework to model both the classical propagation of light through PICs and the quantum mechanical nature of light-matter interactions. In the first section, we examine the basic building blocks of photonic circuits and introduce a scattering matrix formalism that enables the analysis of complex integrated circuits. In the second section, we discuss the quantization of the electromagnetic field in integrated optical systems, accounting for material nonlinearities, dispersion, and optical confinement consistently.

1.1 Linear Photonic Integrated Circuits

The behaviour of PICs can be modeled by decomposing them into their fundamental building blocks. Among these, waveguides form the backbone of many photonic circuits, providing the optical interconnects that route light between different functional elements. One of the most common waveguide layouts is ridge waveguides, which are strips composed of a core with rectangular, trapezoidal, or round cross-section, which is surrounded by a cladding made of a different material. One simple configuration is depicted in figure Fig. 1.1. The refractive index of the core material is higher than that of the cladding, and both materials are transparent at the operating wavelength. Light is confined inside the core, due to total internal reflection, which is made possible by the index contrast between the two materials.

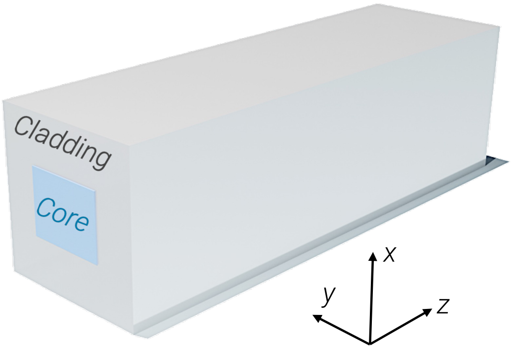

Figure 1.1: Sketch of a ridge waveguide.

Modeling the propagation of light inside an integrated waveguide ultimately reduces to solving Maxwell's equations:

$$\begin{aligned} \nabla \cdot \mathbf{D}(\mathbf{r},t) &= 0, & \frac{\partial \mathbf{B}}{\partial t} &= -\nabla \times \mathbf{E}(\mathbf{r},t), \\ \nabla \cdot \mathbf{B}(\mathbf{r},t) &= 0, & \frac{\partial \mathbf{D}}{\partial t} &= \nabla \times \mathbf{H}(\mathbf{r},t), \end{aligned} \tag{1.1}$$

under the boundary conditions imposed by the waveguide geometry. Here **D** is the displacement field, **E** the electric field, **B** the magnetic field, and **H** the magnetizing field at position $\mathbf{r} = (x, y, z)$ and time t. We are neglecting any free charges or currents.

Analytical solutions are available only for very simple geometries with high confinement in the core region. In general, one needs numerical methods such as finite-difference time domain or guided-mode expansion to solve Maxwell's equations for the desired structure. In principle, the full three-dimensional solution can be obtained exactly for any geometry. However, these methods are computationally intensive and quickly become impractical when scaling up the number of waveguides.

A different approach is to consider a solution of the form:

$$\mathbf{E}(\mathbf{r},t) = \mathbf{E}(x,y)\bar{A}(z)e^{i(kz-\omega t)}, \tag{1.2}$$

where $\mathbf{E}(x, y)$ represents the transverse mode profile, and $\bar{A}(z)$ is the slowly varying amplitude along the propagation direction z, ω is the angular frequency, and k is the corresponding wavevector which, in general, depends on ω. In a sufficiently narrow bandwidth, one can expand the k in a Taylor series around a central frequency ω_0:

$$k(\omega) = \frac{n_{\text{eff}}}{c}\omega_0 + \frac{n_g}{c}(\omega - \omega_0) + \frac{\text{GVD}}{2}(\omega - \omega_0)^2 \tag{1.3}$$

where n_{eff} is the effective index of the fundamental mode at the central frequency, n_g is the group index, and GVD represents the group velocity dispersion. The group index determines the group velocity $v_g = c/n_g$, which quantifies how fast an optical pulse propagates along the waveguide, while the GVD parameter characterizes how this propagation speed varies with frequency. When GVD > 0 (normal dispersion), the group index increases with frequency, meaning higher frequency components propagate more slowly. Conversely, when GVD < 0 (anomalous dispersion), the group index decreases with frequency, so higher frequency components propagate faster.

In a real waveguide, the amplitude $\bar{A}(z)$ can vary in space due to several factors: material absorption, scattering from surface roughness, radiation losses, and undesired coupling to other guided modes. These effects can be understood as optical losses with an overall power attenuation coefficient α, such that a propagation from an initial point z_0 for a length L is described by

$$\bar{A}(z_0 + L) = \bar{A}(z_0)e^{-\frac{\alpha}{2}L}. \tag{1.4}$$

The dephasing e^{ikz} from Eq. (1.2) can be incorporated in this treatment by defining a complex amplitude $A(z) := \bar{A}(z)\mathrm{e}^{ikz}$, and a complex wavevector $\tilde{k} := k + i\frac{\alpha}{2}$. According to Eq. (1.4), the complex amplitude evolves as

$$A(z_0 + L) = A(z_0)e^{i\tilde{k}L}. \tag{1.5}$$

The separation of transverse and longitudinal field profile in Eq. (1.3) allows one to first solve Maxwell's equations in two dimensions to determine the transverse mode profile $\mathbf{E}(x, y)$, which is then considered fixed. Subsequently, one can compute the evolution of the longitudinal amplitude $A(z)$ according to Eq. (1.5).

In general, waveguides in a PIC might be curved. In this case, one can still use Eq. (1.5), by introducing a local set of coordinates (ρ, y, ζ), where at each point ζ is aligned to the direction of the waveguide, y is normal to the plane of the PIC, and ρ is the remaining coordinate. In general, there is a mode mismatch between a straight and a bent waveguide. This causes the curved waveguide to have different dispersion and loss properties.

When two waveguides are positioned close enough that there is overlap between their evanescent fields, one has a directional coupler, with some power transfer between the two guides. For single-mode, homogeneous waveguides with the same mode profile and negligible losses in the coupling region, the evolution of the field amplitudes A_1 and A_2 along the coupling length between waveguides 1 and 2 is governed by the coupled-mode equations:

$$\begin{cases} \frac{dA_1}{dz} & = -ic_{12}A_2(z) \\ \frac{dA_2}{dz} & = -ic_{21}A_1(z) \end{cases}, \tag{1.6}$$

where $c_{12} = c_{21}^*$ is the coupling strength, which is determined by the field overlap between the two waveguides and depends on the gap between them. By solving the system Eq. (1.6), one can relate the field amplitudes after a coupler of length Λ to the incoming fields $A_1(0)$ and $A_2(0)$:

$$\begin{cases} A_1(\Lambda) = \cos(|c_{12}|\Lambda)A_1(0) - i\frac{c_{12}}{|c_{12}|}\sin(|c_{12}|\Lambda)A_2(0) \\ A_2(\Lambda) = -i\frac{c_{12}^*}{|c_{12}|}\sin(|c_{12}|\Lambda)A_1(0) + \cos(|c_{12}|\Lambda)A_2(0) \end{cases} \tag{1.7}$$

It is common to define self- and cross-coupling coefficients $\sigma(\Lambda) = \cos(|c_{12}|\Lambda)$ and $\kappa(\Lambda) = -\frac{c_{12}}{|c_{12}|}\sin(|c_{12}|\Lambda)$, such that Eq. (1.7) reads:

$$\begin{cases} A_1(\Lambda) = \sigma(\Lambda)A_1(0) + i\kappa(\Lambda)A_2(0) \\ A_2(\Lambda) = i\kappa^*(\Lambda)A_1(0) + \sigma(\Lambda)A_2(0) \end{cases} \tag{1.8}$$

The coupling coefficients represent the probability amplitudes of light remaining in the same waveguide (σ) and light being scattered to the other waveguide (κ) for a given coupler. In the case of a lossless coupler, the relation $|\sigma|^2 + |\kappa|^2 = 1$ holds, representing conservation of energy. If Λ is fixed and much smaller than the lengths of the waveguides composing the circuit, one can treat the directional coupler as an effective point coupler with constant coupling coefficients, where the dependency on the coupler parameters (coupling length, gap distance, and field overlap) is implicit. In addition, κ can be taken real without loss of generality. Under these assumptions, Eq. (1.8) is then conveniently written in matrix form as:

$$\begin{pmatrix} A_1^{\text{out}} \\ A_2^{\text{out}} \end{pmatrix} = \begin{pmatrix} \sigma & i\kappa \\ i\kappa & \sigma \end{pmatrix} \begin{pmatrix} A_1^{\text{in}} \\ A_2^{\text{in}} \end{pmatrix} \tag{1.9}$$

Many passive photonic circuit components can be understood as a set of waveguides coupled to each other. In complex circuits composed of N interconnected couplers with M input gates, it is convenient to adopt a scattering matrix description. One starts by observing that each coupler has four ports: two inputs and two outputs. The field amplitudes at these $4N$ ports characterize the field distribution of the entire structure and can be arranged in a field vector $\mathbf{A}$. The order of the elements of this vector is arbitrary. For instance, in this thesis, we will always identify the couplers' input ports with indices $4n + 1$ and $4n + 2$, and the couplers' output ports with indices $4n + 3$ and $4n + 4$, with n an integer between 0 and $N - 1$ identifying the coupler.

One can then set $2N$ coupling equations based on Eq. (1.9) describing the couplers, and $2N - M$ propagation equations based on Eq. (1.4) describing the waveguide connections between the couplers. Finally, the injected fields at the M input gates of the overall structure set the boundary conditions of the system. In particular, if a field with amplitude f_{in} is injected at the j-th port, one writes $A_j = f_{\text{in}}$. If no field is injected there, then $A_j = 0$. The final system of $4N$ coupled equations with $4N$ unknowns can be written in matrix form:

$$S\mathbf{A} = \mathbf{B}, \tag{1.10}$$

where S is the scattering matrix (S-matrix) representing the system of equations described above, and $\mathbf{B}$ is a vector defining the boundary conditions, i.e., a vector with all zeros except for an element f_{in} corresponding to the input port. The vector $\mathbf{A}$ is then found as:

$$\mathbf{A} = S^{-1}\mathbf{B} \tag{1.11}$$

where the inversion of the S-matrix can be performed numerically or analytically.

We note that, regardless of how we order the fields, all diagonal elements of the S-matrix will be equal to 1, and all off-diagonal elements can only be of the form $-\sigma_\mu$, $-\kappa_\mu$, $-e^{i\tilde{k}_\nu L_\nu}$, or 0, with μ indexing the couplers and ν indexing the waveguide connections. A systematic ordering of the couplers and fields will allow one to identify more symmetries in the S-matrix. For instance, one can divide it into 4×4 blocks, in turn divided into four 2×2 sub-blocks with all diagonal blocks of the form:

$$\begin{pmatrix} 1 & 0 & 0 & 0 \\ 0 & 1 & 0 & 0 \\ -\sigma_\mu & -i\kappa_\mu & 1 & 0 \\ -i\kappa_\mu & -\sigma_\mu & 0 & 1 \end{pmatrix},$$

and all elements like $-e^{i\tilde{k}_\nu L_\nu}$ confined to the upper-right 2×2 sub-blocks. When there is only one input gate, to further simplify the treatment, we introduce the normalization $f_{\text{in}} = 1$. Consequently, $\mathbf{B}$ becomes a vector of the standard basis, and all elements of $\mathbf{A}$ are normalized to the incoming field.

We now apply the scattering matrix formalism to three simple structures that are widely used in integrated optics: the ring resonator, the Mach-Zehnder interferometer, and the Sagnac interferometer. These structures serve as building blocks for more complex photonic circuits and demonstrate how the systematic approach developed above can be used to analyze realistic devices.

1.1.1 Ring Resonator

Ring resonators are among the most versatile components in photonic integrated circuits [9]. In linear applications, they are used as optical filters [10], sensors [11], and modulators [12]. In nonlinear optics, their resonant field enhancement can be exploited to enhance light-matter interactions and increase the efficiency of parametric and quantum processes [13, 14].

A ring resonator is schematically illustrated in Fig. 1.2(a). It consists of a waveguide arranged in a closed loop of length L, which is evanescently coupled to an external waveguide, called the bus waveguide. The cross-coupling coefficient is κ. We consider ring resonators with a minimum bending radius large enough that the effects of bending on the mode profile of the ring waveguide are negligible. In this case, both the ring and the waveguide have the same loss coefficient α and the same wavevector k. Often, the term *ring* resonator refers to devices with a circular loop. However, as far as bending effects are negligible, the scattering matrix treatment we deploy here applies to resonators with loops of arbitrary shape. These kinds of structures are called *racetrack* resonators. Here, when not stated otherwise, we use the two terms as synonyms.

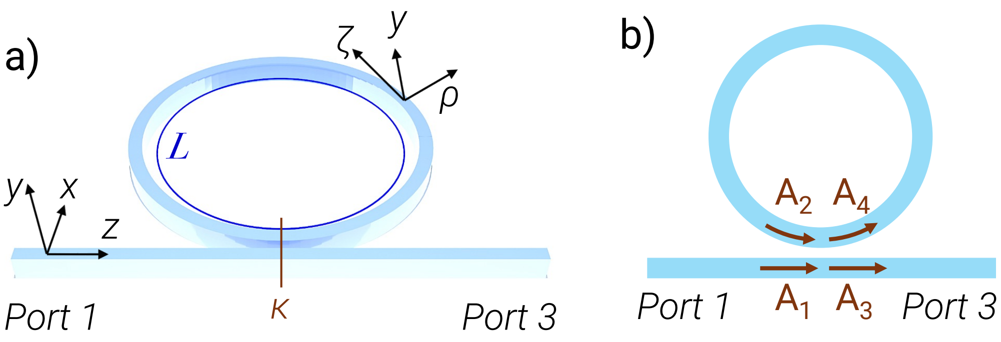

Figure 1.2: Sketches of a ring resonator, indicating (a) the round-trip length L and coupling coefficient κ, along with the two local frames of reference in the bus waveguide (x, y, z) and the ring waveguide (y, ρ, ζ); (b) the four field components used in the scattering matrix calculations.

We define four field amplitudes, as detailed in Fig. 1.2(b): A_1 and A_3 are the input and output fields in the bus waveguide, while A_2 and A_4 represent the fields within the ring immediately before and after the coupling point, respectively. The scattering matrix equations for this system can be constructed from Eqs. (1.5-1.9), assuming light is injected only at port 1:

$$\begin{pmatrix} 1 & 0 & 0 & 0 \\ 0 & 1 & 0 & -e^{i\tilde{k}L} \\ -\sigma & -i\kappa & 1 & 0 \\ -i\kappa & -\sigma & 0 & 1 \end{pmatrix} \begin{pmatrix} A_1 \\ A_2 \\ A_3 \\ A_4 \end{pmatrix} = \begin{pmatrix} 1 \\ 0 \\ 0 \\ 0 \end{pmatrix}. \tag{1.12}$$

Solving Eq. (1.12) yields the transmissivity

$$t = \frac{A_3}{A_1} = \frac{\sigma - e^{i\tilde{k}L}}{1 - \sigma e^{i\tilde{k}L}} \tag{1.13}$$

and field enhancement inside the ring

$$f = \frac{A_4}{A_1} = \frac{i\kappa}{1 - \sigma e^{i\tilde{k}L}}. \tag{1.14}$$

In Fig. 1.3, the transmission $T = |t|^2$ and intensity enhancement $\mathrm{IE} = |f|^2$ of a typical ring resonator are plotted as a function of the natural frequency $\nu = \frac{\omega}{2\pi}$. One can see a comb of equally spaced resonances with maxima in the intensity enhancement and corresponding minima in the transmission. The resonances occurr at frequencies ν_m for which $k(\nu_m)L = 2\pi m$, where m is an integer. The natural frequency spacing between adjacent resonances is called free spectral range (FSR), and, neglecting the GVD, it is equal to

$$\mathrm{FSR} = \frac{c}{n_\mathrm{g} L}. \tag{1.15}$$

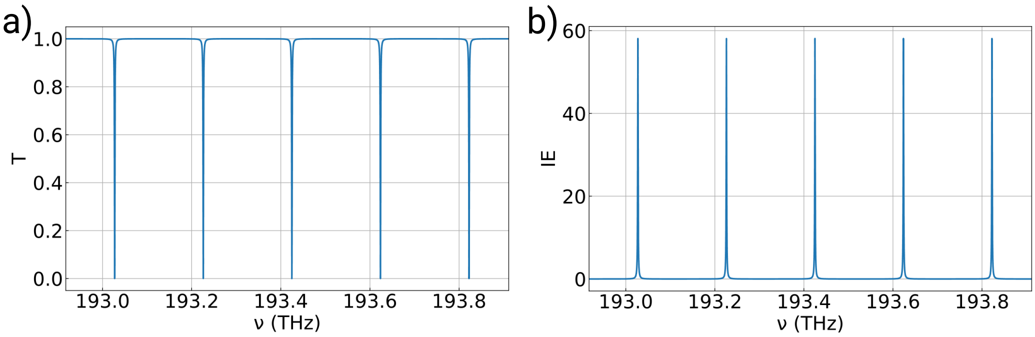

Figure 1.3: (a) Transmission and (b) intensity enhancement of a ring resonator with parameters $n_\mathrm{eff} = 1.7$, $n_g = 2$, GVD$= 0.6$ ps^2/m, $\alpha = 1$ dB/cm, $L = 754$ μm, $\kappa = 0.13$, corresponding to a critical coupling condition.

When the resonance width is much smaller than a free spectral range, the ring resonances have a Lorentzian lineshape, with full width at half maximum

$$\Delta\nu = \frac{2c}{n_g L} \frac{1 - \sigma e^{-\alpha L/2}}{\sqrt{\sigma e^{-\alpha L/2}}}. \tag{1.16}$$

The ring resonators can be classified through their finesse, defined as

$$F = \frac{\mathrm{FSR}}{\Delta\nu}. \tag{1.17}$$

High-finesse ring resonators have a clear Lorentzian lineshape. Low-finesse resonators have either resonances that are separated only by a few linewidths, and thus tend to overlap with each other and modify their shape.

Another figure of merit for a ring resonator is its quality factor, also called the loaded quality factor or Q-factor, and defined as

$$Q_L = \frac{\nu_m}{\Delta\nu} \approx \frac{\pi n_g L}{\lambda_0} \frac{\sqrt{\sigma e^{-\alpha L/2}}}{1 - \sigma e^{-\alpha L/2}}, \tag{1.18}$$

where $\lambda_0 = \frac{2\pi c}{\omega_0}$ is the central wavelength, and we consider ν_m close to the central frequency $\nu_0 = \frac{\omega_0}{2\pi}$. The quality factor represents the number of round-trip lengths a pulse travels in the ring before its energy is reduced to e^{-1} of its original value. This depends on two main loss mechanisms: the intrinsic losses, which are quantified by α, and the coupling to the bus waveguide, which is quantified by σ. For this reason, the loaded quality factor is often decomposed into two parts: the intrinsic quality factor Q_I accounting for material losses, and the coupling quality factor Q_C accounting for coupling losses. The three are related by

$$\frac{1}{Q_L} = \frac{1}{Q_I} + \frac{1}{Q_C} \tag{1.19}$$

and by

$$\eta = \frac{Q_L}{Q_C}, \tag{1.20}$$

where η is the escape efficiency, measuring the probability of a photon within the ring to couple to the bus waveguide.

Based on the relative strength of intrinsic and coupling losses, one can identify three operation regimes for a ring resonator. When $\sigma^2 = e^{-\alpha L}$, the ring is at critical coupling, when $\sigma^2 > e^{-\alpha L}$ it is undercoupled, and when $\sigma^2 < e^{-\alpha L}$ it is overcoupled. In Fig. 1.4 we plot transmission T, intensity enhancement IE, and dephasing $\phi = \arg[t]$ of a single ring resonance in the three regimes. At critical coupling, the resonant transmission drops to zero, while the intensity enhancement reaches its maximum value. In this case, $Q_I = Q_C = 2Q_L$. In the undercoupled regime, the resonances are narrower with smaller intensity enhancement and transmission, reflecting the reduced coupling to the bus waveguide. Conversely, in the overcoupled regime, the resonances become broader due to the stronger coupling that dominates over intrinsic losses. The phase response exhibits different behaviour across the coupling regimes: while all three show a characteristic phase transition across the resonance, the total magnitude of the phase shift is less than π in undercoupling, π at critical coupling, and 2π in overcoupling.

1.1.2 Mach-Zehnder Interferometer

Another widespread element in photonic integrated circuits is the Mach-Zehnder interferometer (MZI). It is a fundamental building block for optical switches [15], modulators [16, 17], filters [18], and wavelength division multiplexing devices [19]. In quantum integrated photonics, MZIs find application as interferometers implementing universal unitary transformations [20, 21] and complex devices handling specific quantum protocols [22, 6].

A Mach-Zehnder interferometer consists of two waveguides that are coupled to each other at two distinct locations, A and B, with cross-coupling coefficients κ_A and κ_B. This configuration is illustrated in Fig. 1.5. The two arms connecting the couplers have lengths $L \pm \frac{\Delta L}{2}$, with L the average length and ΔL the length imbalance.

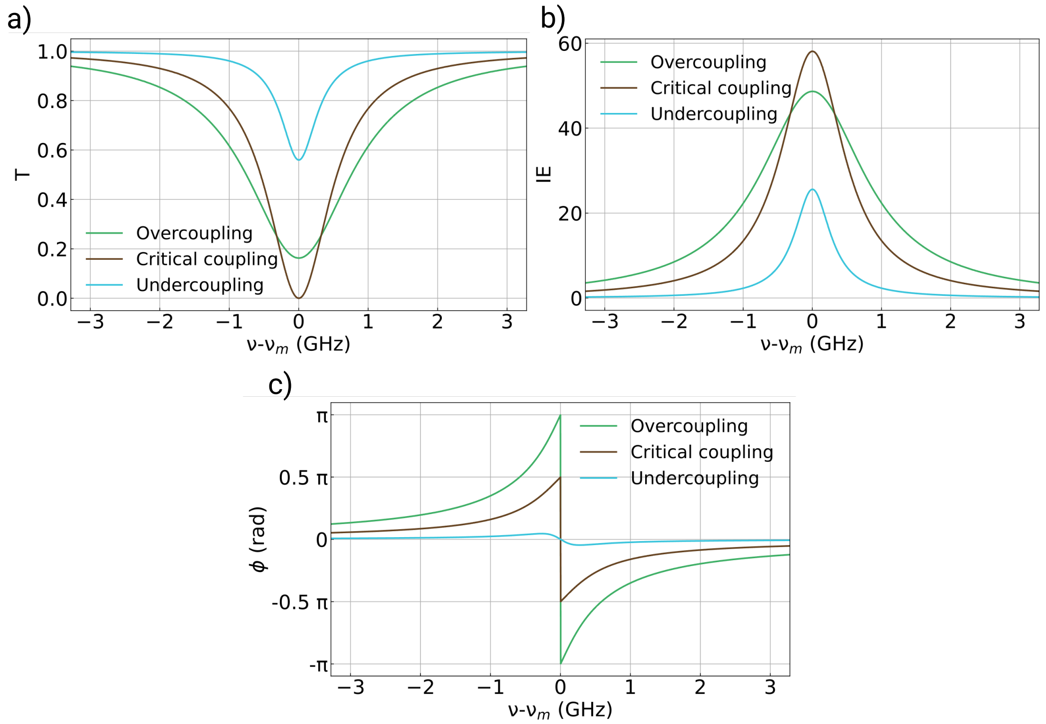

Figure 1.4: Comparison of different coupling regimes of a ring resonator. It is shown the (a) transmission, (b) intensity enhancement, and (c) dephasing of a ring resonance with parameters $n_{\text{eff}} = 1.7$, $n_g = 2$, GVD$= 0.6$ ps^2/m, $\alpha = 1$ dB/cm, $L = 754$ μm. The coupling coefficient is $\kappa = 0.05$ for undercoupling, $\kappa = 0.13$ for critical coupling, and $\kappa = 0.2$ for overcoupling.

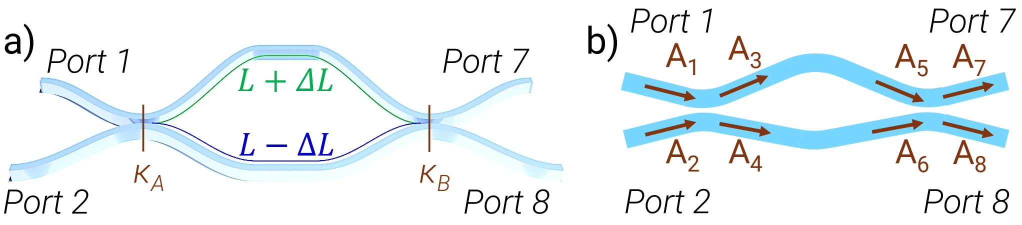

Figure 1.5: Sketches of a Mach-Zehnder interferometer, indicating (a) the arm lengths $L + \frac{\Delta L}{2}$ and $L - \frac{\Delta L}{2}$, along with the coupling coefficients κ_A and κ_B; (b) the eight field components used in the scattering matrix calculations.

The MZI is completely characterized by eight field amplitudes: A_1 and A_2 are the input fields, A_3 and A_4 are the fields after the first coupler, A_5 and A_6 are the fields before the second coupler, and A_7 and A_8 are the output fields, with even indices referring to the lower waveguide, and odd indices referring to the upper one. For light injected only at port 1 ($A_1 = 1$, $A_2 = 0$), the scattering matrix equations become:

$$\begin{pmatrix} 1 & 0 & 0 & 0 & 0 & 0 & 0 & 0 \\ 0 & 1 & 0 & 0 & 0 & 0 & 0 & 0 \\ -\sigma_A & -i\kappa_A & 1 & 0 & 0 & 0 & 0 & 0 \\ -i\kappa_A & -\sigma_A & 0 & 1 & 0 & 0 & 0 & 0 \\ 0 & 0 & -e^{i\tilde{k}(L+\Delta L/2)} & 0 & 1 & 0 & 0 & 0 \\ 0 & 0 & 0 & -e^{i\tilde{k}(L-\Delta L/2)} & 0 & 1 & 0 & 0 \\ 0 & 0 & 0 & 0 & -\sigma_B & -i\kappa_B & 1 & 0 \\ 0 & 0 & 0 & 0 & -i\kappa_B & -\sigma_B & 0 & 1 \end{pmatrix} \begin{pmatrix} A_1 \\ A_2 \\ A_3 \\ A_4 \\ A_5 \\ A_6 \\ A_7 \\ A_8 \end{pmatrix} = \begin{pmatrix} 1 \\ 0 \\ 0 \\ 0 \\ 0 \\ 0 \\ 0 \\ 0 \end{pmatrix}. \tag{1.21}$$

Solving this system yields the transmitted amplitudes:

$$A_7 = \sigma_A \sigma_B e^{i\tilde{k}(L+\Delta L/2)} - \kappa_A \kappa_B e^{i\tilde{k}(L-\Delta L/2)}, \tag{1.22}$$

$$A_8 = i\sigma_A \kappa_B e^{i\tilde{k}(L+\Delta L/2)} + i\kappa_A \sigma_B e^{i\tilde{k}(L-\Delta L/2)}. \tag{1.23}$$

In the simplest case, when $\kappa_A = \kappa_B = \frac{1}{\sqrt{2}}$, the transmittivities simplify to:

$$A_7 = \frac{1}{2} e^{i\tilde{k}L} \left(e^{i\tilde{k}\Delta L/2} - e^{-i\tilde{k}\Delta L/2} \right) = i e^{i\tilde{k}L} \sin\left(\frac{\tilde{k}\Delta L}{2} \right), \tag{1.24}$$

$$A_8 = \frac{i}{2} e^{i\tilde{k}L} \left(e^{i\tilde{k}\Delta L/2} + e^{-i\tilde{k}\Delta L/2} \right) = i e^{i\tilde{k}L} \cos\left(\frac{\tilde{k}\Delta L}{2} \right). \tag{1.25}$$

The power transmission to each output has a sinusoidal dependence on the phase difference between the arms: $|A_7|^2 = \sin^2(\frac{\tilde{k}\Delta L}{2})$ and $|A_8|^2 = \cos^2(\frac{\tilde{k}\Delta L}{2})$. This behaviour is illustrated in Fig. 1.6a. The two outputs oscillate between 0 and 1 with a π dephasing between them, ensuring energy conservation. Neglecting the GVD, the oscillation frequency is constant, equal to $\nu = \frac{c}{n_g L}$. When taking into account a small normal dispersion of GVD $= 0.6$ ps^2/m, the periodicity is broken and the distance between two maxima decreases with the frequency.

When a different splitting ratio is employed for the couplers ($\kappa_A = \kappa_B \neq 1/\sqrt{2}$), the response remains sinusoidal, with the same phase and period, but with reduced visibility. In Fig. 1.6(b), the device response is plotted with $\kappa_A = \kappa_B = 0.48$; the maximum of $|A_7|^2$ and the minimum of $|A_8|^2$ remain at 1 and 0, respectively, but the amplitude of both oscillations is reduced. Transmissions oscillating between arbitrary values in the interval $[0, 1]$ can be obtained with unbalanced couplers. For instance in Fig. 1.6(c) the response with $\kappa_A = 0.48$ and $\kappa_B = 0.6$ is plotted. The maxima and minima are shifted with respect to the values of Fig. 1.6(c). These examples illustrate how the MZI can function as a tunable coupler between its two waveguides. By choosing appropriate coupling coefficients, one can set the effective coupling strength at a given frequency.

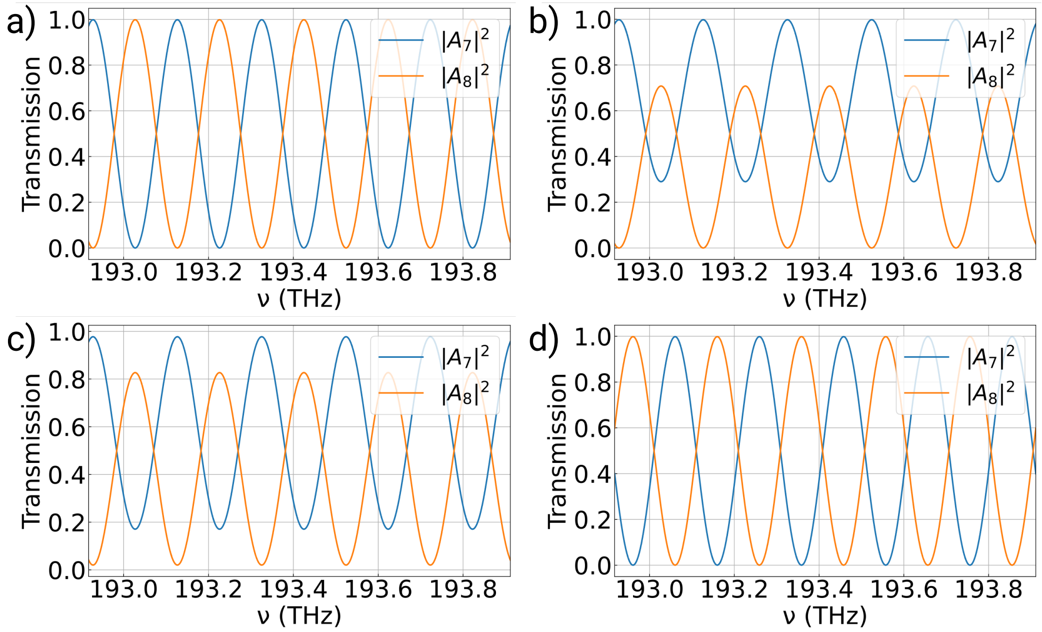

Figure 1.6: Transmission at the two output ports of a few MZI configurations with parameters $n_{\text{eff}} = 1.7$, $n_g = 2$, GVD$= 0.6$ ps^2/m, $\alpha = 0.1$ dB/cm, and $\Delta L = 754$ μm. (a) MZI with symmetric 50:50 couplers $\kappa_A = \kappa_B = \frac{1}{\sqrt{2}}$ and light injected from port 1. (b) MZI with symmetric couplers $\kappa_A = \kappa_B = 0.48$ and light injected from port 1. (c) Unbalanced MZI with $\kappa_A = 0.48$, $\kappa_B = 0.6$ and light injected from port 1. (d) MZI with symmetric 50:50 couplers $\kappa_A = \kappa_B = \frac{1}{\sqrt{2}}$, but $\frac{1}{4}$ of the power injected from port 1 and $\frac{3}{4}$ from port 2.

Besides the single-input transmission, the scattering matrix formalism also enables the description of the response when light is injected from both ports of the MZI. If a field of amplitude f_1 is injected at port 1 and a field f_2 at port 2, with the power normalization $|f_1|^2 + |f_2|^2 = 1$, the output fields become:

$$A_7 = e^{i\tilde{k}L}\left[f_1\left(\sigma_A\sigma_B e^{\frac{i\tilde{k}\Delta L}{2}} - \kappa_A\kappa_B e^{-\frac{i\tilde{k}\Delta L}{2}}\right) + if_2\left(\kappa_A\sigma_B e^{\frac{i\tilde{k}\Delta L}{2}} + \sigma_A\kappa_B e^{-\frac{i\tilde{k}\Delta L}{2}}\right)\right], \tag{1.26}$$

$$A_8 = e^{i\tilde{k}L}\left[if_1\left(\kappa_A\sigma_B e^{-\frac{i\tilde{k}\Delta L}{2}} + \sigma_A\kappa_B e^{\frac{i\tilde{k}\Delta L}{2}}\right) + f_2\left(\sigma_A\sigma_B e^{-\frac{i\tilde{k}\Delta L}{2}} - \kappa_A\kappa_B e^{\frac{i\tilde{k}\Delta L}{2}}\right)\right]. \tag{1.27}$$

This dual-input scenario is illustrated in Fig. 1.6(d), where $\kappa_A = \kappa_B = \sqrt{0.5}$ as in Fig. 1.6(a), but with 1/4 of the power injected from A_1 and 3/4 from A_2. The transmitted power has been normalized to $|A_1|^2 + |A_2|^2$ by defining $A_1 = \frac{1}{2}$, $A_2 = \frac{\sqrt{3}}{2}$. Here, the maxima and minima remain the same as in the single-input case, but the oscillation acquires a phase shift due to the interference between the two input signals. These expressions demonstrate the applications of the transfer matrix even in complex photonic circuits where multiple input channels are used simultaneously.

1.1.3 Sagnac Interferometer

All the photonic components investigated above were characterized by unidirectional propagation. However, in general, light can travel in both directions in an optical waveguide. One of the simplest structures creating counter-directional propagation in a PIC is the Sagnac interferometer, illustrated in Fig. 1.7(a). It consists of a loop of length L made of a single waveguide coupled to itself with a coupling coefficient κ. Light entering the device is partly self-coupled, entering the loop in the clockwise direction, and partly cross-coupled to the counterclockwise direction. Due to the bidirectional propagation, eight fields, instead of four, are needed to completely characterize the coupler, as is shown in Fig. 1.7(b). We call A_1 and A_2 the input fields at ports 1 and 2, A_3 and A_4 are the fields entering the loop in the clockwise and counterclockwise directions respectively, A_5 and A_6 are the fields that have completed one round trip around the loop and are coupled out to ports 2 and 1 with the output fields called A_7 and A_8 respectively.

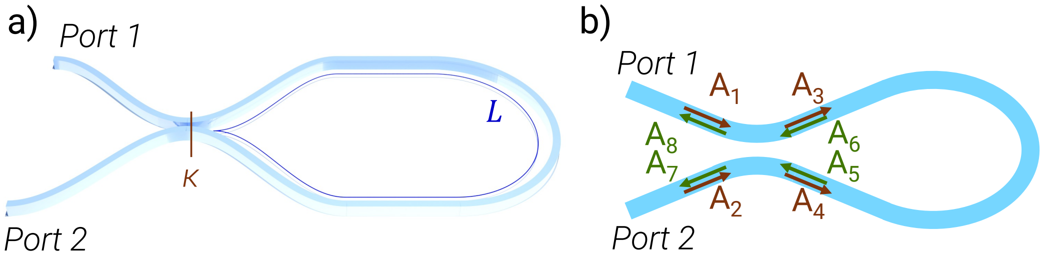

Figure 1.7: Sketches of a Sagnac interferometer, indicating (a) the round-trip length L and the coupling coefficient κ; (b) the eight field components used in the scattering matrix calculations.

For input fields $A_1 = f_1$ and $A_2 = f_2$, the scattering matrix system describing the structure is

$$\begin{pmatrix} 1 & 0 & 0 & 0 & 0 & 0 & 0 & 0 \\ 0 & 1 & 0 & 0 & 0 & 0 & 0 & 0 \\ -\sigma & -i\kappa & 1 & 0 & 0 & 0 & 0 & 0 \\ -i\kappa & -\sigma & 0 & 1 & 0 & 0 & 0 & 0 \\ 0 & 0 & -e^{i\tilde{k}L} & 0 & 1 & 0 & 0 & 0 \\ 0 & 0 & 0 & -e^{i\tilde{k}L} & 0 & 1 & 0 & 0 \\ 0 & 0 & 0 & 0 & -\sigma & -i\kappa & 1 & 0 \\ 0 & 0 & 0 & 0 & -i\kappa & -\sigma & 0 & 1 \end{pmatrix} \begin{pmatrix} A_1 \\ A_2 \\ A_3 \\ A_4 \\ A_5 \\ A_6 \\ A_7 \\ A_8 \end{pmatrix} = \begin{pmatrix} f_1 \\ f_2 \\ 0 \\ 0 \\ 0 \\ 0 \\ 0 \\ 0 \end{pmatrix}. \tag{1.28}$$

Solving this system yields the transmittivities at the two output ports:

$$A_7 = [(\sigma^2 - \kappa^2) f_1 + 2i\sigma\kappa f_2] e^{i\tilde{k}L}, \tag{1.29}$$

$$A_8 = [2i\sigma\kappa f_1 + (\sigma^2 - \kappa^2) f_2] e^{i\tilde{k}L}. \tag{1.30}$$

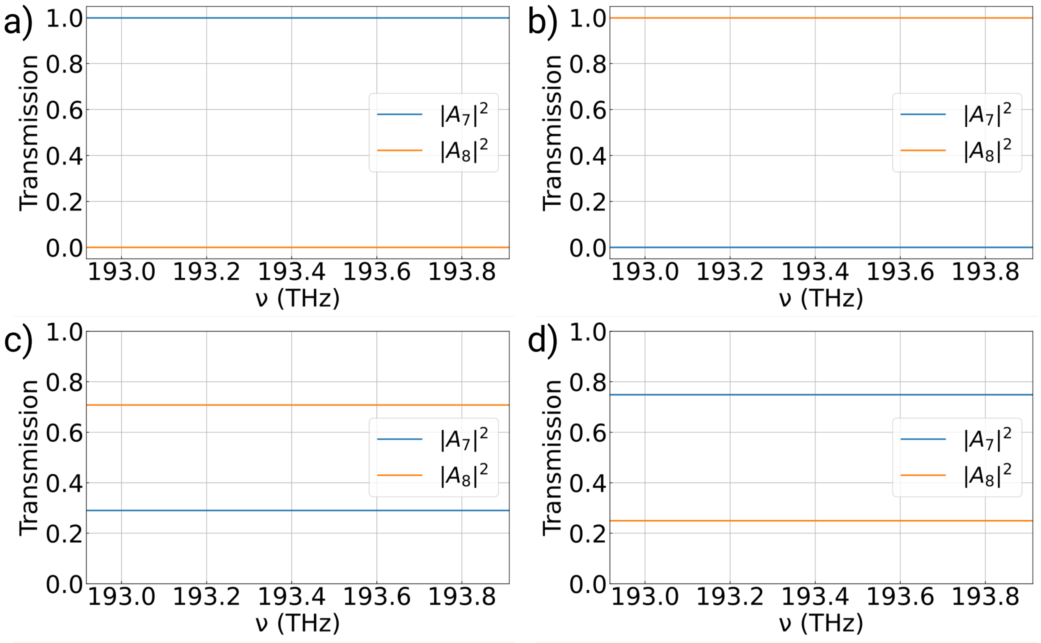

Figure 1.8: Transmission at the two output ports of a few Sagnac configurations with parameters $n_{\text{eff}} = 1.7$, $n_g = 2$, GVD$= 0.6$ ps^2/m, $\alpha = 0.1$ dB/cm, and $L = 754$ μm. (a) $\kappa = 0$, or $\kappa = 1$ and light injected from port 1. (b) $\kappa = \frac{1}{\sqrt{2}}$ and light injected from port 1. (c) $\kappa = 0.48$ and light injected from port 1. (d) $\kappa = \frac{1}{\sqrt{2}}$, but $\frac{1}{4}$ of the power injected from port 1 and $\frac{3}{4}$ from port 2.

The transmissions $|A_7|^2$ and $|A_8|^2$ are illustrated in Fig. 1.8 for a few configurations. Fig. 1.8(a) shows the case where $\kappa = 0$ (or equivalently $\kappa = 1$) with light injected from port 1, resulting in all light being transmitted through the other port with no reflection to port 1. Fig. 1.8(b) demonstrates the balanced 50:50 coupler case ($\kappa = 1/\sqrt{2}$), where all light is reflected back to port 1. Fig. 1.8(c) shows an intermediate coupling strength ($\kappa = 0.48$), resulting in partial transmission to both outputs. Finally, Fig. 1.8(d) illustrates a scenario with $\kappa = 1/\sqrt{2}$ but with 1/4 of the power injected from port 1 and 3/4 from port 2, demonstrating how the input field distribution is important to determine the final output.

These results highlight two fundamental properties of the Sagnac interferometer. First, as with the MZI, choosing the coupling coefficient and the input field distribution allows for tuning the transmitted power at the two output ports. Second, the transmission depends on the coupling ratio but is independent of the optical frequency, because both clockwise and counterclockwise paths accumulate the same phase $\tilde{k}L$, and experience the same coupling strength. This makes the Sagnac interferometer intrinsically balanced and sensitive to any source of non-reciprocity that can introduce an imbalance between the phase accumulated in the clockwise and counterclockwise direction, generating a sinusoidal response similar to the MZI [23]. For this reason, Sagnac interferometers have often been employed in sensing applications. Perhaps, the most prominent examples are fibre-optic and integrated gyroscopes [24, 25, 26, 27], where reciprocity is broken due to mechanical rotations on the plane of the Sagnac loop. Beyond sensing, the intrinsic phase stability of the Sagnac makes it attractive for quantum technologies, such as quantum key distribution [28] and entangled photon-pair generation [29, 30], though currently these implementations remain predominantly in bulk optics rather than integrated platforms. Finally, in classical integrated photonics, Sagnac interferometers serve as building blocks for filters, optical cavities, and wavelength de/multiplexers, often implemented in cascaded configurations of multiple Sagnac elements to achieve more sophisticated spectral responses [31].

1.2 Quantization of the Electromagnetic Field in Integrated Devices

The generation and manipulation of quantum states of light in integrated photonic devices requires a proper theoretical framework for quantizing the electromagnetic field in realistic geometries. Unlike free-space quantization, integrated structures present several challenges: the dielectric waveguide environment is far from the standard box with periodic boundary conditions that is usually assumed when quantizing light in vacuum [32]. Light-matter interactions modify the dispersion and propagation properties of light to the point that some argue it is not even appropriate to talk about photons when dealing with PICs [33]. In this respect, a nonlinear approach to the electromagnetic field quantization was proposed early in 1997 that explicitly treats polaritons as collective excitations of electromagnetic and matter degrees of freedom, at the expense of giving up any straightforward macroscopic treatment of the electromagnetic field [34]. Still, when dealing with transparent media, one can talk about photons instead of polaritons, provided the effects of matter are carefully taken into account in the light dispersion properties, and the macroscopic electromagnetic fields are properly normalized to satisfy the Poynting theorem [33].

A second challenge arises from nonlinear interactions, which are crucial to many quantum applications. It has been shown that in the presence of nonlinear processes, one can not quantize the electromagnetic field starting from the fundamental fields **E** and **B**. In fact, this standard approach would lead to incorrect or intractable expressions for higher-order terms in the Hamiltonian. Such corrections are often negligible, but in some cases they may lead to incorrect quantitative and even qualitative predictions [35]. A more practical macroscopic approach uses the displacement field **D** and magnetic field **B** as the fundamental fields. This choice, originally suggested by Born and Infeld [36], has proved essential for obtaining correct results in quantum nonlinear optics [35] [37]. In this section, we review the theoretical foundation needed to describe quantum light in nonlinear PICs, starting from the **D** and **B** fields, and deriving the nonlinear Hamiltonian.

1.2.1 Linear Treatment

For non-magnetic materials, the constitutive relations are:

$$\mathbf{E}(\mathbf{r},t) = \frac{\mathbf{D}(\mathbf{r},t)}{\varepsilon_0\varepsilon_r(\mathbf{r})}, \qquad \mathbf{H}(\mathbf{r},t) = \frac{\mathbf{B}(\mathbf{r},t)}{\mu_0}, \tag{1.31}$$

where ϵ_0 and μ_0 are the vacuum dielectric and magnetic permittivities, and $\varepsilon_r(\mathbf{r})$ is the position-dependent relative permittivity characterizing the dielectric structure. These are substituted into the energy density of the electromagnetic field, which is given by

$$d\hbar = \mathbf{H}\cdot d\mathbf{B} + \mathbf{E}\cdot d\mathbf{D}, \tag{1.32}$$

to find the classical Hamiltonian:

$$\mathcal{H} = \int_V \left[\frac{\mathbf{B}(\mathbf{r},t)\cdot\mathbf{B}(\mathbf{r},t)}{2\mu_0} + \frac{\mathbf{D}(\mathbf{r},t)\cdot\mathbf{D}(\mathbf{r},t)}{2\varepsilon_0\varepsilon_r(\mathbf{r})}\right] d^3\mathbf{r}, \tag{1.33}$$

where V is the quantization volume defined according to the structure of interest.

The canonical quantization procedure promotes the fields to operators with equal-time commutation relations:

$$[\hat{D}_i(\mathbf{r}), \hat{D}_j(\mathbf{r}')] = 0, \tag{1.34}$$

$$[\hat{B}_i(\mathbf{r}), \hat{B}_j(\mathbf{r}')] = 0, \tag{1.35}$$

$$[\hat{D}_i(\mathbf{r}), \hat{B}_j(\mathbf{r}')] = i\hbar\varepsilon_{ijk}\frac{\partial}{\partial r_k}\delta(\mathbf{r}-\mathbf{r}'), \tag{1.36}$$

where ε_{ijk} is the Levi-Civita tensor. These commutation relations ensure that the quantum field operators satisfy Maxwell's equations through the Heisenberg equations of motion.

The field operators are usually expanded in terms of a set of discrete modes labeled by index m:

$$\hat{\mathbf{D}}(\mathbf{r},t) = \sum_m \sqrt{\frac{\hbar\omega_m}{2}}\left[\hat{a}_m(t)\mathbf{D}_m(\mathbf{r}) + \hat{a}_m^\dagger(t)\mathbf{D}_m^*(\mathbf{r})\right], \tag{1.37}$$

$$\hat{\mathbf{B}}(\mathbf{r},t) = \sum_m \sqrt{\frac{\hbar\omega_m}{2}}\left[\hat{a}_m(t)\mathbf{B}_m(\mathbf{r}) + \hat{a}_m^\dagger(t)\mathbf{B}_m^*(\mathbf{r})\right], \tag{1.38}$$

where each mode is a solution of Maxwell equations supported by the structure of interest, a photon is defined as the fundamental excitation of the electromagnetic field in one mode, and $\hat{a}_m$ and $\hat{a}_m^\dagger$ are the annihilation and creation operators of mode m, satisfying the bosonic commutation relations:

$$[\hat{a}_m, \hat{a}_{m'}^\dagger] = \delta_{mm'}, \quad [\hat{a}_m, \hat{a}_{m'}] = 0. \tag{1.39}$$

Following the arguments developed by Bhat and Sipe [38] and further elaborated by Raymer [33], the appropriate normalization condition for the displacement field in a dispersive medium is

$$\int_V \frac{\mathbf{D}_m^*(\mathbf{r}) \cdot \mathbf{D}_m(\mathbf{r})}{\varepsilon_0 \varepsilon_r(\mathbf{r};\omega_m)} \frac{v_p(\mathbf{r};\omega_m)}{v_g(\mathbf{r};\omega_m)} d^3\mathbf{r} = 1, \tag{1.40}$$

where $v_p(\mathbf{r};\omega) = \frac{c}{n_{\text{eff}}(\mathbf{r};\omega)}$ and $v_g(\mathbf{r};\omega) = \frac{c}{n_g(\mathbf{r};\omega)}$ are the local phase and group velocities. Similarly, assuming that the magnetization effects are negligible, the magnetic field is normalized to

$$\int_V \frac{\mathbf{B}_m^*(\mathbf{r}) \cdot \mathbf{B}_m(\mathbf{r})}{\mu_0} d^3\mathbf{r} = 1. \tag{1.41}$$

With the proper normalization, the quantum Hamiltonian takes the familiar form of a harmonic oscillator:

$$\hat{\mathscr{H}}^{(\mathrm{L})} = \sum_m \hbar\omega_m \left(\hat{a}_m^\dagger \hat{a}_m + \frac{1}{2} \right), \tag{1.42}$$

where the superscript (L) recalls that we are in the linear regime.

1.2.2 Including Nonlinearities

The framework developed above can be extended to the case of a nonlinear material response, with the constitutive relation between the electric field and displacement field becoming more complex. In the presence of second- and third-order nonlinearities, the electric field components are given by:

$$E_i = \frac{D_i}{\varepsilon_0 \varepsilon_r} - \frac{\Gamma^{(2)}_{ijl}}{\varepsilon_0} D_j D_l - \frac{\Gamma^{(3)}_{ijlm}}{\varepsilon_0} D_j D_l D_m - \dots, \tag{1.43}$$

where the summation over repeated spatial component indices i, j, l, m is implicit. In Eq. (1.43), we used the second- and third-order nonlinear tensors $\Gamma^{(2)}_{ijl}$ and $\Gamma^{(3)}_{ijlm}$ instead of the more common tensors $\chi^{(2)}_{ijl}$ and $\chi^{(3)}_{ijlm}$ appearing in the constitutive relation for the displacement. This is because we want to use $\mathbf{D}$ as the fundamental field. The Γ and χ tensors are related to each other by considering that the constitutive relation for the displacement field is the inverse of Eq. (1.43). For instance, one has $\Gamma^{(2)}_{ijl} = \frac{\chi^{(2)}_{ijl}}{\varepsilon_0\ \varepsilon_r^3}$, and $\Gamma^{(3)}_{ijlm} = \frac{\chi^{(3)}_{ijlm}}{\varepsilon_0^2\ \varepsilon_r^4} - 2\frac{\chi^{(2)}_{ijn}\ \chi^{(2)}_{nlm}}{\varepsilon_0^2\ \varepsilon_r^5}$. In the rest of the thesis, we will work mainly with the Γ tensors, but we will refer to a process associated with the N-th order term of Eq. (1.43) as a $\chi^{(N)}$ nonlinear process.

Substituting this expression into Eq. (1.32), the complete Hamiltonian becomes:

$$\begin{aligned}
\mathcal{H}(t) &= \int_V \left[\frac{\mathbf{B}(\mathbf{r},t)\cdot\mathbf{B}(\mathbf{r},t)}{2\mu_0} + \frac{\mathbf{D}(\mathbf{r},t)\cdot\mathbf{D}(\mathbf{r},t)}{2\varepsilon_0\varepsilon_r(\mathbf{r})}\right] d^3\mathbf{r} \\
&\quad - \frac{1}{3\varepsilon_0}\int_V \Gamma^{(2)}_{ijk}(\mathbf{r}) D_i(\mathbf{r},t) D_j(\mathbf{r},t) D_k(\mathbf{r},t) d^3\mathbf{r} \\
&\quad - \frac{1}{4\varepsilon_0}\int_V \Gamma^{(3)}_{ijkl}(\mathbf{r}) D_i(\mathbf{r},t) D_j(\mathbf{r},t) D_k(\mathbf{r},t) D_l(\mathbf{r},t) d^3\mathbf{r} + \dots \\
&= \mathcal{H}^{(L)}(t) + \mathcal{H}^{(\mathrm{NL})}(t), \qquad (1.44)
\end{aligned}$$

where one can recognize the linear Hamiltonian $\mathcal{H}^{(L)}$, identical to Eq. (1.33), and a nonlinear part $\mathcal{H}^{(\mathrm{NL})}$ containing the higher-order interaction terms.

Treating $\mathcal{H}^{(\mathrm{NL})}$ as a perturbation to the linear dynamics, the Hamiltonian can be quantized in terms of the modes Eq. (1.37) and Eq. (1.38):

$$\begin{aligned}
\hat{\mathcal{H}}(t) &= \sum_\alpha \hbar\omega_\alpha \hat{a}^\dagger_\alpha(t)\hat{a}_\alpha(t) - \frac{1}{3\varepsilon_0}\int_V \Gamma^{(2)}_{ijl}(\mathbf{r}) : \hat{D}_i(\mathbf{r})\hat{D}_j(\mathbf{r})\hat{D}_l(\mathbf{r}) : d^3\mathbf{r} \\
&\quad - \frac{1}{4\varepsilon_0}\int_V \Gamma_{ijlm},^{(3)}(\mathbf{r}) : \hat{D}_i(\mathbf{r},t)\hat{D}_j(\mathbf{r},t)\hat{D}_l(\mathbf{r},t)\hat{D}_m(\mathbf{r},t) : d^3\mathbf{r} + \dots \\
&= \hat{\mathcal{H}}^{(L)}(t) + \hat{\mathcal{H}}^{(\mathrm{NL})}(t), \qquad (1.45)
\end{aligned}$$

where the colons denote normal ordering of operators. Unlike the linear Hamiltonian, the quantum nonlinear one was not expanded in terms of the creation and annihilation operators. This is because such an expansion contains several different nonlinear processes, which would be impractical to treat in one single expression. Additionally, depending on the characteristics of the system under study, many processes described by the full nonlinear Hamiltonian are often prohibited by energy or momentum conservation, or by other selection rules, related, for example, to symmetry. For this reason, Eq. (1.45) is more conveniently used as a starting point, from which one can select a few terms relevant to a specific process of interest, neglecting all the others. For each process, the overlap integral of the fields provides the coupling strength, allowing one to determine which processes are allowed and which ones can be neglected. In the following chapter, we will apply this formalism to specific nonlinear processes and device geometries relevant to quantum light generation and manipulation.

1.3 Conclusion

In this chapter, we discussed a theoretical framework for modeling linear and nonlinear light propagation in integrated photonic circuits. We first reviewed the scattering matrix formalism as a versatile tool for analyzing the linear properties of many photonic structures. In Chapter 1, this method was only applied to some simple resonators and interferometers. In the following, we will employ it to investigate more complicated structures. In fact, the number of linear equations involved in a scattering matrix problem scales as four times the number of components in the photonic integrated circuit, resulting in a low computational complexity.

We then addressed the quantization of the electromagnetic field. By adopting the displacement field $\mathbf{D}$ and magnetic field $\mathbf{B}$ as fundamental variables, we ensured consistency with Maxwell's equations even in the presence of nonlinearities. Additionally, the field normalization was chosen to satisfy the Poynting theorem. Throughout Section 1.2, we never assumed a particular geometry for the region where the field is quantized, making this a robust foundation for describing nonlinear phenomena in integrated circuits, as we will do in Chapter 2.

Among the fundamental building blocks discussed in this chapter, ring resonators provide light confinement and field enhancement on resonance, useful to increase light-matter interactions and improve the efficiency of the inherently weak nonlinear processes that underlie the generation of quantum states. Ring resonators, along with Mach-Zehnder interferometers, were also discussed for their ability to control the phase and intensity of the transmitted light, useful to selectively tune the spectral properties of photonic structures. In Chapter 3, we will apply these principles to design a device for squeezed light generation. In Chapter 6, we will present a second application of resonant interferometric principles in quantum photonics. In this case, a Sagnac interferometer will be used to create an interaction between two counterpropagating modes, enabling the control of single-photon emission from a dipole. Here too, a ring resonator will enhance the dipole emission.

While in Chapter 1 we discussed the basic principles of photonic integrated circuits, we will present a more detailed analysis in Chapter 4. This includes the effects of waveguide geometry and strategies for optimizing device design based on specific applications, such as squeezed light generation.

Chapter 2

Spontaneous Four-Wave Mixing: Theory and Applications

Starting from the complete nonlinear Hamiltonian Eq. (1.44) derived in Chapter 1, we focus on the third-order nonlinear term. This term describes the interaction of four electromagnetic field modes through the $\chi^{(3)}$ susceptibility of the material. Unlike second-order susceptibility, the third-order one is naturally present in centrosymmetric materials such as silicon and silicon nitride, making it particularly interesting for CMOS-compatible integrated photonic platforms. In particular, we study one third-order process that is widely used for quantum light generation: spontaneous four-wave mixing (SFWM).

SFWM involves the interaction of one or two pump lasers with a nonlinear material. Pairs of photons from the pumps are annihilated to create pairs of photons at different frequencies, typically called signal and idler. Energy and momentum conservation imply that

$$\omega_{P1} + \omega_{P2} = \omega_S + \omega_I, \tag{2.1}$$

$$\mathbf{k}_{P1} + \mathbf{k}_{P2} = \mathbf{k}_S + \mathbf{k}_I, \tag{2.2}$$

where $\omega_{P1,P2}$ are the pump frequencies, $\omega_{S,I}$ are the signal and idler frequencies, and $\mathbf{k}_{\mathbf{P1},\mathbf{P2},\mathbf{S},\mathbf{I}}$ represent the corresponding wave vectors. In the single-pump SFWM (SP-SFWM) configuration, only one pump is used, and the signal-idler pair is non-degenerate, as shown in Fig. 2.1(a). When two non-degenerate pumps are used instead, the process is dual-pump SFWM (DP-SFWM), and the generated pair can be degenerate, as in Fig. 2.1(b). In this case, one typically talks only of the signal mode, as the idler is indistinguishable from it.

SFWM is a spontaneous process. This means that it occurs when both signal and idler are initialized into a vacuum state. On the contrary, when an additional laser, called the *seed*, is injected at the signal or idler mode, the process is stimulated four-wave mixing, whose efficiency is typically enhanced by the interaction between the seed and pump lasers [39]. Both SFWM and its stimulated counterpart belong to the class of *parametric* processes, because

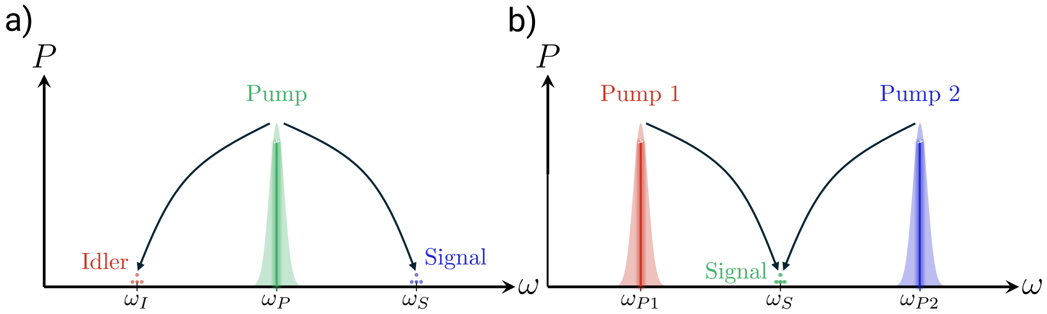

Figure 2.1: Schematic representation of SFWM. (a) SP-SFWM pairs of photons from one pump laser at frequency ω_P (green) are converted into signal-idler pairs at frequencies ω_S and ω_I (blue and red, respectively). (b) DP-SFWM pairs of photons from two pump lasers at frequencies ω_{P1} (red) and ω_{P2} (blue) are converted into signal pairs at frequency ω_S (green).

they do not involve a net energy exchange with the nonlinear material. As a consequence, the photon energy conservation Eq. (2.1) does not depend on the material's degrees of freedom, and the material affects the photon dynamics solely through the linear and nonlinear response parameters.

SFWM represents a paradigmatic example of how optical nonlinearities can be harnessed to generate non-classical states of light. In the first section of this chapter, we review its characteristics, highlighting the properties and applications of the resulting quantum state, namely the squeezed state. Then, we review two methods for modeling SFWM in integrated structures. The one described in the second section is based on a Lorentzian treatment of the four modes involved in SFWM. The asymptotic-field theory presented in the third section is a perturbative description that is suited to treat arbitrary field distributions in the squeezer. Finally, in the fourth section, we present a new approach to extend the asymptotic-field treatment to the non-perturbative regime.

2.1 Squeezed Light by Spontaneous Four-Wave Mixing

The SFWM Hamiltonian is built by substituting the mode expansion of the displacement field Eq. (1.37) into the third-order nonlinear term of Eq. (1.45), retaining only the contributions that contain two creation operators in the signal and idler modes and two annihilation operators in the pump modes. All other terms in the expansion either describe different $\chi^{(3)}$ processes or correspond to processes that are not allowed by energy or momentum conservation.

We start by considering ideal processes involving single-mode pumps, a single-mode signal and a single-mode idler. In this case, the SP-SFWM Hamiltonian takes the form:

$$\hat{\mathscr{H}}^{(\text{SP-SFWM})}(t) = -\frac{1}{4\varepsilon_0}\frac{4!}{2!}\frac{\hbar^2\sqrt{\omega_P^2\omega_S\omega_I}}{4}\hat{a}_S^\dagger\hat{a}_I^\dagger\hat{a}_P^2 \int_V \Gamma^{(3)}_{ijlm}(\mathbf{r})D^*_{S,i}(\mathbf{r})D^*_{I,j}(\mathbf{r})D_{P,l}(\mathbf{r})D_{P,m}(\mathbf{r})d^3\mathbf{r} + \text{H.c.}, \tag{2.3}$$

where $\hat{a}_P$, $\hat{a}_S$, and $\hat{a}_I$ are the annihilation operators for the pums, signal, and idler modes, respectively, and the factor $\frac{4!}{2!}$ counts the number of permutations assigning modes $\{P, S, I\}$ to the field components $\{i, j, l, m\}$. Similarly, the DP-SFWM Hamiltonian is

$$\hat{\mathscr{H}}^{(\text{DP-SFWM})}(t) = -\frac{3}{\varepsilon_0}\frac{\hbar^2\sqrt{\omega_{P1}\omega_{P2}\omega_S^2}}{4}\hat{a}_S^{\dagger 2}\hat{a}_{P1}\hat{a}_{P2} \int_V \Gamma^{(3)}_{ijlm}(\mathbf{r})D^*_{S,i}(\mathbf{r})D^*_{S,j}(\mathbf{r})D_{P1,l}(\mathbf{r})D_{P2,m}(\mathbf{r})d^3\mathbf{r} + \text{H.c.}. \tag{2.4}$$

In general, SFWM can involve multimode signal-idler pairs. In this case, the full SFWM Hamiltonian will contain a summation or an integral of several terms like Eq. (2.3) or Eq. (2.4).

Since the pumps are typically lasers operating in a coherent state, they can be treated semi-classically, replacing the pump operators with their expectation values: $\hat{a}_P(t) \to \langle\hat{a}_P(t)\rangle = \alpha_P(t)$, where $|\alpha_P(t)|^2$ is the mean photon number carried by a pump pulse. Additionally, we work in the undepleted pump approximation, in which the effects of SFWM on the pump are negligible. Under these assumptions, the mean number of pump photons is constant in time: $|\alpha_P(t)| \approx |\alpha_P|$ and, assuming perfect resonance between the pump, signal, and idler modes, the SFWM Hamiltonians take a quadratic form:

$$\hat{\mathscr{H}}^{(\text{SP-SFWM})}(t) = \frac{i\hbar}{2}\xi_{\text{SP}}\hat{a}_S^\dagger\hat{a}_I^\dagger + \text{H.c.}, \tag{2.5}$$

and

$$\hat{\mathscr{H}}^{(\text{DP-SFWM})}(t) = \frac{i\hbar}{2}\xi_{\text{DP}}\hat{a}_S^{\dagger 2} + \text{H.c.}, \tag{2.6}$$

where

$$\xi_{\text{SP}} = \frac{3}{\varepsilon_0}\frac{i\hbar\sqrt{\omega_P^2\omega_S\omega_I}}{2}\alpha_P^2 \int_V \Gamma^{(3)}_{ijlm}(\mathbf{r})D^*_{S,i}(\mathbf{r})D^*_{I,j}(\mathbf{r})D_{P,l}(\mathbf{r})D_{P,m}(\mathbf{r})d^3\mathbf{r}, \tag{2.7}$$

for SP-SFWM, and

$$\xi_{\text{DP}} = \frac{3}{\varepsilon_0}\frac{i\hbar\sqrt{\omega_{P1}\omega_{P2}\omega_S^2}}{2}\alpha_{P1}\alpha_{P2} \int_V \Gamma^{(3)}_{ijlm}(\mathbf{r})D^*_{S,i}(\mathbf{r})D^*_{S,j}(\mathbf{r})D_{P1,l}(\mathbf{r})D_{P1,m}(\mathbf{r})d^3\mathbf{r}, \tag{2.8}$$

for DP-SFWM. Eq. (2.5) and Eq. (2.6) are the two-mode and single-mode squeezing Hamiltonians [40]. When applied to an initial vacuum state, which is always the case when dealing with a spontaneous process like SFWM, two-mode or single-mode squeezed vacuum states are generated

$$|\text{sq}_{\text{SP}}\rangle = \exp\left[\frac{r_{\text{SP}}e^{i\phi_{\text{SP}}}}{2}\hat{a}_S^\dagger \hat{a}_I{}^\dagger - \text{H.c.}\right]|\text{vac}\rangle \tag{2.9}$$

$$|\text{sq}_{\text{DP}}\rangle = \exp\left[\frac{r_{\text{DP}}e^{i\phi_{\text{DP}}}}{2}\hat{a}_S^{\dagger 2} - \text{H.c.}\right]|\text{vac}\rangle\,. \tag{2.10}$$

with $r_I = |\xi_I|\Delta t$ being the squeeze amplitude, $\phi_I(t) = \arg[\xi_I \Delta t]$, with $I \in \{\text{SP, DP}\}$ the squeeze phase, and Δt the time interval during which the squeezing Hamiltonians were applied.

2.1.1 Properties of Squeezed States

We now focus on the single-mode squeezed state Eq. (2.10) generated by DP-SFWM, and review some of its key properties. For simplicity, we drop the subscript DP. The Fock basis expansion is [41]:

$$\begin{aligned}|\text{sq}\rangle &= \frac{1}{\sqrt{\cosh(r)}}\exp\left[\frac{e^{i\phi}}{2}\tanh(r)\hat{a}^{\dagger 2}\right]\left[\frac{1}{\sqrt{\cosh(r)}}\right]^{\hat{a}^\dagger\hat{a}}\exp\left[\frac{e^{-i\phi}}{2}\tanh(r)\hat{a}^{2}\right]|\text{vac}\rangle\\ &= \frac{1}{\sqrt{\cosh(r)}}\sum_{n=0}^{\infty}\frac{e^{in\phi}\sqrt{(2n)!}}{2^n n!}\tanh^n(r)\,|2n\rangle\,,\end{aligned} \tag{2.11}$$

where $|2n\rangle$ is the Fock state with $2n$ photons in the signal mode. This expansion reflects the fact that squeezed photons are generated in pairs.

However, squeezed vacuum is fundamentally different from a simple two-photon state, as it does not have a well-defined photon number. Rather, one can compute the average photon number, which is the expectation value of the number operator $\hat{n} = \hat{a}^\dagger\hat{a}$:

$$\begin{aligned}\langle\text{sq}|\hat{n}|\text{sq}\rangle &= \left\langle \text{vac}\,\middle|\,\exp\left[-\left(\frac{re^{i\phi}}{2}\hat{a}^{\dagger 2} - \text{H.c.}\right)\right]\hat{a}^\dagger\hat{a}\exp\left[\frac{re^{i\phi}}{2}\hat{a}^{\dagger} - \text{H.c.}\right]\,\middle|\,\text{vac}\right\rangle =\\ &= \langle\text{vac}\,|\,[\cosh(r)\hat{a}^\dagger - e^{-i\phi}\sinh(r)\hat{a}][\cosh(r)\hat{a} - e^{i\phi}\sinh(r)\hat{a}^\dagger]\,|\,\text{vac}\rangle =\\ &= \sinh^2(r).\end{aligned} \tag{2.12}$$

This quantity depends only on the squeeze amplitude r and is often more directly accessible in experiments than the squeeze amplitude, thus providing a practical means of quantifying the squeezing strength. However, the mean photon number alone is not enough to certify that a state is squeezed. To do this, a full analysis of the photon statistics is needed.

An alternative way to completely characterize a squeezed state is through the study of its quadrature statistics. Recalling Eq. (1.42), which shows that light can be described to a good approximation as a harmonic oscillator, with nonlinearities treated as higher-order perturbations, it is useful to define a generalized quadrature operator of a harmonic oscillator:

$$\hat{X}(\theta) = \sqrt{\frac{\hbar}{2}}\left(e^{i\theta}\hat{a} + e^{-i\theta}\hat{a}^{\dagger}\right), \tag{2.13}$$

where θ is the quadrature phase. For $\theta \in \{0, \frac{\pi}{2}\}$, this operator reduces to the standard Hermitian quadratures of the harmonic oscillator:

$$\hat{P} = \hat{X}(0) = \sqrt{\frac{\hbar}{2}}\left(\hat{a} + \hat{a}^{\dagger}\right) \qquad \hat{Q} = \hat{X}\left(\frac{\pi}{2}\right) = i\sqrt{\frac{\hbar}{2}}\left(\hat{a} - \hat{a}^{\dagger}\right), \tag{2.14}$$

Looking only at the expectation value of the quadrature,

$$\langle \hat{X}(\theta) \rangle_{\text{sq}} := \langle \text{sq}|\hat{X}(\theta)|\text{sq}\rangle = 0,$$

a single-mode squeezed state seems to have the same characteristics as the vacuum state. However, the quadrature variance exhibits a fundamentally different behaviour:

$$\mathfrak{V}(\theta) = \langle \hat{X}(\theta)^2 \rangle_{\text{sq}} - \langle \hat{X}(\theta) \rangle_{\text{sq}}^2 = \frac{\hbar}{2}[\cosh(2r) - \sinh(2r)\cos(\phi - 2\theta)]. \tag{2.15}$$

Different than the variance of vacuum, which is independent of θ and equal to the shot noise level $\hbar/2$, squeezed states exhibit a variance that oscillates with the quadrature phase θ. The minimum variance is

$$\mathfrak{V}_{\text{min}} = \frac{\hbar}{2}e^{-2r}, \tag{2.16}$$

and is reached when $\phi = 2\theta + 2m\pi$ with m integer. The maximum variance is

$$\mathfrak{V}_{\text{max}} = \frac{\hbar}{2}e^{2r}, \tag{2.17}$$

and it is reached when $\phi = 2\theta + (2m+1)\pi$. Eq. (2.16) shows that squeezed states have one quadrature with uncertainty compressed below the shot noise limit, hence the term *squeezed* states. This reduced uncertainty does not counterdict the Heisenberg indetermination principle, as $\hat{X}_{\text{min}}$ and $\hat{X}_{\text{max}}$ are conjugate variables, and the product of their variances satisfies

$$\mathfrak{V}_{\text{min}} \cdot \mathfrak{V}_{\text{max}} = \frac{\hbar^2}{4}, \tag{2.18}$$

which is the Heisenberg uncertainty principle bound with the equality sign. This confirms that ideal single-mode squeezed states are minimum uncertainty states, similar to vacuum and coherent states, but with a non-uniform distribution of the uncertainty.

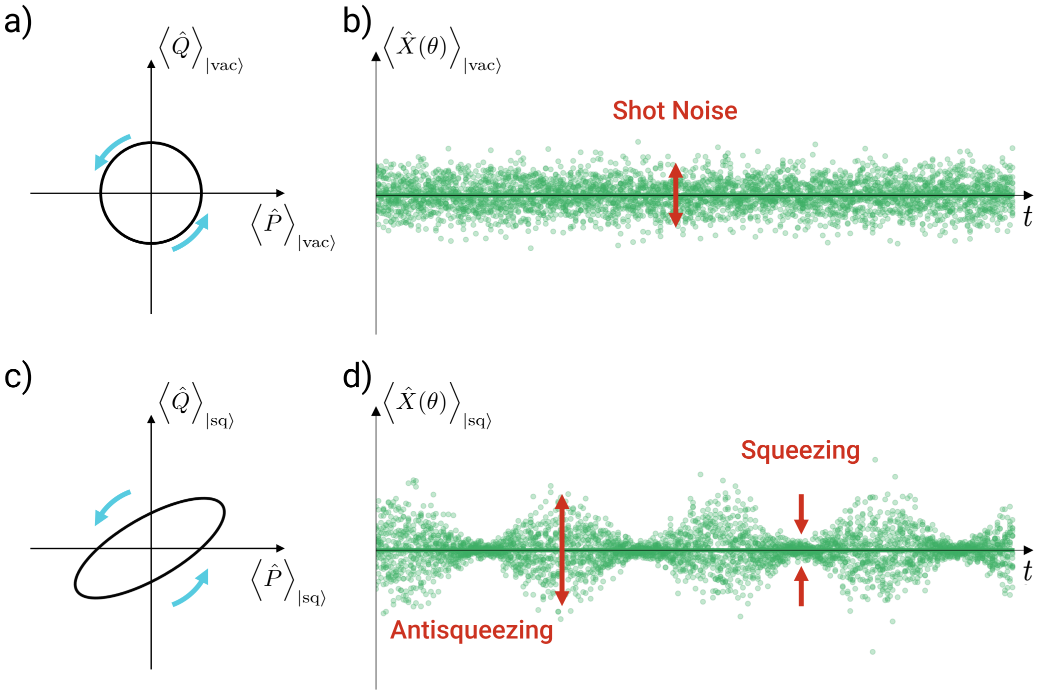

Figure 2.2: Comparison between vacuum and squeezed vacuum states. (a) Phase space representation of the vacuum state's quadrature standard deviation. Blue arrows indicate the state's time evolution. (b) Time evolution of the quadrature expectation value $\langle \hat{X}(\theta) \rangle$ for the vacuum state. Green dots are sampled from a zero-mean distribution with variance equal to the shot noise. (c) Phase space representation of a squeezed vacuum state's quadrature standard deviation, with $\phi = -\frac{pi}{6}$. The reduced variance in the quadrature with $\theta = -\frac{pi}{3}$ comes at the cost of increased variance in the orthogonal quadrature, forming an elliptical region. (d) Time evolution of $\langle \hat{X}(\theta) \rangle$ for the squeezed state, exhibiting alternating regions of squeezing (fluctuations below the shot noise) and antisqueezing (fluctuations above the shot noise) as the phase ϕ varies. In figures b) and d) θ is fixed to $-\frac{\pi}{3}$.

This consideration leads to the definition of a physical quantity measuring the quality of a squeezed state: the squeezing level, defined as

$$\mathcal{S} = 10 \log_{10} \left(\frac{2}{\hbar} \mathfrak{V}_{\mathrm{min}} \right) = 10 \log_{10} (e^{-2r}), \tag{2.19}$$

which is the maximum reduction, in dB, of the quadrature variance compared to shot noise. For an ideal single-mode state, the squeezing level is proportional to the squeeze amplitude: $S = \frac{20}{\ln(10)} r$. In analogy to squeezing, one can also define the antisqueezing:

$$\mathcal{A} = 10 \log_{10} \left(\frac{2}{\hbar} \mathfrak{V}_{\mathrm{max}} \right) = 10 \log_{10} (e^{2r}), \tag{2.20}$$

The quadrature can be measured experimentally through homodyne detection, where the signal interferes with a strong laser, the *local oscillator*, at a balanced beam splitter, as depicted in Fig. 2.3. Two photodetectors are placed at the two outputs of the beam splitter, and their resulting photocurrents are subtracted electronically. It can be shown that if the two optical paths through the beam splitter are balanced, the resulting signal difference is proportional to the expectation value of the field quadrature. The same proportionality holds for the uncertainty and all the higher-order moments of the two quantities. By varying the local oscillator phase ϕ_{LO} and measuring the noise variance, one can reconstruct the complete quadrature noise ellipse and determine the squeezing level.

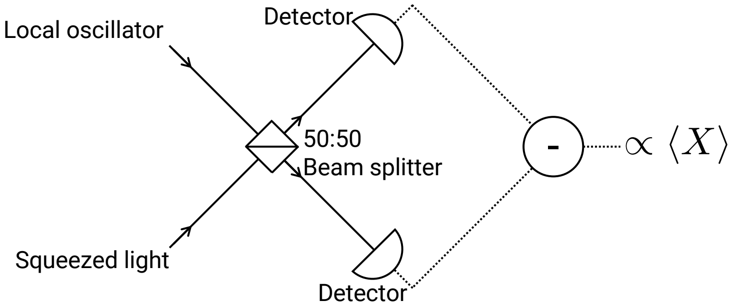

Figure 2.3: Schematic setup of an homodyne detection experiment. The solid lines represent the optical paths. The dotted lines represent the electronic processing of the signal.

2.1.2 Squeezed Light in Practice

Squeezed states have been studied for almost a century [42, 43]. However, for decades, the attempts at an experimental demonstration faced numerous technical challenges. [44]. Only in 1985 Slusher and collaborators observed squeezed light using four-wave mixing in a sodium atomic vapor [45]. The following year, two additional demonstrations were made on completely different platforms. Shelby and colleagues exploited $\chi^{(3)}$ nonlinearity in optical fibers [46], while Wu *et al.* achieved significantly improved squeezing levels of 3.5 dB using the $\chi^{(2)}$ process of spontaneous parametric downconversion in a nonlinear crystal [47]. The $\chi^{(2)}$ approach quickly became the most common due to its higher efficiency and relative experimental simplicity. In 2016, Vahlbruch *et al.* attained the current squeezing world record of 15 dB in a parametric downconversion experiment. However, the other platforms that were used for the first proof-of-principle demonstrations were never abandoned.

While $\chi^{(2)}$ materials remain the most efficient platform for squeezing generation in bulk, their poor compatibility with standard complementary metal-oxide-semiconductor (CMOS) technology has driven significant interest toward $\chi^{(3)}$ materials. Despite $\chi^{(3)}$ nonlinearity being typically lower than $\chi^{(2)}$, materials such as silicon and silicon nitride are CMOS compatible and provide a robust pathway for scalable photonic integrated sources [48, 49]. Significant progress has been made with various integrated platforms, including $\chi^{(2)}$ periodically poled waveguides achieving over 8 dB of squeezing [50], and silicon nitride microresonators demonstrating broadband dual-pump operation [51, 52], and squeezing levels above 10 dB in single-pump operation [53]. More complex integrated structures, such as coupled-resonator systems, have also been used to enhance SFWM, reaching 1.8 dB of directly detected squeezing in a silicon nitride platform, corresponding to 8 dB on chip [54].

The development of squeezed light sources has enabled applications across multiple domains. Including precise sensing [55, 56], microscopy [57], and continuous-variable quantum computing [58], with experimental demonstrations of quantum computational advantage using photonic systems [59] and programmable quantum processors [60]. Squeezed light is also widely employed as a starting point for generating other quantum states, such as heralded single-photons [61, 62] or more complex non-gaussian states [63, 64, 65].

In this thesis, we focus on the generation of squeezed light by SFWM in integrated devices. Like many nonlinear processes, SFWM is inherently weak, requiring enhancement of the optical fields and extended interaction times and lengths to achieve significant effects. Nanophotonic resonators address both requirements by providing field enhancement through resonant power buildup and extended interaction times due to optical confinement. Ring resonators are particularly attractive for their small footprint, high field enhancement, and mature fabrication technology [66]. In the following sections, we present three theoretical frameworks to model SP-SFWM in a ring resonator. Much of what will be said can be adapted to DP-SFWM and other nonlinear processes, but we choose to restrict the description to a special case for the sake of clarity.

2.2 Lorentzian Model for Squeezing in Integrated Resonators

The first theoretical model we discuss, following the work by Quesada *et al.*. [40], exploits one fundamental characteristic of high-quality ring resonators: their comb of Lorentzian resonances. For an efficient enhancement of the process, signal, idler, and pumps must be aligned to three ring resonances at frequencies satisfying energy and momentum conservation.

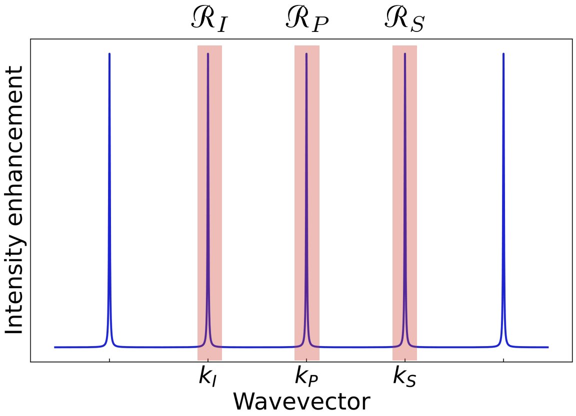

Figure 2.4: Scheme of the resonance ranges that form a Lorentzian basis for the field modes in a ring resonator.

A natural way to express the fields appearing in the nonlinear Hamiltonian Eq. (2.3), is to expand them on a discrete set of modes spaning a narrow frequency range $\mathcal{R}_J$ centered around the ring resonance frequency ω_J, with $J \in \{P, S, I\}$, as shown in Fig. 2.4:

$$\mathbf{D}_J^{(\text{ring})}(\mathbf{r}) = \frac{\mathbf{d}_J(\mathbf{r}_\perp;\zeta)}{\sqrt{L}} e^{ik_J\zeta}, \tag{2.21}$$

where, referring to Fig. 1.2a, L is the ring circumference, ζ parameterizes the azimuthal position, $\mathbf{r}_\perp = (y, \rho)$ is the transverse coordinate, $k_J = 2\pi m_J/L$ is the central wavevector of resonance J with m_J the integer resonance index, and $\mathbf{d}_J(\mathbf{r}_\perp;\zeta)$ are the transverse field distributions, whose absolute values are assumed independent of ζ.

With this in hand, the mode expansion of the displacement field operator Eq. (1.37) takes the form (cf. Eq. (57) of Quesada *et al.* [40])

$$\mathbf{D}^{(\text{ring})}(\mathbf{r}, t) = \sum_J \sqrt{\frac{\hbar\omega_J}{2L}} \hat{a}_J(t)\mathbf{d}_J(\mathbf{r}_\perp;\zeta)e^{ik_J\zeta} + \text{H.c.}, \tag{2.22}$$

where $\hat{a}_J(t)$ is the time-dependent creation operator in mode J.

Contrary to the ring resonator, the channel supports a continuum of modes. To describe this, it is convenient to write its field operators as (cf. Eq. (92) of

Quesada *et al.* [40])

$$\mathbf{D}^{(\mathrm{chan})}(\mathbf{r},t) \approx \sum_J \sqrt{\frac{\hbar\omega_J}{2}}\mathbf{d}_J(y,z)\hat{\psi}_J(x,t)e^{ik_Jx} + \text{H.c.}, \tag{2.23}$$

where

$$\hat{\psi}_J(z,t) := \int_{k\in\mathcal{R}_J} \frac{dk}{\sqrt{2\pi}}\hat{a}_J(k,t)e^{i(k-k_J)z}, \tag{2.24}$$

are slowly-varying envelope ladder operators for the channel, and we neglected index or field profile variations over the the frequency range $\mathcal{R}_J$.

2.2.1 Ring-Channel Dynamics

It can be shown that, neglecting losses and group velocity dispersion, the linear Hamiltonian for a ring resonator point-coupled to a channel waveguide at the waveguide coordinate $z = 0$ is given by (cf. Eq. (105) of Quesada *et al.* [40])

$$\begin{aligned}\hat{\mathcal{H}}^{(\mathrm{L})} = &\sum_J \hbar\omega_J \int \hat{\psi}_J^\dagger(z)\hat{\psi}_J(z)dz + \sum_J \hbar\omega_J\hat{a}_J^\dagger\hat{a}_J + \\ &-\sum_J \frac{1}{2}i\hbar v_J \int \left(\hat{\psi}_J^\dagger(z)\frac{\partial\hat{\psi}_J(z)}{\partial z} - \frac{\partial\hat{\psi}_J^\dagger(z)}{\partial z}\hat{\psi}_J(z)\right)dz \\ &+\sum_J \left(\hbar\sqrt{\frac{2v_J^2(1-\sigma)}{L}}\hat{a}_J^\dagger\hat{\psi}_J(0) + \text{H.c.}\right),\end{aligned} \tag{2.25}$$

where the first two terms represent the linear Hamiltonians at frequency ω_J for the channel and ring fields, respectively, the third term is a correction including the effects of the group velocity v_J, and the fourth term describes the ring-channel coupling with σ the self-coupling coefficient.

Losses can be included separately, by defining a second fictitious channel coupled to the ring, which is called the phantom channel. The ring-phantom coupling coefficient is $\sigma_{\mathrm{ph}} = 1 - e^{-\frac{\alpha}{2}L}$, with α the attenuation coefficient, such that for each round trip, the probability of couping to the phantom-channel corresponds to the loss probability in the ring. The phantom channel follows the same dynamics Eq. (2.25) of the physical channel, with field operators $\psi_{J\mathrm{ph}}(x)$. This is a different approach compared to the most standard loss treatment based on a master equation, with leaky modes loosing energy to the environment [67]. The advantage here is that a phantom channel can be described with the same equations of a real physical channel, maintaining a unitary evolution. The disadvantage is that this is a somewhat artificial construction, with losses localized at a certain point instead of being distributed throughout the structure.

Starting from Eq. (2.3), the SP-SFWM contribution to the nonlinear Hamiltonian is:

$$\hat{\mathcal{H}}^{(\text{SP-SFWM})} = -\hbar\Lambda^{\mathrm{SP}}\hat{a}_S^\dagger\hat{a}_I^\dagger\hat{a}_P\hat{a}_P + \text{H.c.}, \tag{2.26}$$

where the nonlinear coupling coefficient is (cf. Eq. (389) of Quesada *et al.* [40]):

$$\Lambda^{\mathrm{SP}} = \frac{\hbar(\omega_P^2\omega_S\omega_I)^{1/4} v_P\sqrt{v_S v_I}}{L}\gamma_{\mathrm{SP}}, \tag{2.27}$$

with the SP-SFWM nonlinear parameter γ_{SP} defined as:

$$\gamma_{\mathrm{SP}} = \frac{3(\omega_P^2\omega_S\omega_I)^{1/4}}{4v_P\sqrt{v_S v_I}}\frac{\epsilon_0}{L}\int d\mathbf{r}\,\chi^{(3)}_{ijlm}(\mathbf{r})e^*_{S,i}(\mathbf{r})e^*_{I,j}(\mathbf{r})e_{P,l}(\mathbf{r})e_{P,m}(\mathbf{r}), \tag{2.28}$$

where $\chi^{(3)}_{ijlm}$ is the third-order nonlinear susceptibility tensor and $\mathbf{e}_J$ are the electric field mode profiles correspoding to displacement field $\mathbf{d}_J$.

In the low-power regime, as far as the ring resonances are Lorentzian, Eq. (2.28) accurately captures the physics of SP-SFWM. However, when moving to higher pump powers, two more processes must be taken into account: self-phase modulation (SPM) and cross-phase modulation (XPM), which are stimulated $\chi^{(3)}$ processes involving the interaction of the pump with itself (SPM) and with other resonances (XPM). In particular, SPM involves the annihilation and simultaneous creation of pump photon pairs, while XPM is the annihilation and creation of pump-signal or pump-idler pairs. These stimulated processes result in an energy shift of the ring resonances compared to those of the unpumped *cold* resonator.

Following the same approach described for SP-SFWM, one can find the nonlinear coupling coefficients Λ^{SPM} and Λ^{XPM}, expressing the strength of SPM and XPM, respectively. SPM is about four times weaker than XPM, causing a smaller shift for the pump resonance compared to the other ones. The complete Hamiltonian is then

$$\hat{\mathscr{H}} = \hat{\mathscr{H}}^{(\mathrm{L})} + \hat{\mathscr{H}}^{(\text{SP-SFWM})} - \hbar\Lambda^{\mathrm{SPM}}a_P^\dagger a_P^\dagger a_P a_P - \hbar\Lambda^{\mathrm{XPM}}\left(a_S^\dagger a_P^\dagger a_S a_P + a_I^\dagger a_P^\dagger a_I a_P\right). \tag{2.29}$$

The dynamics of the system is governed by the Heisenberg equation:

$$i\hbar\frac{d\hat{O}(t)}{dt} = [\hat{O}(t), \hat{\mathscr{H}}], \tag{2.30}$$

where $\hat{O}(t)$ represents any operator in the Heisenberg picture. Applying this to the ring mode operators and treating the pump as an undepleted classical field with amplitude $\alpha_P(t)$, and detuning Δ_P from the pump resonance, the equations of motion for the signal and idler modes become (cf. Eq. (394) of

Quesada *et al.* [40]):

$$\begin{aligned}\frac{d\tilde{a}_S(t)}{dt} &= \left(i\Lambda^{\text{XPM}}|\alpha_P(t)|^2 - i\Delta_P - \Gamma_S - \Gamma_{S,\text{ph}}\right)\tilde{a}_S(t) + i\Lambda^{\text{SP}}[\alpha_P(t)]^2 e^{-i\Delta_\omega t}\tilde{a}_I^\dagger(t) + \\ &- i\left(\sqrt{\frac{2v_S^2(1-\sigma)}{L}}\right)^* \tilde{\psi}_S(0^-,t) - i\left(\sqrt{\frac{2v_S^2(1-\sigma_{\text{ph}})}{L}}\right)^* \tilde{\psi}_{S,ph}(0^-,t),\end{aligned} \tag{2.31}$$

$$\begin{aligned}\frac{d\tilde{a}_I^\dagger(t)}{dt} &= \left(i\Lambda^{\text{XPM}}|\alpha_P(t)|^2 - i\Delta_P - \Gamma_I - \Gamma_{I,\text{ph}}\right)\tilde{a}_I^\dagger(t) - i\Lambda^{\text{SP}}[\alpha_P(t)^*]^2 e^{i\Delta_\omega t}\tilde{a}_S(t) + \\ &- i\left(\sqrt{\frac{2v_I^2(1-\sigma)}{L}}\right)^* \tilde{\psi}_I(0^-,t) - i\left(\sqrt{\frac{2v_I^2(1-\sigma_{\text{ph}})}{L}}\right)^* \tilde{\psi}_{I,ph}(0^-,t),\end{aligned} \tag{2.32}$$

where $\tilde{a}_J(t) = \hat{a}_J(t)e^{i(\omega_J-\Delta_P)t}$ and $\tilde{\psi}_J(0^-,t) = \hat{\psi}_J(0^-,t)e^{i(\omega_J-\Delta_P)t}$ are rotating-frame operators, $\hat{\psi}_J(0^-,t)$ are the channel operators immediately before the coupling point to the ring, $\Gamma_J = \frac{v_J(1-\sigma_{\text{ph}})}{L}$ are the damping rates due to channel coupling or intrinsic losses, and $\Delta_\omega = 2\omega_P - \omega_S - \omega_I$. The coupled equations Eq. (2.31) and Eq. (2.32) can be written in compact matrix form as:

$$\frac{d}{dt}\begin{pmatrix}\tilde{a}_S(t)\\ \tilde{a}_I^\dagger(t)\end{pmatrix} = M_{\text{SP-SFWM}}(t)\begin{pmatrix}\tilde{a}_S(t)\\ \tilde{a}_I^\dagger(t)\end{pmatrix} + D_{\text{SP-SFWM}}(t), \tag{2.33}$$

with $M_{\text{SP-SFWM}}(t)$ describing the effects of the resonant fields, and $D_{\text{SP-SFWM}}(t)$ describing the effects of the external couplings.

2.2.2 Output Modes and Correlation Functions

Eq. (2.33) can be solved by the Green function method. The Green matrix is defined by the relations:

$$G(t_0,t_0) = \mathbb{1}, \tag{2.34}$$

$$\frac{\partial G(t,t')}{\partial t} - M_{\text{SP-SFWM}}(t)G(t,t') = \delta(t-t'), \tag{2.35}$$

where $\mathbb{1}$ is the 2×2 identity matrix. The full solution for the fields can then be built as

$$\begin{pmatrix}\tilde{a}_S(t)\\ \tilde{a}_I^\dagger(t)\end{pmatrix} = G(t,t_0)\begin{pmatrix}\tilde{a}_S(t_0)\\ \tilde{a}_I^\dagger(t_0)\end{pmatrix} + \int_{-\infty}^{t} dt'\,\Theta(t-t')G(t,t')D_{\text{SP-SFWM}}(t'), \tag{2.36}$$

where $\Theta(t-t')$ is the Heaviside step function.

Besides the formal time evolution of the signal and idler operators, the Green function gives a more direct insight into the quantum statistical properties of the generated squeezed light, such as the mean number of photons and the squeezing level. In general, it can be shown that a multimode squeezed state, is completely characterized by two second-order correlation functions, known as the N and M moments. The N moment is a multimode and multitime generalization of the mean output photon number, quantifying the intensity correlations, and is defined as (cf. Eq. (400) of Quesada *et al.* [40]):

$$N_J(t_1, t_2) \equiv v_J \langle \tilde{\psi}_J^\dagger(0^+, t_1) \tilde{\psi}_J(0^+, t_2) \rangle. \tag{2.37}$$

The M moment describes the most general correlations between non-degenerate modes J and K:

$$M_{JK}(t_1, t_2) \equiv \sqrt{v_J v_K} \langle \tilde{\psi}_J(0^+, t_1) \tilde{\psi}_K(0^+, t_2) \rangle. \tag{2.38}$$

Here $\tilde{\psi}_J(0^+, t_1)$ is the output field operator in mode J, which should be intended as a Schmidt mode, namely one of the linear independent modes resulting after a Schmidt decomposition of the dynamic matrices [68].

The N and M correlation functions provide complete statistical information about the generated quantum state, enabling calculation of all experimentally accessible quantities. In this framework, the mean photon numbers for each Schmidt mode are:

$$\langle n_J(t) \rangle = N_{J,J}(t, t), \tag{2.39}$$

and the quadrature variance spectrum measured by a local oscillator with phase θ is expressed as (cf. Eq. (422) of Quesada *et al.* [40]) :

$$\mathfrak{V}(\omega) = 1 + N_S(\omega, \omega) + N_S(-\omega, -\omega) + 2\,\mathrm{Re}[e^{-2i\theta} M_{SS}(\omega, -\omega)], \tag{2.40}$$

where $N_S(\omega, \omega')$ and $M_{SS}(\omega, \omega')$ are the Fourier transforms of the temporal correlation functions. The squeezing level is determined by the minimum value of $\mathfrak{V}(\omega)$ over all local oscillator phases.

Using the Green function solution, the explicit expressions for N and M correlation functions can be calculated (cf. Eq. (402) and Eq. (403) of Quesada *et al.* [40]):

$$N_S(t_1, t_2) = 4\overline{\Gamma}_S \overline{\Gamma}_I \int d\tau\, G_{12}^*(t_1, \tau)\theta(t_1 - \tau) G_{12}(t_2, \tau)\theta(t_2 - \tau), \tag{2.41}$$

$$\begin{aligned} M_{SI}(t_1, t_2) = 2\Gamma_S \int d\tau\, G_{11}(t_1, \tau)\theta(t_1 - \tau) G_{21}^*(t_2, \tau)\theta(t_2 - \tau) - 2\sqrt{\eta_S \eta_I \overline{\Gamma}_S \overline{\Gamma}_I} \\ (\overline{\Gamma}_S + \overline{\Gamma}_I) \int d\tau\, [G_{21}^*(t_1, \tau) G_{22}^*(t_2, \tau) - G_{22}^*(t_1, \tau) G_{21}^*(t_2, \tau)]\theta(t_2 - t_1)\theta(t_1 - \tau), \end{aligned} \tag{2.42}$$

where $G_{ij}(t, t')$ denote the matrix elements of the Green function, η_J is the energy transmission after accounting for intrinsic losses, and $\overline{\Gamma}_J = \Gamma_J + \Gamma_{J,\mathrm{ph}}$.

2.3 Asymptotic-Fields Formalism

The Lorentzian model introduced in the previous section provides a rigorous description of spontaneous four-wave mixing (SFWM) in high-quality ring resonators, where the resonances are well isolated and can be approximated as ideal Lorentzians. However, this approach becomes less accurate in complex devices featuring resonance splitting or suppression. In this case, a more precise description of the electromagnetic fields in the structure is required. The asymptotic-field formalism proposed by Liscidini *et al.* in 2012 [69] offers such a framework, providing a rigorous way to connect the linear properties of the device with its quantum nonlinear dynamics for a variety of parametric processes. In this section, we review this method in the specific case of SP-SFWM.

2.3.1 Asymptotic-in and Asymptotic-out Fields

In the asymptotic-fields formalism, an integrated structure is described as an interaction region, where nonlinear processes can take place, with a set of channels representing the only pathways for light to enter or leave the interaction region, as sketched in Fig. 2.5. For instance, in a ring resonator, the ring is the interaction region, and the bus waveguide forms two channels. If one defines a phantom channel representing losses, as was done in the previous section, then an additional channel will enter into the picture, which is the output part of the phantom channel.

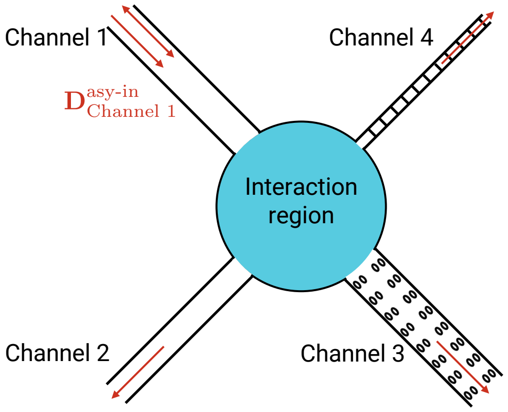

Figure 2.5: Scheme of the structure considered in the asymptotic-in formalism. Some channels, which may not all have the same characteristics, connect an interaction region (blue shaded area) to the outside. The red arrows represent the direction of an asymptotic-in field associated with Channel 1 at the four input/output ports of the structure. It is important to note that the asymptotic field is defined everywhere in space. The figure has been adapted with permission from [69].

An *asymptotic-in(-out) field* propagating in a channel ch with mode J is defined as the full solution of Maxwell's equations when light is injected(extracted) from that mode of that channel only, and only linear interactions are present. For ease of notation, we identify the modes through the sole index J, incorporating also the information about the channel, and we drop the index $c\hbar$. The displacement operator can then be expanded on the asymptotic-in basis as

$$\mathbf{D}(\mathbf{r}) = \sum_J \int_0^\infty d\omega \sqrt{\frac{\hbar\omega}{2v_{g,J}(\omega)}}\, \hat{a}^{\text{in}}_{\omega J}\, \mathbf{D}^{\text{asy-in}}_{\omega J}(\mathbf{r}) + \text{H.c.}, \tag{2.43}$$

and on the asymptotic-out basis as

$$\mathbf{D}(\mathbf{r}) = \sum_J \int_0^\infty d\omega \sqrt{\frac{\hbar\omega}{2v_{g,J}(\omega)}}\, \hat{a}^{\text{out}}_{\omega J}\, \mathbf{D}^{\text{asy-out}}_{\omega J}(\mathbf{r}) + \text{H.c.}, \tag{2.44}$$

where $\hat{a}^{\text{in}}_{\omega J}$ and $\hat{a}^{\text{out}}_{\omega J}$ are the annihilation operators for the asymptotic-in and -out modes of frequency ω, and $\mathbf{D}^{\text{asy-in (-out)}}_{\omega J}(\mathbf{r})$ are the corresponding normalized mode profiles. It can be shown that, in the absence of loss, the asymptotic-out fields are the Hermitian conjugates of the corresponding asymptotic-in fields, and both constitute a complete, orthonormal basis in the mode space [69].

Each asymptotic-in mode can be separated into a longitudinal and a transverse contribution,

$$\mathbf{D}^{\text{asy-in}}_{\omega J}(\mathbf{r}) = \frac{e^{ik(\omega)\zeta}}{\sqrt{2\pi}} A_{\omega J}(\zeta)\, \mathbf{d}_{\omega J}(\mathbf{r}_\perp, \zeta), \tag{2.45}$$

where $A_{\omega J}(\zeta)$ is the longitudinal amplitude that we introduced in Chapter 1 when analyzing the scattering-matrix theory and $\mathbf{d}_{\omega J}(\mathbf{r}_\perp, \zeta)$ is the transverse displacement field profile, whose ζ dependence is only due to the variation of direction along the ring. The field is normalized as [70]:

$$\int d\mathbf{r}_\perp \frac{\mathbf{d}^*_{\omega J}(\mathbf{r}_\perp)\mathbf{d}_{\omega J}(\mathbf{r}_\perp)}{\epsilon_0 \epsilon_r(\mathbf{r}_\perp;\omega)} \frac{v_p(\mathbf{r}_\perp;\omega)}{v_g(\mathbf{r}_\perp;\omega)} = 1. \tag{2.46}$$

2.3.2 Nonlinear Hamiltonian

As before, the SFWM Hamiltonian is built by substituting the mode expansion Eqs. (2.43-2.44) into the general third-order nonlinear Hamiltonian Eq. (1.45), retaining only the terms corresponding to the annihilation of two pump photons and the creation of a signal-idler pair. It is convenient to express the pump fields in terms of asymptotic-in modes, while signal and idler are described by asymptotic-out modes. The resulting SP-SFWM Hamiltonian is [69, 71]

$$\begin{aligned}\hat{\mathscr{H}}^{(\text{SFWM})} = &- \frac{1}{4\varepsilon_0} \frac{4!}{2!2!} \int_{S\cup I} d\omega_1 \int_{S\cup I} d\omega_2 \int_P d\omega_3 \int_P d\omega_4 \hat{a}_1^\dagger \hat{a}_2^\dagger \hat{a}_3 \hat{a}_4 \frac{\hbar^2 \sqrt{\omega_1\omega_2\omega_3\omega_4}}{4v_g^2} \\ &\int d\mathbf{r} \Gamma^{(3)}_{ijlm}(\mathbf{r}) D^{\text{asy}-\text{in}*}_{1,i}(\mathbf{r}) D^{\text{asy}-\text{in}*}_{2,j}(\mathbf{r}) D^{\text{asy}-\text{in}}_{3,l}(\mathbf{r}) D^{\text{asy}-\text{in}}_{4,m}(\mathbf{r}) + H.c.,\end{aligned} \tag{2.47}$$

where we considered single-mode channels (so that we could drop the J index) and introduced the notation $\hat{a}_\chi := \hat{a}^{\text{in}}_{\omega_\chi}$, $\mathbf{D}^{\text{asy-in}}_\chi(\mathbf{r}) = \mathbf{D}^{\text{asy-in}}_{\omega_\chi}(\mathbf{r})$. Here we used the fact that asymptotic-in and -out fields are Hermitian conjugates, and the factor $\frac{4!}{2!2!}$ arises from the fact that signal-idler pairs, as well as pump-pump pairs, are made of indistinguishable photons. It must be noted that here, the indices $1, 2, 3, 4$ do not correspond exactly to signal, idler, and pump modes. Rather, 1 and 2 identify two distinct frequencies that are associated with the asymptotic-out modes and run over the union of the signal and idler spectral regions, while indices 3 and 4 identify the two frequencies associated with the asymptotic-in modes and run over the pump spectral region.

Eq. (2.47) is conveniently rewritten as

$$\hat{\mathcal{H}}^{(\text{SFWM})} = -\int d\omega_1 d\omega_2 d\omega_3 d\omega_4 \hat{a}^\dagger_1 \hat{a}^\dagger_2 \hat{a}_3 \hat{a}_4 \sqrt{\omega_1\omega_2\omega_3\omega_4} S_\perp \mathcal{G}(\omega_1, \omega_2, \omega_3, \omega_4) + H.c., \tag{2.48}$$

where

$$S_\perp = \frac{3\hbar^2}{8\varepsilon_0 v_g^2} \int d\mathbf{r}_\perp \frac{\Gamma^{(3)}_{ijlm}(\mathbf{r}_\perp)}{4\pi^2} d^*_{1,i}(\mathbf{r}_\perp) d^*_{2,j}(\mathbf{r}_\perp) d_{3,l}(\mathbf{r}_\perp) d_{4,m}(\mathbf{r}_\perp), \tag{2.49}$$

contains the overlap of the transverse parts of the modes, which are assumed to be identical for simplicity, and the longitudinal overlap integral is

$$\mathcal{G}(\omega_1, \omega_2, \omega_3, \omega_4) = \int d\zeta \, e^{i\Delta k\zeta} A^*_1(\zeta) A^*_2(\zeta) A_3(\zeta) A_4(\zeta). \tag{2.50}$$

Here, the integral runs over the entire structure, including all waveguides in both the channel and the interaction region. It is often convenient to decompose this integral in a set of integrals associated with different waveguides, which we identify through an index w:

$$\mathcal{G}(\omega_1, \omega_2, \omega_3, \omega_4) = \sum_w \int_{L_w} d\zeta \, e^{i\Delta k\zeta} A^*_{1,w}(\zeta) A^*_{2,w}(\zeta) A_{3,w}(\zeta) A_{4,w}(\zeta), \tag{2.51}$$

where L_w is the waveguide's length, and $\Delta k = k(\omega_1) + k(\omega_2) - k(\omega_3) - k(\omega_4)$ the phase mismatch.

The transverse overlap integral can be related to the nonlinear parameter [71]

$$\gamma_{\text{NL}} = \frac{3\omega_P}{4\varepsilon_0 v_g^2} \int d\mathbf{r}_\perp \frac{\Gamma^{(3)}_{ijlm}(\mathbf{r}_\perp)}{4\pi^2} d^*_i(\mathbf{r}_\perp) d^*_j(\mathbf{r}_\perp) d_l(\mathbf{r}_\perp) d_m(\mathbf{r}_\perp) \tag{2.52}$$

by

$$S_\perp = \gamma_{NL} \frac{\hbar^2}{8\pi^2\omega_p}, \tag{2.53}$$

where ω_p is the central pump frequency, v_g the group velocity of the guided mode, and we neglected the spectral dependency of $\mathbf{d}_\omega(\mathbf{r}_\perp, \zeta)$.

2.3.3 Low-Gain Generation Rate

The quantum state generated by SFWM is fundamentally a multi-mode squeezed state. Following the approach of Yang *et al.* [70], it can be written in the general form:

$$|\psi\rangle = e^{\frac{\beta}{\sqrt{2}}\int d\omega_1 d\omega_2 \phi(\omega_1,\omega_2)\hat{a}_1^\dagger \hat{a}_2^\dagger - \text{H.c.}}|\text{vac}\rangle, \tag{2.54}$$

where $|\beta|$ is a generalized squeezing parameter and $\phi(\omega_1,\omega_2)$ is the joint probability amplitude to detect one generated photon at frequency ω_1 and one at frequency ω_2. $\phi(\omega_1,\omega_2)$ is often called the biphoton wavefunction, for its resemblance to the wavefunction appearing in the Schrödinger equation. However, when using this notation, one should be aware that this is a probability amplitude in the spectral domain rather than in the spatial domain. In the limit of a small β, this state can be approximated as:

$$|\psi\rangle \approx |\text{vac}\rangle + \frac{\beta}{\sqrt{2}}\int d\omega_1 d\omega_2 \phi(\omega_1,\omega_2)\hat{a}_1^\dagger \hat{a}_2^\dagger \left|\text{vac}\right\rangle. \tag{2.55}$$

In this case, $|\beta|^2$ can be interpreted as the mean number of photon pairs generated per pump pulse.

In the low-gain regime, in the undepleted pump approximation, the biphoton wavefunction can be calculated in a backward Heisenberg picture [70], as outlined in [70, 71, 72, 73]. The result is

$$\begin{aligned}\phi(\omega_s,\omega_i) =& \frac{2\sqrt{2}\pi\alpha_P^2}{\beta}\frac{i}{\hbar}\int d\omega_3 d\omega_4 \sqrt{\omega_1\omega_2\omega_3\omega_4} S_\perp \phi_{P1}(\omega_3)\phi_{P2}(\omega_4)\\ & \mathcal{J}(\omega_1,\omega_2,\omega_3,\omega_4)\delta(\omega_1+\omega_2-\omega_3-\omega_4) =\\ =& \frac{i\hbar\gamma_{NL}\alpha_P^2}{2\sqrt{2}\pi\omega_p\beta}\int d\omega_3 \sqrt{\omega_1\omega_2\omega_3(\omega_1+\omega_2-\omega_3)}\phi_P(\omega_3)\phi_P(\omega_1+\omega_2-\omega_3)\\ & \mathcal{J}(\omega_1,\omega_2,\omega_3,\omega_1+\omega_2-\omega_3),\end{aligned} \tag{2.56}$$

where $\phi_P(\omega)$ is the spectral amplitude of the pump fields and $|\alpha_P|^2$ is the average number of pump photons. It must be stressed that Eq. (2.56) is only valid up to a first-order expansion of the time-ordering operator that appears when evolving an input pump pulse through the nonlinear Hamiltonian Eq. (2.48).

Since the biphoton wavefunction is a probability amplitude, it must satisfy the normalization condition:

$$\int_0^\infty \int_0^\infty |\phi(\omega_1,\omega_2)|^2 d\omega_1 d\omega_2 = 1. \tag{2.57}$$

As a consequence the average number of generated pairs is:

$$|\beta|^2 = \int_0^\infty \int_0^\infty \left|\beta\phi(\omega_1,\omega_2)\right|^2 d\omega_1 d\omega_2. \tag{2.58}$$

In the limit of a long pump pulse duration ΔT, keeping the pump power $\mathscr{P}_P$ constant, the integration becomes analytical. In this continuous-wave regime, the generation rate per unit time should be considered rather than the number of pairs per pulse. It can be shown that this rate is [73]:

$$\mathfrak{R} = \frac{|\beta|^2}{\Delta T} = \frac{\gamma_{\mathrm{NL}}^2 \mathscr{P}_P^2}{4\pi\omega_P^2} \int_0^\infty d\omega_1 \omega_1 (2\omega_P - \omega_1) |\mathcal{J}(\omega_1, 2\omega_P - \omega_1, \omega_P, \omega_P)|^2, \quad (2.59)$$

where ω_P is the pump frequency. Eq. (2.59) only involves an integral of the linear classical field amplitudes, making it very efficient in terms of computational resources. Additionally, the result was derived without any assumption about the shape of the field spectrum, making it suitable to describe split, low-finesse, resonances and even non-resonant devices.

This asymptotic fields approach allows one to extract both the spectral properties of the generated pairs, through the biphoton wavefunction, and the overall generation efficiency in the low-gain regime for complex integrated photonic structures. From a Schmidt decomposition of the biphoton wavefunction, other properties such as the entanglement, purity, and temporal coherence of the two-photon state can be derived [68, 74, 75]. Losses can be either accounted directly by using a complex wavevector, as outlined in 1, or modeled through a phantom channel similar to the one used in the Lorentzian model. The first approach provides a more realistic description of the field distribution within the ring. The latter enables the full calculation of the number of photons that are generated and then lost to non-radiative modes, which are represented by the phantom channel.

2.4 Local Modes for the High-Gain Regime

The Lorentzian and asymptotic-fields formalisms presented in the previous sections provide an accurate modeling of SFWM in their regimes of validity. The first, describes high-quality ring resonators with well-isolated Lorentzian resonances even in the high-gain regime and in the presence of competing parametric processes. The latter, offers a general framework applicable even to complex device geometries but has previously been limited to perturbative calculations that cannot reconstruct the complete quantum state required for high-gain squeezing analyses. Extending it to the non-perturbative regime is challenging due to the two key assumptions of small generation rate and first-order expansion of the time-ordering operator. The first is used to approximate the squeezing parameter to the average number of generated photon pairs, and the second is essential to write the biphoton wavefunction in a closed form. Relaxing either of these assumptions would result in treating the exponential of non-trivially commuting creation operators, which rapidly becomes intractable even with a modest number of modes.

In the following section, we present an approach to extend the asymptotic fields into the high-gain regime, taking advantage of some results from the

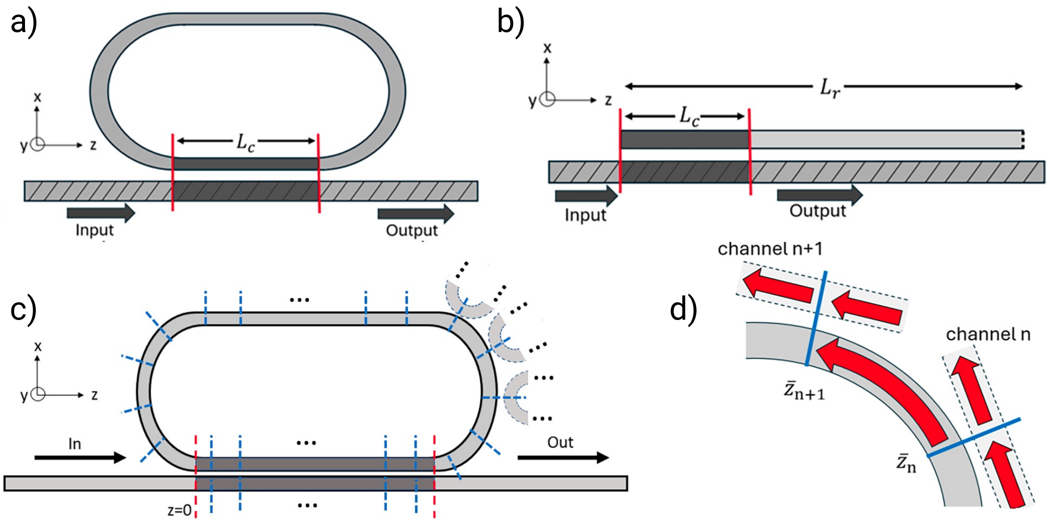

Figure 2.6: (a) Ring resonator side-coupled to a channel waveguide. The darker shaded area represents the coupler, of length L_c (b) Linearized representation of the same ring. (c) Phantom-channel model for the losses. Each blue dashed line represent the coupling point of a phantom channel. Three phantom channels are sketched on the right. We allow the coupler to be lossy, by introducing phantom channels inside it. (d) Sample local mode with a finite field amplitude only in the region between two adjacent phantom channel. This is obtained by a proper linear combination of the asymptotic-in fields associated with the two adjacent channels. Images taken from [76].

Lorentzian model while maintaining the ability to describe complex device geometries and realistic loss mechanisms. [76].

2.4.1 Local Basis Construction

We consider a racetrack resonator of length L_r side-coupled to a bus waveguide through a directional coupler of length L_c, as shown in Fig. 2.6(a). We approximate this ring resonator as a linearized structure, as illustrated in Fig. 2.6(b): when the bending radius of the curved regions is large enough that field distribution variations are negligible, we can consider the field profile inside the ring identical to the one of the bus waveguide. This means we can take one unified frame of reference with all fields propagating in the z direction, representing the coupled ring-waveguide system as a pair of straight waveguides that couple only for part of their length and with the ring waveguides having periodic boundary conditions.

We describe losses through a set of N_L phantom channels, as sketched in Fig. 2.6(c) such that the sum of all the coupling probabilities κ_n^2 is equal to the round-trip loss. Here, the bus waveguide is indexed by $n = 0$ while the phantom channels are indexed by $n \in 1, ...N_L$. This approach offers two advantages compared to the single phantom channel. First, the unitary evolution of generated and lost photons is properly tracked throughout the whole structure. Second, it divides the interaction region in $N_L + 1$ sections, which will be useful later to define localized modes that exist only in one of these sections and are null elsewhere. We allow the directional coupler to be lossy by putting some of the N_L phantom channels in the interaction region. In this case, for each channel coupled to the ring at position $\bar{z}_n$, we add a phantom channel coupled to the waveguide at the same position $\bar{z}_n$.

We start from the asymptotic field decomposition of the displacement field Eq. (2.43), but we introduce a key modification. Instead of considering spectral regions spanning all frequencies, we limit each asymptotic mode to a narrow spectral region around a ring resonance, similar to what was done in the Lorentzian model (see Fig. 2.4). However, unlike the Lorentzian approach, we allow the wavevector to vary in the range $\mathscr{R}_J$ around the central value k_J not only for the channel operators, but also for the ring operators Within this range, the resonant modes are expanded in terms of the $N_L + 1$ asymptotic fields associated with the phantom channel and bus waveguide, enabling a more complete description of the field dynamics. The resulting displacement field is expanded as:

$$\mathbf{D}(\mathbf{r}, t) = \sum_{J,n} \int_{\mathscr{R}_J} dk \sqrt{\frac{\hbar\omega_J}{2}} \mathbf{D}^{\text{asy-in}}_{k,J,n}(\mathbf{r}) \hat{a}^{\text{in}}_{k,J,n}(t) + \text{H.c.} \tag{2.60}$$

where $n = 0$ identifies the bus waveguide, $n > 0$ runs over the phantom channels, J runs over all resonance ranges involved in the nonlinear process of interest, and

$$\mathbf{D}^{\text{asy-in}}_{k,J,n}(\mathbf{r}) = \frac{e^{ik_J z}}{\sqrt{2\pi}} \mathbf{d}_{k,J}(\mathbf{r}_\perp) A^{\text{in}}_{k,J,n}(z) \tag{2.61}$$

is the wavevector-domain analogous of the frequency-domain asymptotic-in field introduced in the previous section. Here $A^{\text{in(out)}}_{k,J,n}(z)$ and $\mathbf{d}_{k,J}(\mathbf{r}_\perp)$ are the longitudinal and transverse amplitudes in the wavevector domain. For simplicity, we approximate $\mathbf{d}_{k,J}(\mathbf{r}_\perp)$ to be equal in all the channels and in the ring, although this assumption can be relaxed [76].

The asymptotic fields rigorously describe all the modes within the structure. However, they are defined in all space, meaning they all interact with each other, making any non-perturbative calculation intractable even for a modest number of phantom channels. For this reason, we perform a change of basis constructing local modes of the form [76]:

$$\mathbf{D}^{\text{loc}}_{k,J,n}(\mathbf{r}) = \mathbf{D}^{\text{asy-in}}_{k,J,n}(\mathbf{r}) - \frac{\kappa_n}{\kappa_{n+1}} \sigma_{n+1} \mathbf{D}^{\text{asy-in}}_{k,J,n+1}(\mathbf{r}) e^{ik(\bar{z}_{n+1} - \bar{z}_n)}, \tag{2.62}$$

where the wavevector varies in the range $\mathscr{R}_J$, $\bar{z}_n$ and $\bar{z}_{n+1}$ are the positions of two adjacent phantom channels. This construction ensures that, as detailed in Fig. 2.6(d), the local field has nonzero support only in the two phantom channels and in the ring area between the coupling points $\bar{z}_n$ and $\bar{z}_{n+1}$, dramatically simplifying the overlap integrals required for the nonlinear calculations.

A similar argument holds in the interaction region, although here the relation between asymptotic and local fields involves two pairs of phantom channels: one for the ring and one for the waveguide.

The transformation between local and asymptotic bases is captured by the matrix equation [76]:

$$\begin{pmatrix} \mathbf{D}^{\text{loc}}_{k,J,0}(\mathbf{r}) \\ \mathbf{D}^{\text{loc}}_{k,J,1}(\mathbf{r}) \\ \vdots \\ \mathbf{D}^{\text{loc}}_{k,J,N_L}(\mathbf{r}) \end{pmatrix} = \mathbf{L}^{\text{in}}_{k,J} \begin{pmatrix} \mathbf{D}^{\text{asy-in}}_{k,J,0}(\mathbf{r}) \\ \mathbf{D}^{\text{asy-in}}_{k,J,1}(\mathbf{r}) \\ \vdots \\ \mathbf{D}^{\text{asy-in}}_{k,J,N_L}(\mathbf{r}) \end{pmatrix} \tag{2.63}$$

Correspondingly, the operators transform with the inverse-transpose of the transformation matrix:

$$\begin{pmatrix} \hat{a}^{\text{loc}}_{k,J,0}(t) \\ \hat{a}^{\text{loc}}_{k,J,1}(t) \\ \vdots \\ \hat{a}^{\text{loc}}_{k,J,N_L}(t) \end{pmatrix} = \left(\mathbf{L}^{\text{in},-1}_{k,J}\right)^T \begin{pmatrix} \hat{a}^{\text{in}}_{k,J,0}(t) \\ \hat{a}^{\text{in}}_{k,J,1}(t) \\ \vdots \\ \hat{a}^{\text{in}}_{k,J,N_L}(t) \end{pmatrix} \tag{2.64}$$

The transformation matrix $\mathbf{L}^{\text{in}}_{k,J}$ can be built from knowledge of only the longitudinal field $A^{\text{in}}_{k,J,n}(z)$, which is transformed into a local longitudinal field $A^{\text{loc}}_{k,J,n}(z)$. In analogy to the asymptotic-in construction, these same local modes can be derived from the asymptotic-out fields.

We point out that the local-mode operators do not satisfy the usual commutation relations, because

$$[\hat{a}^{\text{loc}}_{k,J,n}(t), \hat{a}^{\text{loc}}_{k',J',n'}(t)] = 0, \tag{2.65}$$

but

$$[\hat{a}^{\text{loc}}_{k,J,n}(t), \hat{a}^{\text{loc}\dagger}_{k',J',n'}(t)] = \delta_{J,J'}\delta(k-k')C^{k,J}_{n,n'}, \tag{2.66}$$

with

$$C^{k,J}_{n,n'} = \sum_{m=0}^{N_L} \left(\mathbf{L}^{\text{in},-1}_{k,J}\right)^*_{n',m} \left(\mathbf{L}^{\text{in},-1}_{k,J}\right)_{n,m}.$$

Still, the local modes constitute a complete basis for the displacement field, nonetheless. The corresponding decomposition,

$$\mathbf{D}(\mathbf{r},t) = \sum_{J,n} \int_{\mathcal{R}_J} dk \sqrt{\frac{\hbar\omega_{k,J}}{2}} \mathbf{D}^{\text{loc}}_{k,J,n}(\mathbf{r}) \hat{a}^{\text{loc}}_{k,J,n}(t) + \text{H.c.}, \tag{2.67}$$

is obtained by substituting Eqs. (2.63-2.64) in Eq. (2.60).

2.4.2 Nonlinear Hamiltonian and Time Evolution

We expand the third-order nonlinear Hamiltonian on the local basis following the calculations that led to Eq. (2.48):

$$\begin{aligned}\mathscr{H}^{(\mathrm{NL})} = &-\frac{\hbar^2}{8\pi^2}\sum_{\mathbf{J},\mathbf{n}}\int d\mathbf{k}\gamma^{\mathbf{J}}_{NL}\,\mathscr{G}_{\mathbf{J},\mathbf{k},\mathbf{n}}v_g^2\sqrt[4]{\omega_1\omega_2\omega_3\omega_4}\\ &\times\hat{a}^{\mathrm{loc}\dagger}_{k_1,J_1,n_1}(t)\hat{a}^{\mathrm{loc}\dagger}_{k_2,J_2,n_2}(t)\hat{a}^{\mathrm{loc}}_{k_3,J_3,n_3}(t)\hat{a}^{\mathrm{loc}}_{k_4,J_4,n_4}(t).\end{aligned} \tag{2.68}$$

Here, $\mathbf{J}=\{J_1,J_2,J_3,J_4\}$, $\mathbf{n}=\{n_1,n_2,n_3,n_4\}$, $d\mathbf{k}=dk_1dk_2dk_3dk_4$, $\omega_\chi=\omega_{k_\chi,J_\chi}$,

$$\mathscr{G}_{\mathbf{J},\mathbf{k},\mathbf{n}}=\int dzA^{\mathrm{in}}_{k_1,J_1,n_1}(z)A^{\mathrm{in}}_{k_2,J_2,n_2}(z)A^{\mathrm{in}}_{k_3,J_3,n_3}(z)A^{\mathrm{in}}_{k_4,J_4,n_4}(z)e^{-i\,\Delta k^0_{\mathbf{J}}\,z},$$

is the longitudinal overlap integral with $\Delta k^0_{\mathbf{J}}=k_1+k_2-k_3-k_4$ the zero-th order wavevector mismatch, and

$$\gamma^{\mathbf{J}}_{\mathrm{NL}}=\frac{3\sqrt[4]{\omega_1\omega_2\omega_3\omega_4}}{4\varepsilon_0v_g^2}\int d\mathbf{r}_\perp\frac{\Gamma^{(3)}_{ijlm}(\mathbf{r}_\perp)}{4\pi^2}d^*_{J_1,i}(\mathbf{r}_\perp)d^*_{J_2,j}(\mathbf{r}_\perp)d_{J_3,l}(\mathbf{r}_\perp)d_{J_4,m}(\mathbf{r}_\perp)$$

is the nonlinear coefficient associated with modes $\mathbf{J}$. The latter is similar to the coefficient introduced in Eq. (2.52), but it is generalized to an arbitrary $\chi^{(3)}$ process defined by the set of resonances $\mathbf{J}$.

In Eq. (2.68), all possible $\chi^{(3)}$ processes are taken into account simultaneously. For instance, SP-SFWM is associated with modes $\mathbf{J}=(S,I,P,P)$, but one can include DP-SFWM by choosing the modes $\mathbf{J}=(S,I,P,P)$, or SPM with modes $\mathbf{J}=(P,P,P,P)$.

We now consider a SP-SFWM process with arbitrary gain, and include SPM and XPM. The equations of motion for the local mode are obtained from the Heisenberg equation Eq. (2.30), involving a commutator of the local operator with the full Hamiltonian. We first compute the linear term:

$$\begin{aligned}&\frac{\partial d}{\partial t}\hat{a}^{\mathrm{loc}}_{\overline{k},I,m}(t)=\frac{i}{\hbar}\sum_{J,n}\int_{\mathscr{R}_J}dk\hbar\omega_{k,J}[\hat{a}^{\mathrm{in}\dagger}_{k,J,n}(t)\hat{a}^{\mathrm{in}}_{k,J,n}(t),\hat{a}^{\mathrm{loc}}_{\overline{k},I,m}(t)]=\\ &=i\sum_{J,n}\int_{\mathscr{R}_J}dk\omega_{k,J}\sum_j\left(\mathbf{L}^{\mathrm{in},-1}_{\overline{k},I}\right)_{j,m}[\hat{a}^{\mathrm{in}\dagger}_{k,J,n}(t)\hat{a}^{\mathrm{in}}_{k,J,n}(t),\hat{a}^{\mathrm{in}}_{\overline{k},I,j}(t)]=\\ &=-i\sum_{J,n,j}\int_{\mathscr{R}_J}dk\omega_{k,J}\left(\mathbf{L}^{\mathrm{in},-1}_{\overline{k},I}\right)_{j,m}\delta_{I,J}\delta(k-\overline{k})\delta_{j,n}\hat{a}^{\mathrm{in}}_{k,J,n}(t)=\\ ,&=-i\sum_j\omega_{\overline{k},I}\left(\mathbf{L}^{\mathrm{in},-1}_{\overline{k},I}\right)_{j,m}\hat{a}^{\mathrm{in}}_{\overline{k},I,j}(t)=\\ &=-i\omega_{\overline{k},I}\hat{a}^{\mathrm{loc}}_{\overline{k},I,m}(t).\end{aligned} \tag{2.69}$$

Similarly, one can compute the full equations of motion [76]:

$$\frac{\partial}{\partial t}\hat{a}^{\mathrm{loc}}_{\overline{k},I,m}(t) = -i\omega_{\overline{k},I}\hat{a}^{\mathrm{loc}}_{\overline{k},I,m}(t) + \frac{i\hbar}{4\pi^2}\sum_{\mathbf{J},\mathbf{n}}\int d\mathbf{k}\gamma^{\mathbf{J}}_{NL}\,\mathcal{G}_{\mathbf{J},\mathbf{k},\mathbf{n}}v_g^2\sqrt[4]{\omega_1\omega_2\omega_3\omega_4}g_{\mathbf{J}}\mathcal{C}^{\overline{k},I}_{n_1,m} \times \hat{a}^{\mathrm{loc}\dagger}_{k_2,J_2,n_2}(t)\hat{a}^{\mathrm{loc}}_{k_3,J_3,n_3}(t)\hat{a}^{\mathrm{loc}}_{k_4,J_4,n_4}(t)\delta_{J_1,I}\delta(k_1-\overline{k}), \tag{2.70}$$

where the first term is the linear evolution and the second term is the sum of all nonlinear contributions, with $\mathbf{J} \in \{(S,I,P,P); (P,P,P,P); (S,P,S,P); (I,P,I,P)\}$ and

$$g_{\mathbf{J}} = \begin{cases} 2 if J_1 = J_2 \\ 1 if J_1 \neq J_2 \end{cases}$$

In the undepleted pump approximation, the pump field operators $\hat{a}^{\mathrm{loc}}_{k,P,n}(t)$ can be replaced by their expectation value $\alpha_P(t)$.

Eq. (2.70) can be solved numerically through a split-step method [76]. First one evolves the operators linearly for a time step $\frac{\Delta t}{2}$, which corresponds to adding k-dependent phases:

$$\hat{a}^{\mathrm{loc}}_{k,J,m}(t) \to \hat{a}^{\mathrm{loc}}_{k,J,m}(t)e^{-i\omega_{k,J}\Delta t}. \tag{2.71}$$

Subsequently, one computes the nonlinear evolution from the nonlinear part of the equations of motion for a time Δt, which involves a multiplication between the vector of local operators and a matrix that scales quadratically with the number of phantom channels, resonances, and points in the wavevector discretization. Finally, a second linear evolution of time step $\frac{\Delta t}{2}$ is performed.

While this introduces larger mode dimensionality compared to the perturbative asymptotic-fields method (which scales linearly with the number of channels and with the frequency discretization) and the Lorentzian treatment (which involves only one phantom channel), it enables a local non-perturbative treatment of the field evolution within the ring structure even beyond the high-finesse approximation. For the ring resonators we are going to study in this chapter ($L_r = 2\pi \times 120$ µm, finesse $F = 10^1 - 10^3$), convergence is achieved with $N_L = 10 - 20$ phantom channels, making the method computationally tractable, as opposed to a standard, non-perturbative asymptotic-field theory.

2.4.3 Results and Validation

We validated the local-modes treatment through comparison with established approaches across different parameter regimes. Fig. 2.7 shows the expectation value of the signal photon number generated per pump pulse as a function of the ring finesse, comparing our local-modes method with the Lorentzian and perturbative asymptotic-field treatments. For a fair comparison, we neglect here the effects of SPM and XPM, because they are not immediately integrated in a perturbative backward-Heisenberg picture. Here, we account for both the

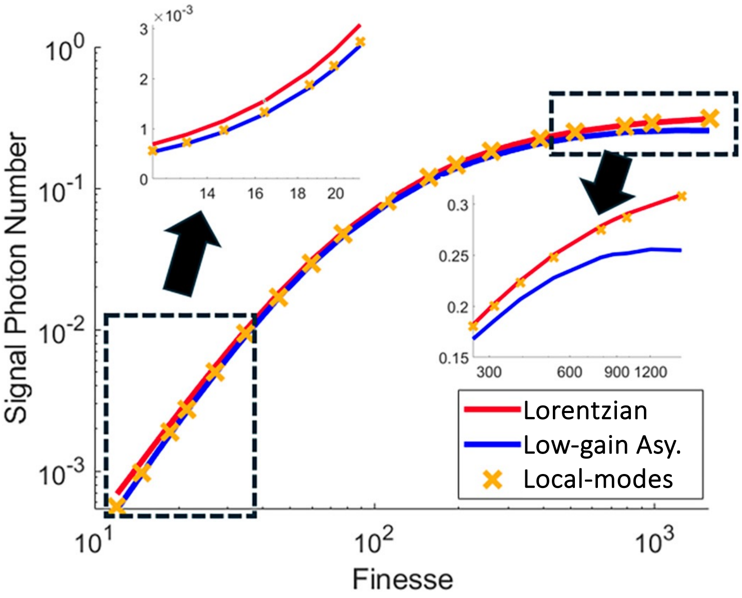

Figure 2.7: Method comparison showing the mean generated signal photon number. The asymptotic scattering method matches the PBH method in the perturbative regime and the CM-IO method in the high-finesse regime, while extending applicability beyond both. Image taken from [76].

photons coupled out to the bus waveguide and those lost to the phantom channels.

In the intermediate region, all three methods agree well, demonstrating that our method correctly reproduces established results. In addition, the local modes have a wider range of applicability compared to the other two methods. As shown in the two insets, in the low-finesse region, the Lorentzian model overestimates the generation rate because the resonances are not Lorentzian, while in the high-finesse region, the perturbative asymptotic fields underestimate it because the expected number of photons approaches 1. For these calculations, we used a Gaussian pump pulse of duration 70 ps and energy 100 pJ, and a fixed ring escape efficiency of $\eta = 0.75$.

Beyond the photon number, the knowledge of how the local-field operators evolve in time allows one to study the spectral correlations of the output state, by defining N and M correlation functions as in Eqs. (2.37-2.38). From these [77, 40], one can derive the first-order cross-correlation function

$$\begin{aligned} g^{(1,1)}_{JJ'} &= \frac{\int dt_1\, dt_2\, \langle \hat{E}^{(-)}_J(t_1)\hat{E}^{(+)}_J(t_1)\hat{E}^{(-)}_{J'}(t_2)\hat{E}^{(+)}_{J'}(t_2)\rangle}{\int dt_1\, dt_2\, \langle \hat{E}^{(-)}_J(t_1)\hat{E}^{(+)}_J(t_1)\rangle\, \langle \hat{E}^{(-)}_{J'}(t_2)\hat{E}^{(+)}_{J'}(t_2)\rangle} = \\ &= \frac{\mathrm{Tr}\left[\tilde{M}_{JJ'}\tilde{M}^{\dagger}_{JJ'}\right] + \mathrm{Tr}\left[\tilde{N}_{JJ}\right]\mathrm{Tr}\left[\tilde{N}_{J'J'}\right]}{\mathrm{Tr}\left[\tilde{N}_{JJ}\right]\mathrm{Tr}\left[\tilde{N}_{J'J'}\right]} \end{aligned} \tag{2.72}$$

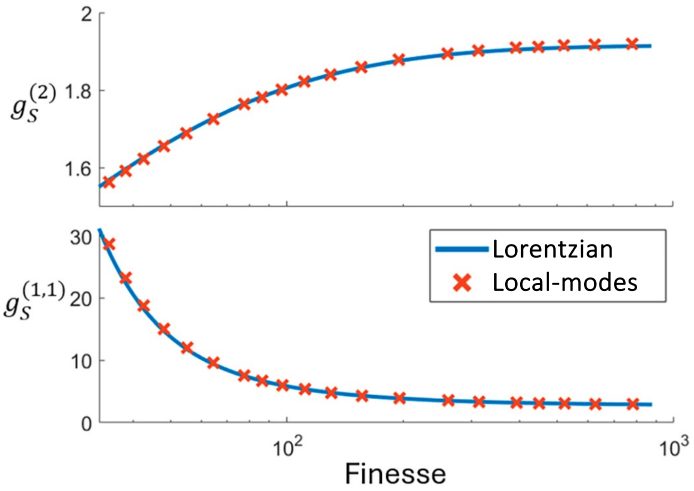

Figure 2.8: High-gain regime results showing the correlation functions $g^{(1,1)}$ and $g^{(2)}$ as a function of the ring's finesse. Image taken from [76].

and the second-order correlation function

$$g_J^{(2)} = \frac{\int dt_1\, dt_2\, \langle \hat{E}_J^{(-)}(t_1)\hat{E}_J^{(-)}(t_2)\hat{E}_J^{(+)}(t_2)\hat{E}_J^{(+)}(t_1)\rangle}{\int dt_1\, dt_2\, \langle \hat{E}_J^{(-)}(t_1)\hat{E}_J^{(+)}(t_1)\rangle \, \langle \hat{E}_J^{(-)}(t_2)\hat{E}_J^{(+)}(t_2)\rangle} = \frac{\mathrm{Tr}\left[\tilde{N}_{JJ}^2\right] + \mathrm{Tr}\left[\tilde{N}_{JJ}\right]^2}{\mathrm{Tr}\left[\tilde{N}_{JJ}\right]^2}, \tag{2.73}$$

where $\hat{E}_J^{(\pm)}(t)$ are quantized electric field operators, and $\tilde{N}$, $\tilde{M}$ are the N and M moments associated with the local modes of the bus channel, i.e. tracing over the phantom channels. In Fig. 2.8 we show these calculated correlations as a function of finesse for a ring with escape efficiency of $\eta = 0.75$ and a Gaussian pump pulse of duration 70 ps and energy 100 pJ. The local modes and the Lorentzian approximation give compatible results.

Finally, we calculate the squeezing by using Eq. (2.40), where the N and M moments for the local modes are intended as related to the bus waveguide. The maximum and minimum of Eq. (2.40) give the antisqueezing and squeezing, respectively. We show these in Fig. 2.9 for a ring with finesse $F = 780$ and escape efficiency $\eta = 0.75$, proving excellent agreement with the Lorentzian predictions in the appropriate limits.

In summary, the local-mode construction of the asymptotic fields offers a powerful framework that complements both perturbative asymptotic treatments and phenomenological Lorentzian-mode approaches. In practical applications, the choice between the three should be guided by the available computational resources and by the target operation regime. While perturbative methods provide analytically tractable solutions in low-gain regimes for any device geometry, and Lorentzian-mode approaches efficiently treat high-finesse resonators even at high pump powers, the asymptotic local-mode method extends the scope of nonperturbative quantum calculations to more general integrated photonic devices. This approach retains computational tractability and

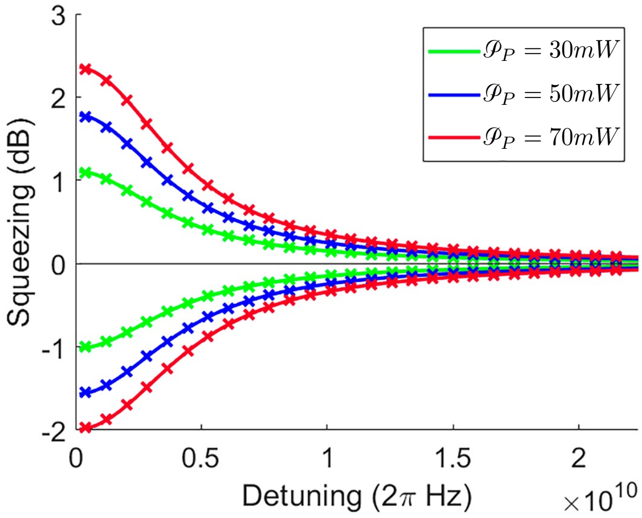

Figure 2.9: Squeezing spectrum calculations for different pump powers in the high-finesse nonperturbative regime. Image taken from [76].

unlocks the ability to model complex geometries and strong coupling regimes that lie beyond the reach of traditional methods.

2.5 Conclusion

In this chapter, we presented a theoretical framework for modeling spontaneous four-wave mixing in photonic integrated circuits, focusing on its application to the generation of squeezed light. We first reviewed the properties of squeezed states, highlighting their relevance for quantum technologies. This discussion lays the groundwork for Chapter 3, where we will design a resonant interferometric coupler for squeezed light generation.

We then introduced three complementary methods for calculating the generation rates and spectral correlations produced by a nonlinear interaction: the Lorentzian model, the asymptotic-fields formalism, and the local-modes approach. The Lorentzian model, discussed in Section 2.2, provides an accurate description of parametric processes in high-quality ring resonators, where the resonances are well-isolated and can be approximated as ideal Lorentzians. This approach is particularly useful for understanding squeezed light in the high-gain regime, as we will explore in Section 3.4.

The asymptotic-fields formalism, presented in Section 2.3, offers a more general framework for describing parametric interactions in complex device geometries, even when resonances are split or noisy. This method is well-suited for analyzing the photon-pair generation in the low-gain regime, as we will do in Section 3.3. Additionally, as we will show in the final part of this thesis, the asymptotic fields can be adapted to describe non-radiative modes, such as bound states in the continuum (Chapter 5), and non-parametric processes, such as single-photon emission (Chapter 6).

Finally, the local-modes approach, developed in Section 2.4, extends the asymptotic-fields formalism into the high-gain regime, enabling non-perturbative calculations for a broad class of integrated devices. This method bridges the gap between the Lorentzian and asymptotic-fields approaches, providing a robust tool for modeling spontaneous four-wave mixing in realistic scenarios.

Chapter 3

Squeezed Light from a Resonant Interferometric Coupler

After having examined the theoretical formalism to describe spontaneous four-wave mixing, we now turn our attention to two specific applications: the heralding of pure single-photons, and the generation of single-mode strongly squeezed states.

First, we analyze the challenges in implementing these applications, highlighting a common denominator in spite of their different characteristics. To address these challenges, we present a resonant interferometric coupler (RIC) combining multiple ring resonators coupled through a Mach-Zehnder Interferometer. We show that the RIC offers selective control over individual ring resonances. Subsequently, we report the application of this device to the generation of uncorrelated photon pairs with reduced spectral correlations, which is crucial for heralding pure single-photon states. Finally, we explore the possible use of the RIC for enhancing squeezed state generation.

3.1 Limits to Squeezing

3.1.1 Low-Gain Regime

Single-photons are essential for quantum computation [78] and quantum communication [79], where high purity is required to achieve optimal interference visibility, critical to many protocols. While quantum dots can produce near-unity purity single photons, they require demanding fabrication processes and cryogenic operation [80], motivating the development of room-temperature integrated sources.

To this end, one possible approach is to start from low-gain squeezed states produced through parametric processes such as parametric down-conversion [81] and SFWM. The low-gain requirement is essential to have a negligible probability of multipair generation, so that the squeezed state can be approximated as the sum of a vacuum state and a two-photon state, as in Eq. (2.55).

Equivalently, one can think of it as a photon pair that is generated only with a certain probability $|\beta|^2$, with $|\beta|^2 \ll 1$ the average number of signal-idler pairs per pump pulse. Subsequently, if the pair is present, one photon is detected and acts as a herald for the second photon, which is then projected into a single-photon state.

The generation of uncorrelated photon pairs via SFWM in integrated resonators faces a fundamental challenge arising from the spectral-temporal correlations between signal and idler photons. The extent of these correlations depends on the relative linewidths of pump, signal, and idler. If the pump is much narrower than the signal and idler resonances, which can be obtained, for instance, by using a continuous-wave laser, the biphoton wavefunction will be approximately antidiagonal in the signal-idler frequency space, and the correlations will be very strong. Even when using a spectrally broad pulsed laser as the pump, the presence of identical ring resonances at the pump, signal, and idler modes will introduce correlations, limiting the spectral purity of heralded single photons generated in a ring resonator to approximately 91.7% [82].

A possible approach is spectral filtering to reduce the effective width of some resonances, but at the expense of reducing the effective heralding efficiency [83] Alternatives in $\chi^{(3)}$ platforms include pump manipulation techniques that use temporally structured pump pulses [75] or dual-pump configurations [84], though these require more complex experimental setups. Recent demonstrations have shown that resonator architectures beyond the simple ring can overcome these limitations. Photonic molecule approaches using coupled resonators have achieved purities exceeding 99% with high heralding efficiency [85]. Similarly, interferometric coupling schemes have demonstrated the ability to generate truly unentangled photon pairs without spectral filtering [74, 86], highlighting the power of resonance engineering approaches.

3.1.2 High-Gain Regime

The second application is the generation of strongly squeezed states in the high-gain regime, which are crucial resources for continuous-variable quantum computing protocols such as Gaussian boson sampling [87, 60]. These applications require single-mode squeezed vacuum states with high squeezing levels to achieve quantum computational advantage in fault-tolerant architectures. Even in this case, efficient correlations can be achieved only when the involved photons have high indistinguishability. In the frequency degree of freedom, this is only possible when light is generated in a dual-pump scheme.

The generation of strongly squeezed states through dual-pump SFWM faces a different but equally challenging set of limitations compared to the single-pump one. In the high-gain regime required for significant squeezing, parasitic nonlinear processes become prominent and can severely degrade the achievable squeezing level [88]. These parasitic processes, including single-pump SFWM and Bragg-scattering four-wave mixing, introduce excess noise into the squeezed mode and limit the maximum achievable squeezing, as illustrated in

Fig. 3.1.

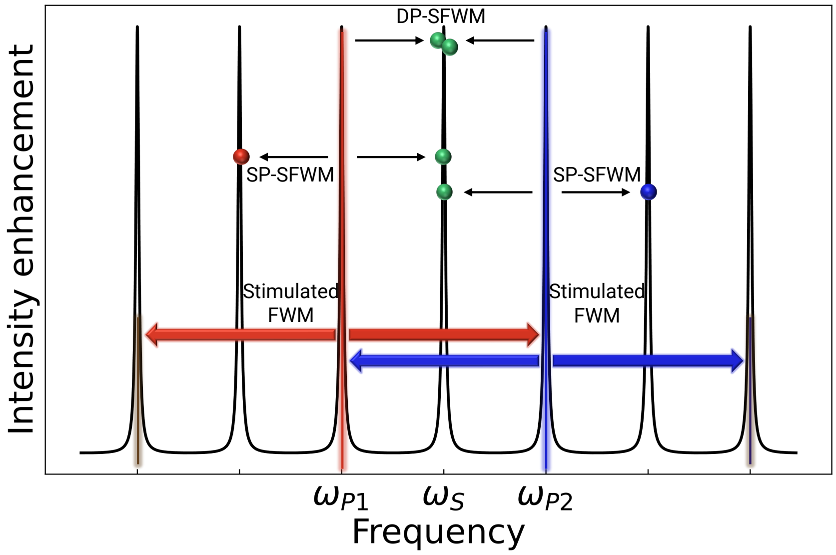

Figure 3.1: Parasitic nonlinear processes in high-gain dual-pump SFWM that limit squeezed state generation. The ring resonator frequency comb supports the desired dual-pump process (indicated by the two input beams) as well as various parasitic interactions that introduce excess noise. These include single-pump SFWM from each pump individually, Bragg scattering to adjacent resonances, and higher-order nonlinear interactions that degrade the purity of the generated squeezed state.

The challenge is particularly acute in integrated platforms, where the high optical intensities required for strong squeezing can simultaneously excite multiple nonlinear processes. Unlike the low-gain regime, where parasitic effects can often be neglected and a pump optimization is usually sufficient to obtain high squeezing level in a simple resonator [89, 90], high-gain operation requires careful management of the entire nonlinear spectrum to achieve optimal performance.

Several strategies have been developed to suppress these parasitic effects. One approach entails linearly uncoupled resonators, where careful design of the coupling conditions can reduce parasitic processes while maintaining the desired dual-pump interaction [91]. However, this approach often requires reduced interaction lengths, limiting the achievable squeezing levels.

Pump detuning techniques can also mitigate parasitic effects by shifting the pump frequencies away from perfect resonance [51], but this approach necessarily reduces the field enhancement and thus the achievable squeezing for a given pump power.

More sophisticated approaches involve resonance splitting through structural modifications of the resonator, such as corrugated photonic crystal rings that selectively suppress unwanted resonances [92] or photonic molecules with asymmetric coupling [54], though these approaches typically offer limited reconfigurability once fabricated.

3.1.3 A Possible Solution

Whether the goal is to eliminate spectral correlations in photon pair generation or to suppress parasitic processes in squeezing generation, the ability to independently tune the quality factors and coupling conditions of specific resonances emerges as a key requirement in quantum technology.

Various resonance tuning mechanisms have been demonstrated in integrated platforms. Optical force-based approaches can provide dynamic control over coupling strengths [93], while stimulated Raman processes offer wavelength-selective tuning capabilities [94]. Electro-optic approaches using carrier injection or depletion can modulate individual resonator properties [95], and interferometric coupling schemes provide both static and dynamic control over resonance characteristics [96, 97, 98].

The recent success of complex architectures such as the photonic molecule [85] demonstrates that sophisticated resonance control can simultaneously address multiple constraints, achieving high purity, high efficiency, and good brightness in a single device. This opens the potential for more general resonance tuning approaches that can be dynamically reconfigured for different applications.

In the following sections, we will present a resonant interferometric coupler that enables selective and tunable control over the quality factors of individual resonances in a ring resonator system. Then, we will study how this structure can be used to address the problems of correlations and the parasitic noise in squeezed state generation.

3.2 The Resonant Interferometric Coupler

The basic interferometric coupler, shown in Fig. 3.2(a), consists of a main ring resonator of radius R that is coupled to a bus waveguide at two distinct points, A and B, with coupling coefficients κ_A and κ_B, respectively. The region between these two coupling points can be viewed as an asymmetric Mach-Zehnder, where one arm travels a distance πR along the ring, while the other arm travels a distance L along the bus waveguide. [97, 96, 98]

Light propagating from A to B can either travel along the bus waveguide (direct path of length L) or couple into the ring, propagate halfway around it, and couple back to the bus (ring path of length πR). The relative phase difference between these two paths determines the constructive or destructive interference at point B, directly controlling the effective coupling strength between the ring and the bus waveguide. The frequency-domain transmission of

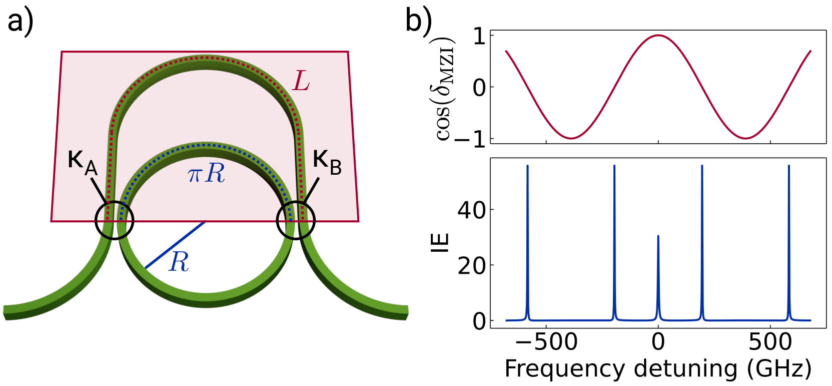

Figure 3.2: Schematic and spectral response of a basic interferometric coupler. a) A main ring resonator of radius R is coupled to a bus waveguide at two points with coupling coefficients κ and self-coupling coefficients σ, creating an embedded Mach-Zehnder interferometer structure. The MZI arms have different lengths: πR along the ring and L along the bus waveguide. b) (top) the cosine of the MZI dephasing $\cos(\delta_{\text{MZI}})$ and (bottom) the intensity enhancement (IE) of the ring resonances. The periodic nature of the MZI response creates alternating high and low enhancement across different resonances, demonstrating the non-selective nature of basic interferometric coupling.

this structure can be expressed as [99],

$$T = \left| \frac{e^{i\tilde{\phi}_{\text{Main}}} \left(\sigma_A \sigma_B e^{i\delta_{\text{MZI}}} - \kappa_A \kappa_B - e^{i\delta_{\text{MZI}}} e^{i2\tilde{\phi}_{\text{Main}}} \right)}{1 - \left(\sigma_A \sigma_B - \kappa_A \kappa_B e^{i\delta_{\text{MZI}}} \right) e^{i2\tilde{\phi}_{\text{Main}}}} \right|^2 , \tag{3.1}$$

where $\tilde{\phi}_{\text{Main}} = k\pi R + \Delta\phi_{\text{Main}}$ is the accumulated phase in the ring, $\sigma_j = \sqrt{1-\kappa_j^2}$ are the self-coupling coefficients, $k = \omega n_{\text{eff}}/c$ is the propagation constant, $\delta_{\text{MZI}} = k(L - \pi R) + \Delta\phi_{\text{MZI}}$ represents the phase imbalance between the MZI arms, and $\Delta\phi_{\text{Main}}$ and $\Delta\phi_{\text{MZI}}$ are the dephasings added by any external factor (e.g. temperature or defects) to the ring and to the MZI respectively.

When $L = 3\pi R$, the phase difference becomes $\delta_{\text{MZI}} = 2\pi kR + \Delta\phi_{\text{MZI}}$, which assumes identical values for all the ring resonances. This ensures that all resonances experience the same effective coupling, creating a periodic response across the entire ring spectrum. From Eq. (3.1), we can define an effective coupling coefficient between the ring and the bus waveguide as

$$|\kappa_{\text{eff}}|^2 = |\kappa_A \sigma_B + \kappa_B \sigma_A e^{i\delta_{\text{MZI}}}|^2, \tag{3.2}$$

which governs the loaded quality factor and intensity enhancement of the ring resonances. When the coupling coefficients are matched ($\kappa_A = \kappa_B = \kappa$), the effective coupling can reach its maximum value,

$$|\kappa_{\text{eff}}|^2_{\text{max}} = 4\kappa^2\sigma^2 = 4\kappa^2(1-\kappa^2), \tag{3.3}$$

corresponding to an overcoupled ring resonator with enhanced extraction efficiency. In this situation, a π dephasing in the phase δ_{MZI} would completely uncouple the ring.

In Fig. 3.2(b), we show a typical spectral response of the interferometric coupler with $L = \frac{3}{4}\pi R$, $\Delta\phi_{\mathrm{MZI}}$, and $\kappa_A^2 = \kappa_B^2 = 0.03$. The cosine of the MZI phase difference $\cos(\delta_{\mathrm{MZI}})$ varies sinusoidally across the frequency range, with the period determined by the free spectral range of the interferometer. This periodic modulation directly affects the intensity enhancement of the ring resonances, creating a pattern where some resonances experience high enhancement while others are suppressed.

While the basic interferometric coupler provides valuable control over ring resonance properties, it suffers from limited wavelength selectivity: any phase modulation applied through $\Delta\phi_{\mathrm{wg}}$ affects all ring resonances simultaneously due to the periodic nature of the MZI response. This becomes problematic when specific resonances need to be independently controlled, as required for parasitic process suppression in squeezed light generation or for creating spectrally uncorrelated photon pairs.

To overcome the inherent limitations of basic interferometric coupling, we introduce an auxiliary ring resonator (Aux) into the MZI structure, creating what we term a *Mach-Zehnder Resonant Interferometric Coupler* (MZ-RIC) [99]. This architecture, shown in Fig. 3.3, adds a wavelength-selective phase control that enables independent manipulation of individual ring resonances. To distinguish between the two resonators in the MZ-RIC, we name the original main resonator *Main*.

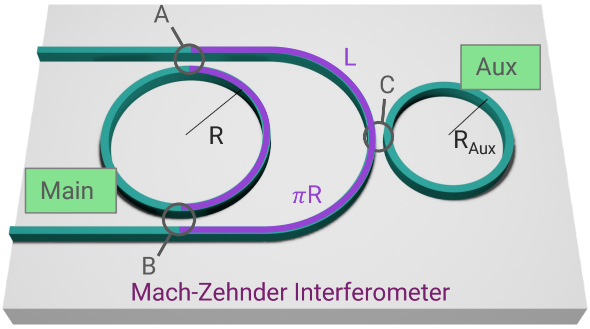

Figure 3.3: Schematic of the MZ-RIC. The basic interferometric coupler is enhanced with an auxiliary ring resonator of radius R_{Aux} coupled to the bus waveguide with coupling coefficient κ_C. This auxiliary resonator provides wavelength-selective phase modulation that enables independent control of individual Main ring resonances while leaving neighbouring resonances largely unaffected. Image adapted from [99].

The Aux resonator introduces a frequency-dependent modification to Eq. (3.1) through its transmission coefficient

$$t_{\text{Aux}} = \frac{\sigma_C - e^{i\tilde{\phi}_{\text{Aux}}}}{1 - \sigma_C e^{i\tilde{\phi}_{\text{Aux}}}}, \tag{3.4}$$

where $\sigma_C = \sqrt{1 - \kappa_C^2}$ is the self-coupling coefficient of the Aux resonator, $\tilde{\phi}_{\text{Aux}} = k\pi R + \Delta\phi_{\text{Aux}}$ is its accumulated phase, and $\Delta\phi_{\text{Aux}}$ the external dephasing. The resulting transmission of the device can be obtained by substituting $e^{i\delta_{\text{MZI}}}$ in Eq. (3.1) with

$$e^{i\tilde{\delta}_{\text{MZI}}} = \frac{\sigma_C - e^{i\tilde{\phi}_{\text{Aux}}}}{1 - \sigma_C e^{i\tilde{\phi}_{\text{Aux}}}} e^{i\delta_{\text{MZI}}}. \tag{3.5}$$

In practice, the MZI phase balance is modified by the transmission coefficient of the Aux resonator. When the Aux resonator is far from any resonance, it acts as a transparent element with minimal phase shift. However, when tuned to coincide with a specific Main ring resonance, it imparts a sharp phase transition that can dramatically alter the interference condition for that particular frequency while leaving other resonances unaffected. The key advantage of this architecture lies in the resonant nature of the Aux ring's phase response. The transmission coefficient of the Aux resonator exhibits a rapid phase change of approximately 2π when tuned through a resonance, effectively providing a wavelength-selective switch that can alter the MZI interference condition for specific frequencies.

Fig. 3.4 demonstrates this selective control capability. In Fig. 3.4(a), the MZI length is set to $L = 3\pi R$ to bring all the resonances to the maximal overcoupling and the Auxiliary resonator is detuned from all the Main resonances, as can be seen by the transmission spectrum. Corresponding to the Aux resonances, the otherwise smooth MZI response features a sharp phase discontinuity. When an Aux resonance is aligned with a target Main ring resonance (for instance through the use of a micro-heater), as it happens in Fig. 3.4(b), the phase jump can shift the interference from constructive to destructive, dramatically changing the effective coupling and resulting intensity enhancement for that specific resonance while neighbouring resonances remain largely unperturbed. Intermediate conditions can be achieved by partially detuning either the Aux or the MZI, as shown in Fig. 3.4(c-d), where the target resonance is first brought to critical coupling in an overcoupled comb of Main resonances and then the reverse condition is achieved by shifting both the MZI and Aux phases.

This selective control mechanism enables several applications needing quality factor tuning or intensity enhancement control with high resonance selectivity or dynamic tuning [94, 93, 100, 95]. Multiple auxiliary rings can be integrated along the extended bus waveguide, allowing independent control of different Main ring resonances with minimal crosstalk. The design flexibility of the MZ-RIC also extends to the choice of the Aux ring radius. By

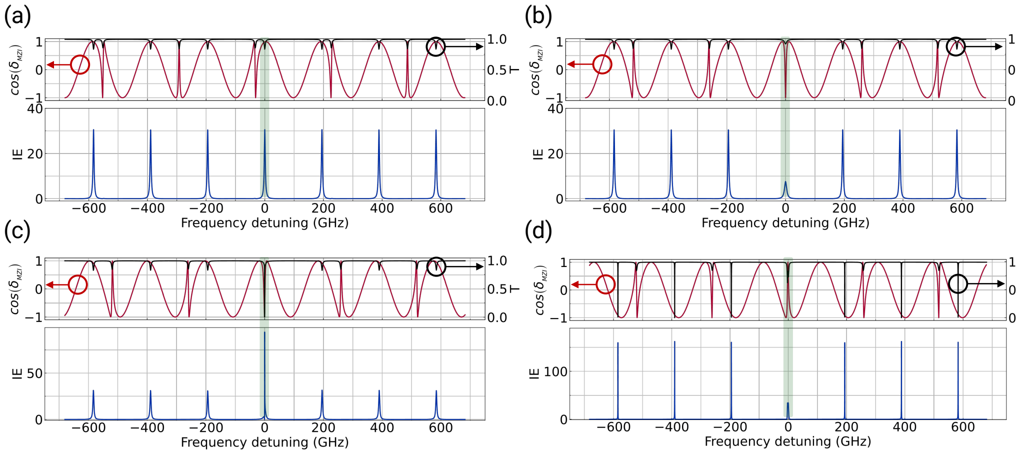

Figure 3.4: Selective resonance control using the resonant interferometric coupler with $\kappa_A = \kappa_B = 0.03$, $\kappa_C = 0.1$, $R = 120$ µm, $R_{\text{Aux}} = \frac{3}{4}R$, and $\alpha = 0.1$ dB/cm. The cosine of the dephasing and transmission are shown in the top panel, while the intensity enhancement appears in the bottom panel. All the spectra are shown as a function of the detuning from a target central resonance (highlighted in green). (a) The Aux resonator is detuned from all the Main resonances, with $\Delta_{\text{MZI}} = 2m\pi$, setting all the resonances in overcoupling. (b) The Aux resonator is tuned to the central resonance from all the Main resonances, with $\Delta_{\text{MZI}} = 2m\pi$. (c-d) Both the Aux resonator and the MZI are detuned to produce (c) a target critically-coupled resonance in a comb of overcoupled resonances and (d) a target overcoupled resonance in a comb of critically-coupled resonances. Image adapted from [99].

selecting $R_{\text{Aux}} = \frac{3}{4}R$, only one Main ring resonance out of every four aligns with an Aux resonance, providing clear spectral separation for selective control. Alternatively, incommensurate ratios can be chosen to eliminate any periodic interference patterns, enabling truly independent addressing of arbitrary resonances. We show this in Fig. 3.5, where the same parameters and dephasings of Fig. 3.4(c) are applied to a MZ-RIC with an Aux resonator of radius $R_{\text{Aux}} = \frac{\pi}{4}R$.

3.2.1 Experimental Demonstration

The MZ-RIC was validated experimentally by our collaborators. These demonstrations confirm the device's capability to selectively modify individual resonance characteristics while preserving the quality factors of neighbouring modes.

The device was fabricated on a silicon nitride photonic platform [101]. The Main resonator features a radius of $R = 120$ µm, while the Aux resonator has a radius of $R_{\text{Aux}} = 90$ µm, establishing the 4/3 ratio that ensures spectral alignment between Main and Aux resonances with a periodic pattern. The coupling coefficients between the Main ring and the bus waveguide at points

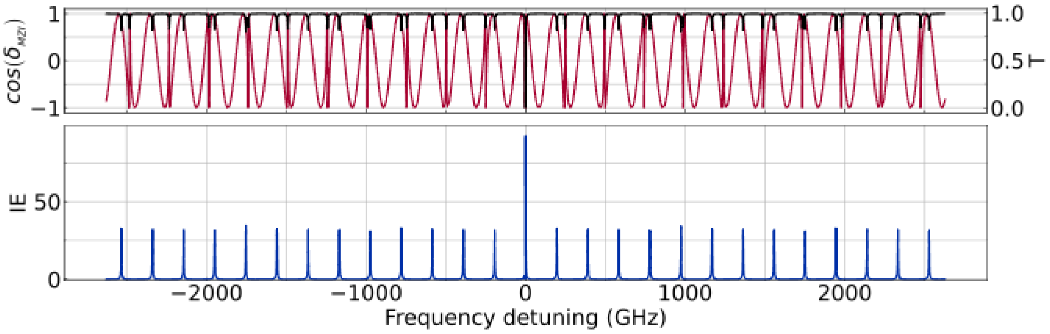

Figure 3.5: Selective resonance control using the resonant interferometric coupler with $\kappa_A = \kappa_B = 0.03$, $\kappa_C = 0.1$, $R = 120$ µm, $R_{\text{Aux}} = \frac{\pi}{4}R$, and $\alpha = 0.1$ dB/cm and dephasings set as in Fig. 3.4(c). The cosine of the dephasing and transmission are shown in the top panel, while the intensity enhancement appears in the bottom panel. Image adapted from [99].

A and B are $\kappa_A^2 = \kappa_B^2 = 0.03$, while the Aux resonator couples to the bus with $\kappa_C^2 = 0.21$, placing it in the overcoupled regime for enhanced phase control.

The waveguides have a cross-section of 1.75 μm width and 800 nm thickness, with a coupling gap of 0.4 μm between the Main resonator and the bus waveguide. The intrinsic quality factor of the Main resonator is $Q_I \approx 3.2 \times 10^6$, corresponding to propagation losses of approximately 0.1 dB/cm. The Main and Aux resonators have free spectral ranges of 1.56 nm and 2.1 nm, respectively, confirming the designed 4/3 ratio.

The experimental setup used for the characterization is shown in Fig. 3.6 [99]. A tunable continuous-wave laser provided the input signal, with polarization controlled via a fibre polarization controller to match the TE mode of the silicon nitride waveguides. Light coupling was achieved through an array of UHNA4 fibres, introducing approximately 1.7 dB coupling loss per facet. Three thermo-optic phase shifters enabled precise control over the device parameters, enabling the independent modulation of the Main ring, bus arm, and Aux resonator. The device was mounted on a thermally stabilized platform, with metallic micro-heaters controlled by voltage driver modules to ensure stable operation. The transmission measurements were performed by detecting the output light through a power meter while continuously scanning the input wavelength.

In Fig. 3.7(a) are shown the position and normalized transmission of a target Main resonance at $\lambda_0 = 1543$ nm while sweeping the Aux resonator across it [99]. The Aux resonance was detuned over a range from $\Delta\lambda_{\text{Aux}}/\gamma_{\text{Aux}} = 5$ to $\Delta\lambda_{\text{Aux}}/\gamma_{\text{Aux}} \approx -2$, where $\gamma_{\text{Aux}} = 0.067$ nm represents the Aux resonance linewidth. The theoretical prediction of same quantity is plotted in Fig. 3.7(b), showing good agreemet. The effective coupling coefficient is also shown in the inset of Fig. 3.7(b). Additionally, in Fig. 3.7(c), it is shown the extintion (i.e. the minimum transmission) and the loaded quality factor $Q_L = \lambda/\Delta\lambda$ where λ is the resonance linewidth and $\Delta\lambda$ the extinction depth [99]. By combining

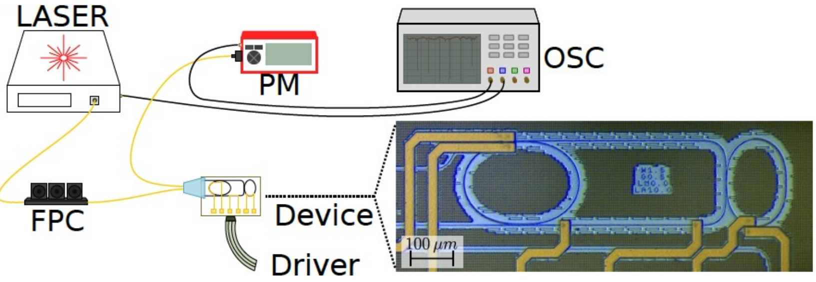

Figure 3.6: Experimental setup for measuring the transmission of a MZ-RIC. Image taken from [99].

all these quantities, it is possible to identify all the relevant coupling regimes.

The experimental results demonstrate remarkable control over the effective coupling coefficient. When $\Delta\lambda_{\text{Aux}}/\gamma_{\text{Aux}} \sim 2.5$, the target resonance enters the undercoupled regime with near-zero extinction, and the loaded quality factor approaches the intrinsic limit of $\sim 3 \times 10^6$. As the Aux resonance approaches alignment, critical coupling is achieved at $\Delta\lambda_{\text{Aux}}/\gamma_{\text{Aux}} \sim 1.2$, where extinction maximizes to approximately -10 dB and the loaded quality factor equals half the intrinsic value, confirming $\kappa_{\text{eff}} = \kappa_{\text{cc}}$, which is the critical coupling calculated from the measured intrinsic losses. When the Aux resonance aligns with the target mode ($\Delta\lambda_{\text{Aux}}/\gamma_{\text{Aux}} \to 0$), the system transitions to the overcoupled regime. Here, the loaded quality factor reaches its minimum value of 6.5×10^4 with extinction reduced to -0.25 dB, indicating maximum effective coupling. This continuous tuning capability spans nearly two orders of magnitude in quality factor, from 6.5×10^4 to 3×10^6. Overall, the effective coupling coefficient varies by more than an order of magnitude.

Resonance selectivity is demonstrated in Fig. 3.7(d), where the quality factors of six Main ring resonances are tracked while moving the Aux resonance. All the quality factors are normalized to their mean value. Only the resonance at 1549.30 nm shows a significant modulation, which is compatible to that of the target. This is because the two are spaced by four free spectral ranges. All the other resonances remain scarcely affected by the presence of the Aux ring [99].

A second practical advantage of the resonant interferometric coupler lies in its reduced power consumption compared to conventional interferometric approaches [99]. The power required to sweep the loaded quality factor from 10% to 90% of its is roughly $\frac{1}{3}$ when modulating the heater of the Aux resonator versus a direct phase control of the interferometer, as is clear from Fig. 3.8. This power efficiency translates directly to reduced thermal crosstalk between neighbouring components, a critical consideration for large-scale integrated photonic circuits where multiple devices must operate simultaneously without mutual interference.

In the following, we will discuss two applications of the MZ-RIC in quantum photonics, where selective resonance control proves essential for generating

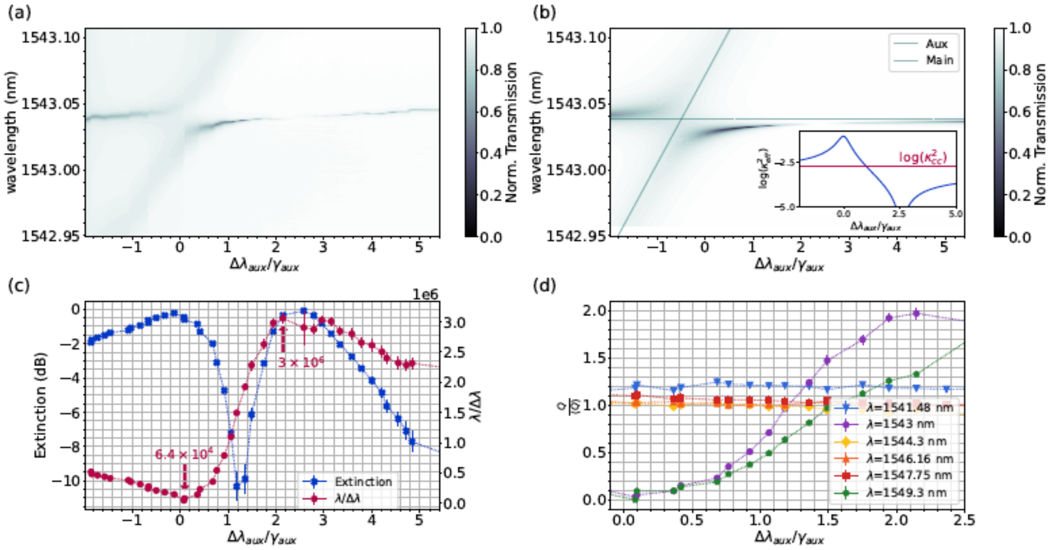

Figure 3.7: Experimental demonstration of the tunability and selectivity in a MZ-RIC. (a) Transmission of one Main resonance in the range 1523.95 − 1543.10 nm as the closest Aux resonance position is swiped across 7 Aux linewidths. (b) Theoretical simulation of the same transmission spectra. The Main and Aux positions are indicated by the two solid lines. In the inset is shown the logarithm of the effective MZ-RIC coupling coefficient, with the red line indicating critical coupling. (c) Extinction and effective quality factor of the same Main resonance. (d) Quality factors (normalized to their average value) of six Main resonances, as two Aux resonator resonances are swept around 1543.00 nm and 1549.30nm. All the other Main resonances shown in the figure do not overlap with any of the Aux ones.

uncorrelated photon pairs and suppressing parasitic processes in squeezed light generation.

3.3 Unentangled Photon Pair Generation

Having established the resonant interferometric coupler's selective tunability capabilities, we now address its applications in Quantum Photonics. An interesting experiment done with our architecture addresses one of the central challenges in heralded single-photon sources development: achieving high spectral purity in photon pairs generated through SFWM [101]. This experiment directly tackles the correlation issues detailed in Section 3.1, demonstrating how selective quality factor control enables the generation of nearly uncorrelated photon pairs that surpass the theoretical limits of conventional single-ring configurations.

The experimental characterization employed time-resolved coincidence detection to retrieve the joint temporal intensity of photon pairs generated by

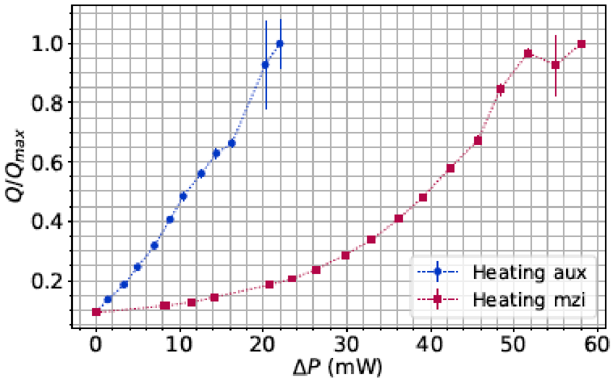

Figure 3.8: Quality factor of one Main resonance as a function of the applied heating power. The same quality factor variation is obtained by acting on two different modulators: the Aux heater and the MZI heater. The first approach consumes approximately $\frac{1}{3}$ of the power. Image taken from [99].

SFWM in the same silicon nitride resonator used for the experiments probing the linear properties of the MZ-RIC [101]. The pump signal was modulated using an electro-optic amplitude modulator to create rectangular pulses with a duration $T = 300$ ps and a repetition rate of 10 MHz. This pulsed operation enabled precise temporal discrimination between photon pairs generated in the resonator versus those produced in the bus waveguide. As shown in Fig. 3.9, the generated signal-idler pairs were separated from the pump using an off-chip notch filter and subsequently demultiplexed to two independent superconducting nanowire single-photon detectors (SNSPDs). The detector outputs were connected to a time-tagging unit with timing jitter of approximately 35 ps, synchronized with the electrical trigger of the pump pulse to record the arrival times of both photons relative to the pump trigger.

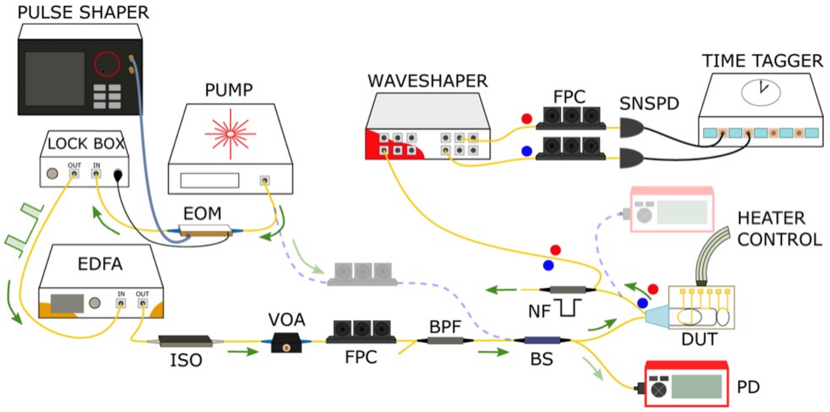

Figure 3.9: Experimental setup for measuring the temporal correlations of the photon pairs generated in the MZ-RIC. Image taken from [101].

The choice of time-resolved and not of frequancy-resolved characterization was motivated by the narrow bandwidth of the Main ring resonances. This configuration allowed reconstruction of the joint temporal intensity $\mathrm{JTI}(t_s, t_i)$, describing the joint probability of detecting a signal photon at time t_s and an idler photon at time t_i within a two-dimensional temporal histogram with 60 ps resolution. This quantity represents the Fourier transform of the more common joint spectral intensity, which is the square modulus of the biphoton wavefunction introduced in Chapter 2. The temporal resolved measurements allowed also to correctly identify the photon pairs that are generated within the resonator, as their arrival time was clearly separated from the arrival time of the photons produced in the waveguide. This temporal separation arose because the pump photon lifetime in the resonator $\tau_L \sim 820$ ps exceeded the pump pulse duration $\tau_P = 300$ ps.

In Fig. 3.10 are shown the resonator's transmission and JTI for three different configurations of the MZ-RIC. In the first configuration, Fig. 3.10(a), the device operated as a conventional single-ring resonator by positioning all Aux resonances far from the Main resonances to minimize perturbation. The pump, signal, and idler were aligned to resonances separated by four free spectral ranges, ensuring identical quality factors of $Q = 8 \times 10^5$ for all three modes due to the periodic nature of the interferometric coupler with the chosen 4/3 radius ratio between Main and Aux resonators. The reconstructed JTI for this single-ring-like operation exhibited the characteristic temporal correlations expected from equal quality factor resonances [101]. From the measured JTI, a heralded single-photon purity upper bound of $P = 0.9289 \pm 0.0002$ was extracted, corresponding to a Schmidt number of $K = 1.0765 \pm 0.0004$. This value approached the theoretical maximum of $P = 0.93$ achievable for resonators with equal quality factors and Gaussian pump pulses, confirming the measurement accuracy and resonator's quality.

The second configuration, Fig. 3.10(b), by positioning an Aux resonance close to the pump mode, the pump quality factor was reduced to $Q_P = 3.3 \times 10^5$ while the signal and idler resonances maintained higher quality factors of $Q_S = 7.6 \times 10^5$ and $Q_I = 1.1 \times 10^6$, respectively. This asymmetric configuration created the condition $\min(Q_S, Q_I)/Q_P \sim 2.3 > 1$, enabling the generation of photon pairs with purity beyond the conventional limit. The resulting JTI exhibited dramatically suppressed temporal correlations, appearing nearly separable in the signal-idler time domain [101]. From this measurement, a high purity of $P = 0.9867 \pm 0.0001$ with a Schmidt number of $K = 1.0134 \pm 0.0002$ were deduced, well beyond the single-ring limit. This result represents one of the highest purities reported for integrated resonator-based sources and demonstrates the clear advantage of selective quality factor engineering over conventional approaches. This approach aligns with theoretical predictions by Vernon *et al.* [74] showing that broader pump modes can reduce spectral correlations and enable truly unentangled photon pairs without spectral filtering.

In the third configuration, Fig. 3.10(c), the opposite regime is explored,

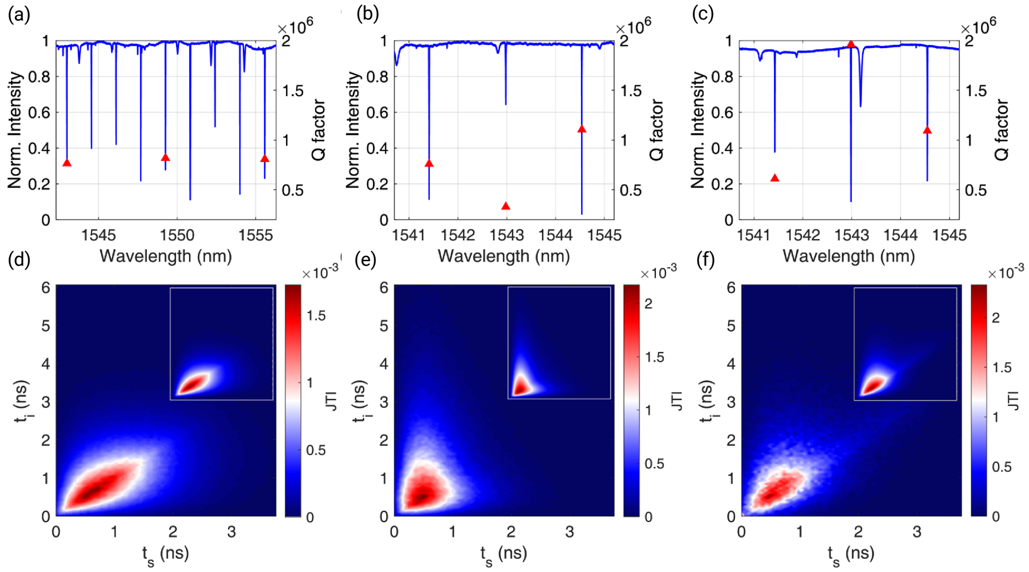

Figure 3.10: (a-b-c) Transmission (blue solid line) of the structure for three different configurations. The red triangles indicate the quality factor of the three resonances chosen for the SP-SFWM experiment. (d-e-f) Measured JTI of the generated pairs. The inset shows the simulated JTI. (a-d) First configuration: the pump, signal, and idler are enhanced by three identical resonances. This simulates a simple ring resonator. (b-e) The pump resonance has a lower quality factor compared to the others, reducing the correlations in the generated pair. (c-f) The pump resonance has a higher quality factor compared to the others, slightly enhancing the correlations in the generated pair. Image adapted from [101].

with a narrowed pump resonance, enhancing the Schmidt number to $K = 1.20$ and reducing the purity to $P = 0.829$. While this regime could benefit entangled photon-pair generation, experimental constraints related to the pump and detectors limited here the useful entanglement.

3.4 Enhanced Squeezed Light Generation with noise suppression

Moving from the low-gain regime to high-power operation, we now explore how the MZ-RIC addresses the challenge of parasitic processes that fundamentally limit squeezed light generation in dual-pump SFWM [102].

The transition to high-gain operation necessitates a fundamentally different device configuration optimized for field enhancement suppression rather than quality factor modulation [102]. We increase the Main ring coupling coefficients to $\kappa_A = 0.6$ and $\kappa_B = 0.48$, with the phase of the interferometer set to $\Delta\phi_{\mathrm{MZI}} = \pi$. This asymmetric coupling strategy enables the device to achieve efficient extraction at the desired signal resonance while simultaneously suppressing parasitic processes at unwanted sideband resonances. The intensity enhancement and transmission, along with the MZI dephasing, are shown in Fig. 3.11(a), where the Aux ring was artificially decoupled from the structure to simulate a conventional single-ring resonator. Our chosen parameters yield a minimum effective coupling that maintains the Main ring in the overcoupled regime with 90% extraction efficiency and approximately 20 dB resonant intensity enhancement relative to the input power [102].

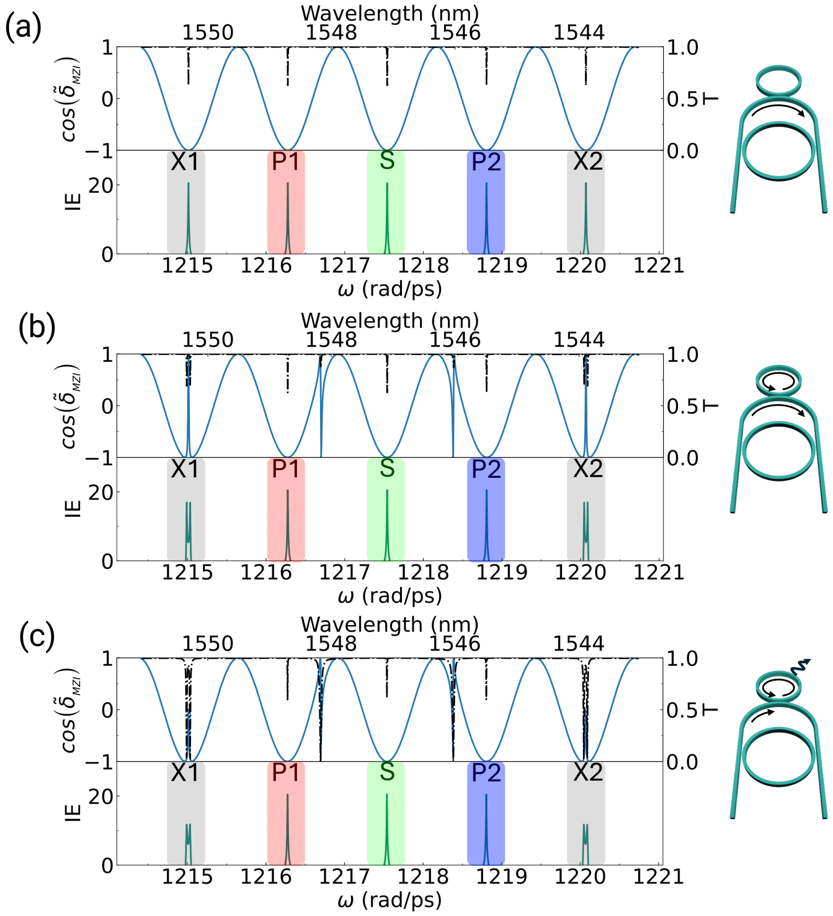

Figure 3.11: Dephasing and transmission (top panel), and intensity enhancement (bottom panel) when (a) the Aux resonator is completely uncoupled, (b) the Aux resonator is overcoupled, and (c) the Aux resonator is critically-coupled. Image taken from [102].

We add the Aux resonator and choose it to operate with a much higher coupling coefficient of $\kappa_C = 0.4$. The 4/3 radius ratio between Main and Aux resonators ensures that only one every fourth resonance of the Main ring experiences significant perturbation and suppression, preserving the pump and signal modes needed for dual-pump SFWM. When the Aux resonator is tuned such that its resonances align with the unwanted sideband modes X1 and X2, dramatic suppression occurs through two complementary mechanisms. First, the π phase shift introduced by the Aux resonator creates destructive interference within the interferometric structure, effectively driving the aligned resonances into extreme overcoupling. As shown in Fig. 3.11(b), this reduces their field enhancement by more than 14 dB while leaving the central pump and signal resonances virtually unaffected. Second, when the effective coupling reaches its maximum value, the Main and Aux resonators enter a strong coupling regime that induces resonance splitting. This splitting detunes the unwanted resonances away from wavelengths that satisfy energy conservation for parasitic SFWM processes, providing an additional suppression mechanism.

The analysis of loss tolerance reveals remarkable robustness of the suppression mechanism [102]. Even when the Aux resonator experiences artificially increased propagation losses of 3.3 dB/cm to reach critical coupling with the bus waveguide, the device maintains effective parasitic suppression, as shown in Fig. 3.11(c). In this configuration, the Aux ring acts as an interruption in the interferometric arm at each resonance, producing strongly frequency-dependent effective coupling while preserving the fundamental suppression characteristics. This tolerance to Aux resonator losses represents a significant practical advantage for device fabrication and operation.

3.4.1 Expected Squeezing

The squeezing performance is governed by the balance between dual-pump efficiency and parasitic noise suppression. This can be simulated by using the Lorentzian model method outlined in Chapter 2. One thing to consider when calculating the squeezing is that in this overcoupled regime, light is distributed in also in the bus waveguide Fig. 3.12, causing an approximately 20% larger effective mode volume compared to the sole Main ring. For the numerical analysis, we consider Gaussian pump pulses with 1.55 ns duration and 35 mW average power, generating squeezed light in the signal resonance at 1547.1 nm with pump resonances at 1548.7 nm and 1545.5 nm [103].

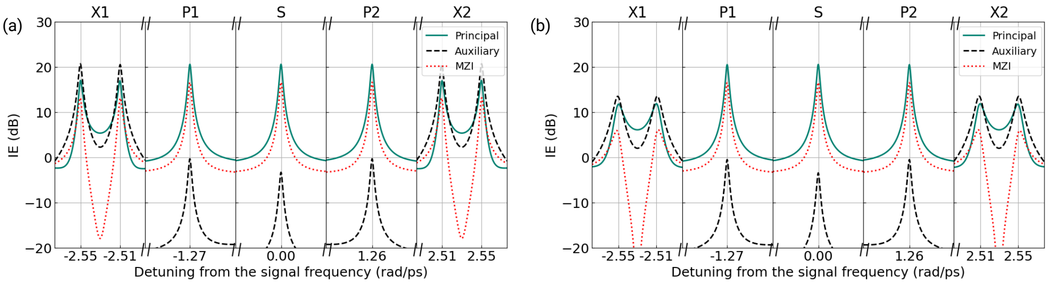

Figure 3.12: Intensity enhancement distribution in three parts of the MZ-RIC when the Aux ring is (a) detuned, (b) overcoupled, (c) critically coupled. Image taken from [102].

The calculated squeezing level is shown in Fig. 3.13 demonstrates a clear dependence on the Aux coupling coefficient κ_C. When $\kappa_C = 0$, corresponding to operation without the Aux resonator, the device behaves as a conventional single-ring resonator limited to -3.24 dB of squeezing due to unsuppressed parasitic processes.

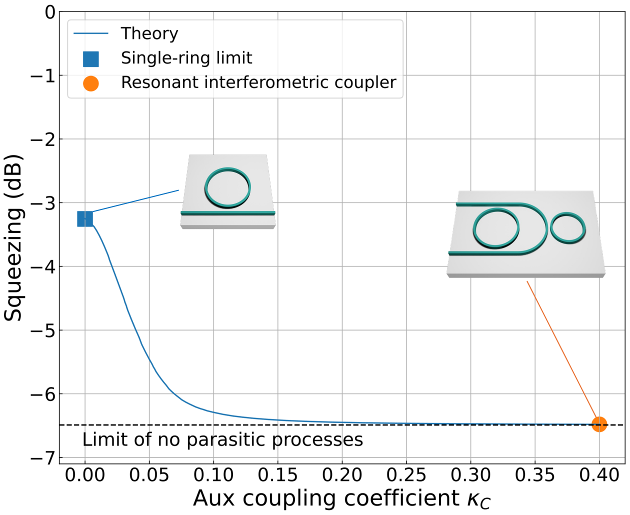

Figure 3.13: Calculated squeezing in the structure as a function of the Aux coupling coefficient κ_C. Image taken from [102].

As κ_C increases, the Aux resonator progressively suppresses unwanted resonances, leading to weaker single-pump processes and enhanced squeezing performance. At $\kappa_C = 0.4$, parasitic processes are almost entirely suppressed and the resonant interferometric coupler achieves -6.48 dB of squeezing, regardless of its intrinsic losses, approaching the theoretical maximum of -6.49 dB for the given pump power and propagation losses.

This represents a factor of two improvement over the single ring and approaches the performance records achieved with photonic molecules [54] while offering improved fabrication tolerance, post-fabrication tunability, reduced thermal crosstalk between the heater modulators, and the potential for scalable integration of multiple Aux resonators along the bus waveguide to address higher-order parasitic processes. These benefits position the resonant interferometric coupler as a highly attractive platform for practical squeezed light sources requiring both high performance and operational flexibility.

3.5 Conclusion

In this chapter, we addressed the challenges of generating high-purity quantum states of light in integrated photonic devices, focusing on two key applications: the heralding of pure single photons and the generation of strongly squeezed states. We first discussed the fundamental limitations imposed by spectral correlations in spontaneous four-wave mixing. These correlations reduce the purity of heralded single photons obtained from non-degenerate photon-pairs in the low-gain regime and introduce parasitic noise in degenerate high-gain squeezing. These challenges motivated the development of a novel architecture, the Mach-Zehnder resonant interferometric coupler, which combines ring resonators with a Mach-Zehnder interferometer to achieve selective control over individual resonances.

The structure leverages the interference between light propagating in a Main ring resonator and the bus waveguide coupled to it. The two are connected at two separate points, forming an effective Mach-Zehnder interferometer. An auxiliary ring resonator coupled to the bus waveguide provides a resonant phase shifts and enables tuning of the quality factors of specific resonances. This capability can be harnessed to suppress unwanted spectral correlations, as reported in Section 3.3, where our collaborators could measure an heralded single-photon purity up to 98.67%. The same architecture was then adapted to the high-gain regime, where it was designed to selectively suppresses two parasitic resonances, yielding a predicted squeezing level of 6.49 dB. The squeezing calculations presented in this chapter build on the theoretical methods that were introduced in Chapter 2.

The principles and results discussed here highlight the versatility of interferometric coupling strategies for quantum photonics. The Mach-Zehnder resonant interferometric coupler architecture overcomes the limitations of conventional ring resonators and provides a reconfigurable platform for optimizing quantum light generation. In Chapter 4, we will further refine this design by addressing material and geometric optimization. In Chapter 5, we will explore an additional application of the Mach-Zehnder resonant interferometric coupler device, consisting in the realization of bound states in the continuum through the complete uncoupling of one resonance involved in photon-pair generation. Finally, in Chapter 6, we will present a second interferometric coupler architecture based on a Sagnac interferometer to optimize spontaneous emission from a dipole.

Chapter 4

Platform Optimization

In the previous chapter, we demonstrated the generation of squeezed light using a Mach-Zehnder resonant interferometric coupler, both in the low-gain and high-gain regimes. The platform parameters used there were primarily chosen to match common values in the literature or the characteristics of our prototype sample, which was fabricated in a wafer with predetermined waveguide geometry. In this chapter, we move further, investigating more in detail some design parameters and the interplay between them. Our goal is to identify practical guidelines for enhancing a resonator's performance in realistic fabrication constraints. For simplicity, we focus on a ring resonator, but our findings can be applied straightforwardly to more complex structures such as the MZ-RIC.

We start by analyzing the choice of the material platform, considering the trade-off between linear and nonlinear properties and fabrication compatibility. We then review the effects of the waveguide geometry on dispersion engineering, loss, backscattering, and nonlinear response. Finally, we propose a concrete design strategy to account for all the effects mentioned above while constraining the parameter space to a tractable set of configurations. As a case study to guide our optimization strategy, we focus on enhancing heralded single-photon source performance, but our method provides broader insights applicable to other quantum photonic applications requiring different regimes and figures of merit.

4.1 Material Platform Selection

The choice of material platform fundamentally determines the performance limits of integrated nonlinear photonic devices. We review here the properties of some common $\chi^{(3)}$ nonlinear materials, of highlighting the trade-offs between nonlinearities, losses, and fabrication complexity. The nonlinear refractive index n_2 directly governs the strength of third-order nonlinear interactions, with highly nonlinear materials such as silicon-rich nitride ($\mathrm{Si_7N_3}$) offering $n_2 = 28\ \mathrm{nm^2/W}$, aluminum gallium arsenide (AlGaAs) providing $n_2 = 26\ \mathrm{nm^2/W}$, and indium phosphide (InP) delivering $n_2 = 27\ \mathrm{nm}^2/\mathrm{W}$ [104] [105] [106]. These high-nonlinearity platforms enable efficient four-wave mixing and enhanced squeezing generation at reduced pump powers, making them attractive for applications requiring strong nonlinear interactions.

However, nonlinearity alone does not determine device performance, as propagation losses fundamentally limit the achievable interaction lengths and quality factors. Low-loss materials such as silicon nitride (Si_3N_4) with propagation losses of 0.03 dB/cm, chalcogenide glasses with As_2S_3 reaching 0.06 dB/cm, and silicon dioxide (SiO_2) with losses below 0.01 dB/cm enable high-quality factor resonators essential for efficient nonlinear processes [107] [108]. The superior loss characteristics of these platforms allow for extended interaction lengths and enhanced field confinement, partially compensating for their lower nonlinear coefficients.

Table 4.1: Material properties for spontaneous four-wave mixing generation in integrated photonics platforms.

Material	**Kerr index n_2 (nm^2/W)**	**Propagation Loss (dB/cm)**	**TPA @1550 nm**	**CMOS Compatible**
Si_3N_4	0.24–0.25 [107] [108]	0.03 [107] [108]	NO [109]	YES [109]
AlN	0.23 × [109]	0.14–0.42 [110] [111]	NO [109]	YES [112]
SiC	0.48–0.50 [113] [114]	3–7 [113]	NO [114]	YES [114]
As_2S_3	2.5–11 [109, 115]	0.06–4 [109]	SMALL [109]	LIMITED [115, 116]
InP	27 [106] [117]	0.4 [118]	YES [109] [106]	NO [119]
Si_7N_3	28 [104]	6 [104]	NO [120]	YES [107] [120]
AlGaAs	26 [105] [104]	0.45–40 [109]	YES [109]	NO [109]
GaInP	9.4 [121]	10–12 [109]	YES [121]	NO [109]
Si	6.5 [104]	0.1–7 [109]	YES [109]	YES [109]

An additional critical consideration is two-photon absorption (TPA), which introduces nonlinear losses that directly compete with desired third-order processes. Materials exhibiting significant TPA at the operating wavelength, including silicon, AlGaAs, GaInP, and InP, suffer from reduced conversion efficiency and increased thermal effects [109] [106] [121]. For applications requiring low-loss operation and high pump powers, TPA-free materials such as Si_3N_4, aluminum nitride (AlN), and silicon carbide SiC are essential.

Table 4.1 summarizes the key properties of various integrated photonics platforms, revealing the trade-offs between nonlinearity, loss, TPA characteristics at telecommunications wavelengths, and fabrication requirements. For our platform optimization, we select silicon nitride as the primary material due to its good balance between losses and nonlinearity and its CMOS compatibility [107] [109]. This material selection prioritizes fabrication accessibility and loss minimization over maximum nonlinearity, reflecting the requirements of quantum photonic applications where low-noise operation and large-scale fabrication are paramount. Alternative platform choices may be justified in different contexts: specialized fabrication facilities with access to high-quality III-V semiconductor growth can exploit the superior nonlinearity of AlGaAs or InP platforms despite their non-CMOS nature; applications tolerating higher losses or specifically exploiting TPA effects might benefit from silicon platforms; systems requiring ultra-high nonlinearity with acceptable loss penalties could employ silicon-rich nitride or chalcogenide glass platforms. However, for the broad class of quantum photonic applications requiring low-noise, high-efficiency operation with accessible fabrication, silicon nitride provides the optimal foundation for platform optimization.

4.2 Waveguide Parameters

Having chosen to focus on a silicon nitride, we now address the waveguide design, starting from the effects of height h and width w on some important figures of merit for a straight waveguide. Then, we move to the description of bent waveguides and ring resonators of radius R. Throughout our analysis, we fix a waveguide with a silica cladding thickness of 15 µm both above and below, as shown in Fig. 4.1, to ensure that there is no interaction with the underlying substrate. We also fix the operating wavelength at 1550 nm.

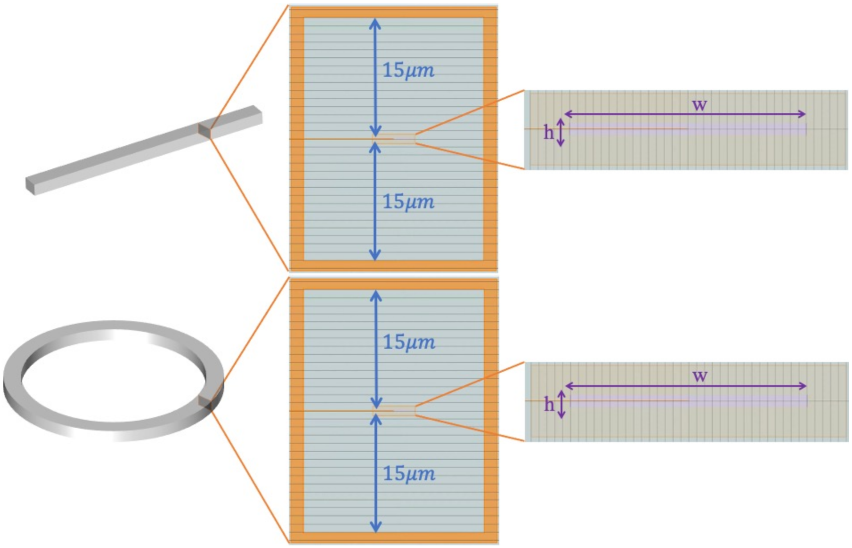

Figure 4.1: Sketch of the two kinds of structures considered for this analysis. (a) A straight waveguide, and (b) A bent waveguide, such as that forming a ring resonator, with bending radius R. The waveguide cross-section is shown on the left: a silicon nitride core of height h and width w, with 15 µm layers of silica both above and below the silicon nitride layer. The orange grid represents the simulation area we used in our numerical calculations.

4.2.1 Dispersion Engineering

Dispersion engineering represents a critical aspect of nonlinear photonic design, fundamentally determining the phase-matching conditions, spectral bandwidth, and efficiency of both second-order ($\chi^{(2)}$) and third-order ($\chi^{(3)}$) nonlinear processes [122]. In spontaneous four-wave mixing, group velocity dispersion plays a particularly crucial role in compensating for the nonlinear phase shifts induced by self-phase modulation (SPM) and cross-phase modulation (XPM).

Both SPM and XPM arise from the intensity-dependent refractive index and tend to redshift ring resonances. However, XPM exhibits twice the strength of SPM, resulting in differential frequency shifts between pump, signal, and idler modes [123]. In single-pump operation, this asymmetry manifests as a smaller shift of the pump resonance compared to signal and idler resonances. Anomalous dispersion can compensate for this differential shift, restoring the phase-matching condition essential for efficient nonlinear conversion. Conversely, dual-pump configurations require normal dispersion to achieve proper phase matching. The magnitude of both SPM and XPM scales with pump power, necessitating higher absolute group velocity dispersion values in high-gain regimes such as intense squeezed light or bright frequency comb generation. For photon-pair applications, operating at modest pump powers, the GVD is not as crucial, and more modest values prove sufficient.

Several approaches exist for controlling waveguide dispersion. Material engineering involves selecting or combining different core and cladding materials [124, 120], while structural modifications encompass engineering the entire resonator architecture [91]. However, geometric optimization of the waveguide cross-section offers the most practical approach [122], as material combinations are constrained by fabrication compatibility and structural modifications may affect other crucial parameters such as nonlinearity and losses.

We employed the Ansys Lumerical two-dimensional Finite Difference Element (FDE) solver to calculate the fundamental transverse electric modes of straight silicon nitride waveguides. The computational domain, illustrated in Fig. 4.1, comprises a silicon nitride core surrounded by a 15-µm silica cladding with perfectly matched layer boundaries. Material properties were defined using the libraries by Philipp [125] for silicon nitride and Philipp-Palik [126] for silica.

The effective index of the fundamental mode was computed across a parameter space spanning waveguide heights from 100 to 800 nm and widths from 1000 to 3000 nm. For each geometric configuration, modal indices were calculated over the wavelength range 1350-1750 nm and fitted with a quadratic dispersion relation to obtain the effective index, group index, and group velocity dispersion Eq. (1.3).

Fig. 4.2 presents the computed group velocity dispersion across the investigated parameter space. The dispersion is predominantly normal, except for a slightly anomalous dispersion region that emerges for thick waveguides, in the range $h > 700$ nm, where GVD values approach -0.07 ps^2/m. This anomalous

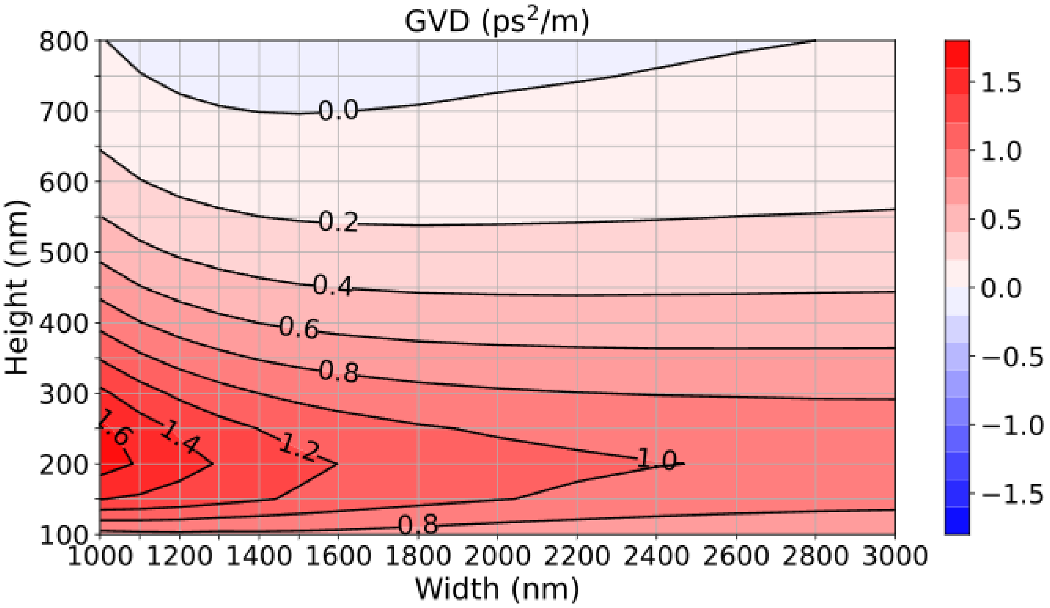

Figure 4.2: Group velocity dispersion as a function of the waveguide height and width.

region may prove valuable for single-pump SFWM applications requiring high pump powers, for which it might be worth exploring even thicker waveguides. Conversely, the highest normal GVD of 1.69 ps^2/m is reached for narrow, thin waveguides at $w = 1000$ nm and $h = 200$ nm.

4.2.2 Loss Analysis and Modeling

Understanding and predicting propagation losses is therefore essential for optimizing device performance. For instance, in photon-pair generation, the loss of either photon from a correlated pair destroys the possibility to herald the other one, and leads to spurious uncorrelated counts [82].

A well-established theoretical framework to model losses in high-contrast waveguides is the Payne-Lacey model, which correlates sidewall roughness parameters directly to optical losses [127]. This model expresses the scattering loss parameter as:

$$\alpha = \frac{8 \times 4.34\mathrm{rms}^2}{k_0^4 w^4 n_{\mathrm{co}}} g \cdot f, \tag{4.1}$$

where rms represents the root-mean-square roughness of the waveguide, k_0 is the free-space wave vector, n_{co} is the core refractive index, and the functions g and f depend on waveguide index contrast and roughness correlation length, respectively.

For bent waveguides and ring resonators, Roberts *et al.* introduced a correction factor to the Payne-Lacey model to account for enhanced mode-sidewall interaction in curved geometries [128]. The modified Payne-Lacey

Bending model incorporates a multiplicative factor η representing the ratio of bent-to-straight mode overlap. The Payne-Lacey model accurately captures the scattering to radiative modes due to sidewall roughness. However, other waveguide parameters, such as the height and the cladding thickness, can impact the overall loss, as they affect the field distribution inside the core, and its overlap with the radiative modes.

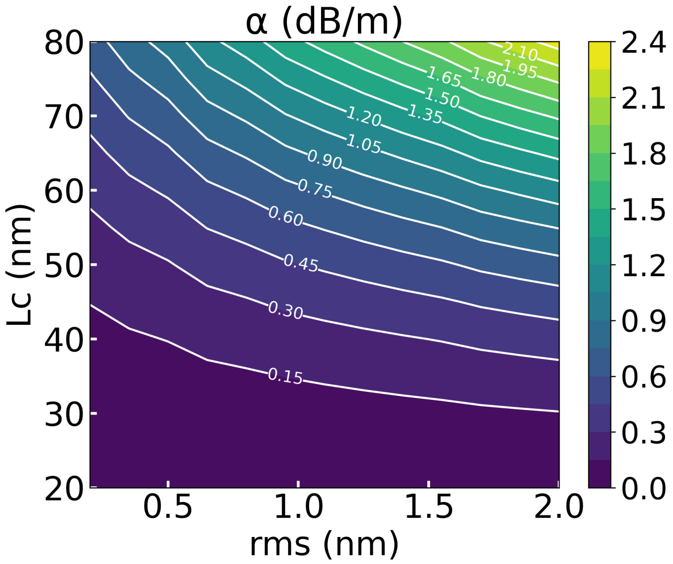

Figure 4.3: Calculated losses as a function of the roughness parameters in a silicon nitride waveguide of width 2000 nm.

A more comprehensive approach for high-contrast rectangular waveguides was developed by Poulton *et al.*, who derived a three-dimensional coupled-mode theory incorporating the full radiation mode spectrum [129]. The calculated losses as a function of height are plotted in Fig. 4.3 for a waveguide of cross section 2000x400 nm.

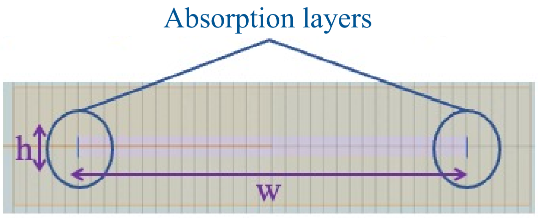

Figure 4.4: Sketch of the structure we used for FDE simulations of the sidewall roughness: a thin absorbing layer of 5 nm thickness is added at the core sidewalls. This has a real refractive index equal to the average between the core and the cladding refractive indices, and an imaginary refractive index calibrated to match the losses of a 400-nm-high waveguide.

To model this more in detail, we employ an FDE approach. We represent surface roughness through thin absorbing layers of thickness 5 nm, as shown in Fig. 4.4. These absorbing layers have a complex refractive index $n_{\text{abs}} = \text{Re}(n_{\text{abs}}) + i \cdot \text{Im}(n_{\text{abs}})$, where $\text{Re}(n_{\text{abs}}) = 1.725$ represents the unweighted average of silicon nitride and silica refractive indices and $\text{Im}(n_{\text{abs}}) = 2.62 \times 10^{-5}$ is calibrated to reproduce the Poulton model for waveguides of width $w = 2000$ nm, height $h = 400$ nm, root mean square rms $= 1.5$ nm, and coherence length $L_{\text{coh}} = 50$ nm.

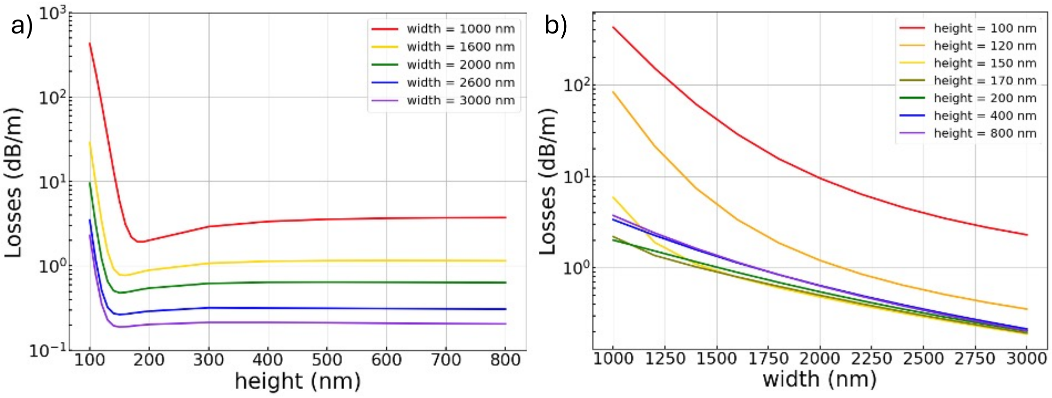

Figure 4.5: Losses calculated through a FDE approach, as a function of the waveguide height and width.

In Fig. 4.5 we plot the calculated losses as a function of waveguide width and height. Wider waveguides exhibit lower losses due to the reduced field overlap with the sidewalls, as the optical mode extends further from the perturbed interfaces. The height dependence exhibits more complex behaviour: for thick waveguides above 200 nm, losses decrease slightly with reducing height because the smaller sidewall area provides less interaction surface for scattering. However, below a critical height of approximately 150-200 nm, this trend reverses and losses increase dramatically with further height reduction. This reversal occurs because the vertically compressed mode begins interacting significantly with the top and bottom cladding interfaces, introducing additional scattering mechanisms that dominate over the sidewall area reduction.

4.2.3 Backscattering Effects

Beyond radiation losses, sidewall roughness introduces another detrimental effect: backscattering, which couples energy from forward-propagating modes into counterpropagating modes. This phenomenon becomes particularly problematic in ring resonators, where the periodic structure naturally provides phase-matching conditions for contradirectional coupling, leading to resonance splitting and degraded extinction ratios.

Little *et al.* developed a comprehensive analytical framework for predicting backscattering in ring resonators based on a coupled-mode theory [130]. Their model treats sidewall roughness as distributed polarization currents that radiate into forward, backward, and radiation modes. The effective reflectivity per unit length is given by:

$$b = \left(\frac{\omega_0 (n_{\mathrm{co}}^2 - n_{\mathrm{cl}}^2)}{2\ c\ w\ n_{\mathrm{eff}}^2} \right)^2 \sqrt{\pi} L_c e^{-(kL_c)^2} \mathrm{rms}^2, \tag{4.2}$$

where n_{cl} is the cladding refractive index, L_c is the roughness correlation length, and k is the wavevector. The maximum value is reached when $L_c = 1/(\sqrt{2}\beta_r)$, corresponding to optimal phase-matching conditions between forward and backward modes.

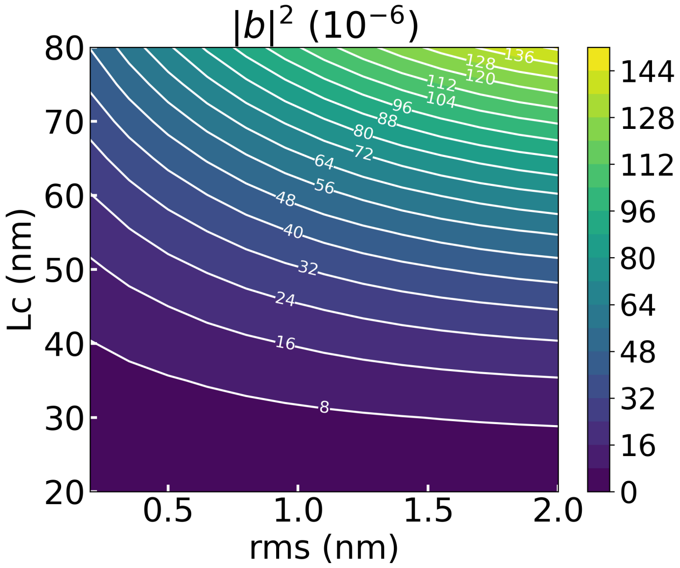

Figure 4.6: Calculated backscattering probability for a silicon nitride waveguide of length 754 nm, width 2000 nm and height 400 nm as a function of the roughness parameters.

Fig. 4.6 presents the backscattering probability $|b|^2$ for a silicon nitride waveguide of length 754 nm as a function of roughness parameters. The backscattering probability exhibits the characteristic exponential dependence on correlation length, with maximum coupling occurring at correlation lengths of 50-80 nm for our waveguide geometries.

4.2.4 Nonlinear Coefficient

The nonlinear coefficient γ_{NL} relates the nonlinear phase shift per unit length to the optical power and is defined as [40]:

$$\gamma_{\mathrm{NL}} = \frac{\omega_0 n_2}{c A_{\mathrm{eff}}}, \tag{4.3}$$

where ω_0 is the angular frequency, n_2 is the Kerr index, c is the speed of light, and A_{eff} is the effective area. The effective area quantifies the spatial extent of the optical mode and is calculated as [131]:

$$A_{\text{eff}} = \frac{\mu_0}{\varepsilon_0} \frac{3\left|\int \mathbf{e}(\mathbf{r}_\perp) \times \mathbf{h}^*(\mathbf{r}_\perp) \cdot \hat{\mathbf{z}}\, d\mathbf{r}_\perp\right|^2}{\int \frac{\chi^{(3)}(\mathbf{r}_\perp)}{\overline{\chi}^{(3)}} \left[2|\mathbf{e}(\mathbf{r}_\perp)|^4 + |\mathbf{e}(\mathbf{r}_\perp)|^2|^2\right] d\mathbf{r}_\perp}, \tag{4.4}$$

where μ_0 and ϵ_0 are the magnetic and electric susceptibilities of vacuum, $\mathbf{e}$ and $\mathbf{h}$ are the electric and magnetic field distributions, $\chi^{(3)}$ is the third-order susceptibility, and the overbar denotes a spatial average over the integration domain.

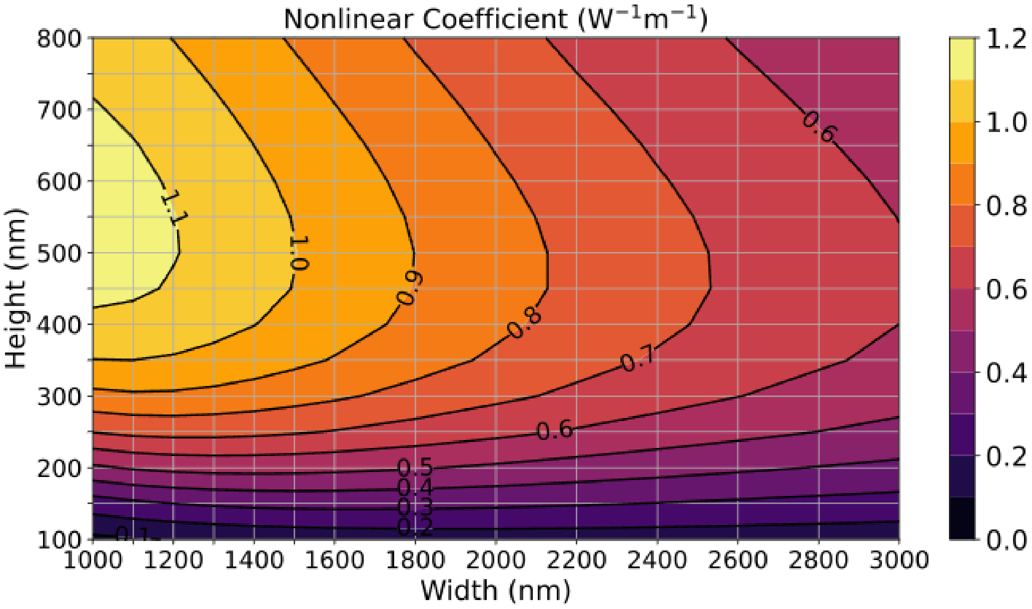

Figure 4.7: Nonlinear coefficient as a function of the waveguide height and width.

Fig. 4.7 shows the calculated nonlinear coefficient for the fundamental TE mode across our parameter space spanning heights from 100 to 800 nm and widths from 1000 to 3000 nm. For narrow waveguides in the range $400 < h < 700$ nm, the nonlinear coefficient reaches maximum values exceeding 1.15 $\text{W}^{-1}\text{m}^{-1}$ due to tight mode confinement and correspondingly small effective areas. For large widths $w > 2500$ nm or low heights $h < 250$ nm, the nonlinear coefficient decreases to below 0.6 $\text{W}^{-1}\text{m}^{-1}$ as the effective area grows, making these regions undesirable for efficient squeezed light generation.

4.2.5 Bending Radius Effects and Ring Resonators

The bending radius of ring resonators significantly influences propagation losses through mode distortion effects. We calculate this by using the FDE-solver method based on two artificial sidewall absorption layers that we introduced at the end of Section 4.2.2. In Fig. 4.8, we show the calculated losses as a function of the bending radius for a few waveguide width and height dimensions. For large radii exceeding 100 µm, bending-induced losses remain negligible compared to material and scattering losses. However, as the radius decreases below 50 µm, additional loss mechanisms become prominent due to enhanced field interaction with the outer sidewall.

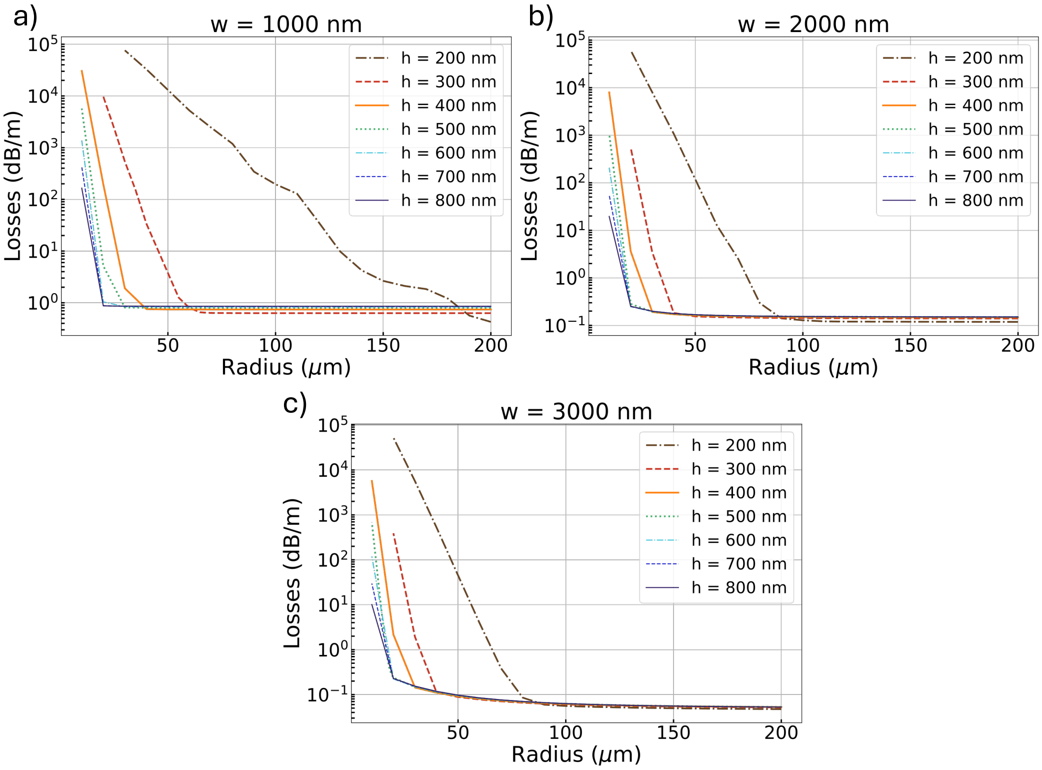

Figure 4.8: Losses as a function of the bending radius for different waveguide heights. (a) Width 1000 nm, (b) Width 2000 nm, (c) Width 3000 nm.

The radius dependence exhibits distinct scaling regimes depending on waveguide dimensions. Wide waveguides show a more rapid loss increase at small radii due to significant mode displacement, while narrow waveguides maintain more stable loss characteristics owing to tighter mode confinement. However, this same confinement makes the overall losses of narrow waveguides higher.

A second parameter that suffers from bending effects is backscattering. As it is caused by the same sidewall roughness that determines the losses, the trend of the two quantities against the bending radius is very similar. However, while losses entail scattering to non-guided modes, backscattering couples light to the counterpropagating modes of a ring resonator.

For typical fabrication parameters with root-mean-square roughness of 0.5–1.0 nm and correlation lengths of 50 − 100 nm, the backscattering probability per round-trip ranges from 10^{-6} to 10^{-4}. While these values may appear

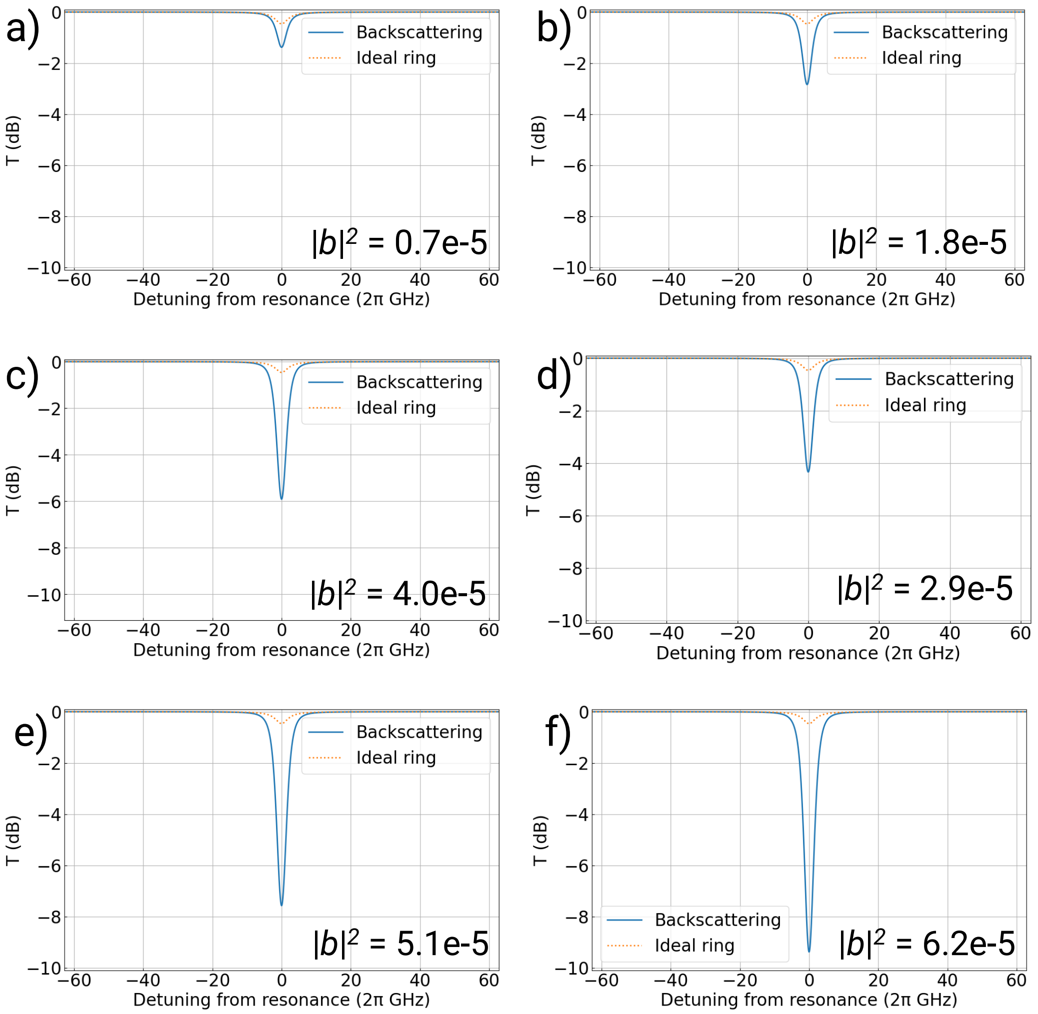

Figure 4.9: Effects of sidewall-roughness induced backscattering on a single ring resonance. The dashed orange line represents the normalized transmission of a ring without backscattering. The solid blue line represents the transmission in the presence of backscattering.

small, the cumulative effect over thousands of round-trips in high-Q resonators can build substantial counterpropagating amplitudes. Fig. 4.9 illustrates the evolution of resonance lineshapes as backscattering strength increases. For weak backscattering with $|b|^2 < 10^{-5}$, the resonances maintain their original Lorentzian profiles with negligible perturbation. However, as backscattering increases, the resonances get distorted, with a higher extinction. In resonators with very high quality factor or sidewall roughness, this distortion can eventually lead to splitting.

Beyond distributed roughness, localized defects or non-ideal point-couplers represent another source of backscattering that can be analyzed within the counterdirectional scattering matrix framework established in Section 1.1.3. These discrete perturbations arise from fabrication imperfections, material inhomogeneities, or directional couplers. To distinguish this localized effect from the distributed backscattering given by sidewall roughness, we here name it *backcoupling*.

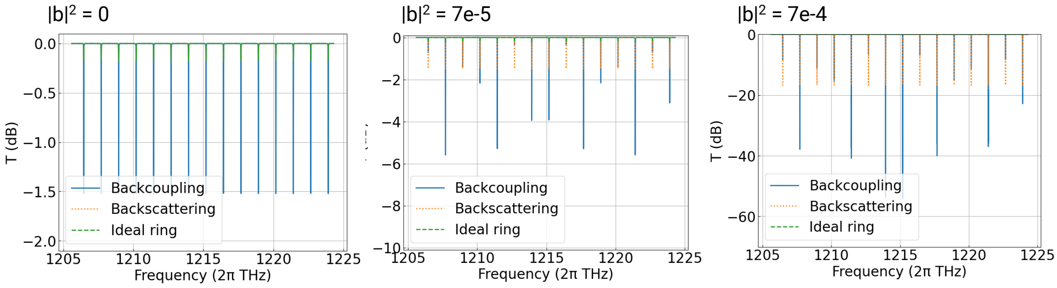

Figure 4.10: Combined effects of localized (backcoupling) and distributed (backscattering) backscattering. The transmission of an ideal ring is shown as a dashed green line, the one with distributed backscattering alone with a dotted orange line, and the one with both distributed and localized backscattering with a solid blue line.

Fig. 4.10 demonstrates the spectral impact of combining backscattering and backcoupling in a ring resonator. The interference between these two backscattering mechanisms creates resonance-dependent extinction variations that cannot be explained by either mechanism alone. Some resonances experience enhanced extinction due to destructive interference between the two coupling pathways, while others suffer degraded performance from constructive interference.

4.3 Application-Driven Design Optimization

Having established the fundamental trade-offs between dispersion, nonlinearity, losses, and backscattering, we now present a systematic methodology for optimizing waveguide parameters for specific applications. We combine the parameters discussed in the previous sections to inform the practical design of a device. We focus on low-gain SFWM for heralding applications.

4.3.1 Application Requirements

We define the generation rate as our primary figure of merit, using the expression Eq. (2.59) derived for single-pump SFWM in ring resonators [73]:

$$R_{\text{pair}} = \frac{64\gamma_{\text{NL}}^2 \mathscr{P}_P^2 v_g^4 \omega_S \omega_I}{L^2 \omega_P^4 (\omega_S Q_I + \omega_I Q_S)} \frac{Q_P^4 Q_S^2 Q_I^2}{Q_{C,P}^2 Q_{C,S} Q_{C,I}}, \tag{4.5}$$

where γ_{NL} is the nonlinear coefficient, $\mathscr{P}_P$ is the pump power, v_g is the group velocity, L is the ring circumference, $Q_{P,S,I}$ are the loaded quality factors for pump, signal, and idler modes, and $Q_{C,P,S,I}$ are the corresponding coupling quality factors. This expression captures the interplay between nonlinear efficiency, spatial confinement, and resonant enhancement.

Beyond generation rate maximization, practical heralded single-photon sources require high escape efficiency to maintain photon purity and heralding fidelity. We fix the escape efficiency at the ambitious but achievable target of $\eta = 99\%$, representing the fraction of generated photons that successfully exit the resonator rather than being lost to propagation mechanisms.

4.3.2 Quality Factor Analysis

The escape efficiency relates to quality factors through $\eta = \Gamma_C/\Gamma_L$, where Γ_C represents the coupling-limited linewidth and Γ_L is the total loaded linewidth. The loaded linewidth comprises contributions from coupling, scattering losses, and backscattering: $\Gamma_L = \Gamma_C + \Gamma_{\text{loss}} + \Gamma_{\text{back}}$.

Following our loss analysis, we express the linewidth contributions as:

$$\Gamma_{\text{loss}} = (1 - e^{-2\alpha L}) \cdot \text{FSR}, \tag{4.6}$$

$$\Gamma_{\text{back}} = |b|^2 \cdot \text{FSR}, \tag{4.7}$$

where α represents the propagation loss per unit length, L is the resonator circumference, $|b|^2$ is the backscattering probability amplitude per round-trip, and FSR is the free spectral range.

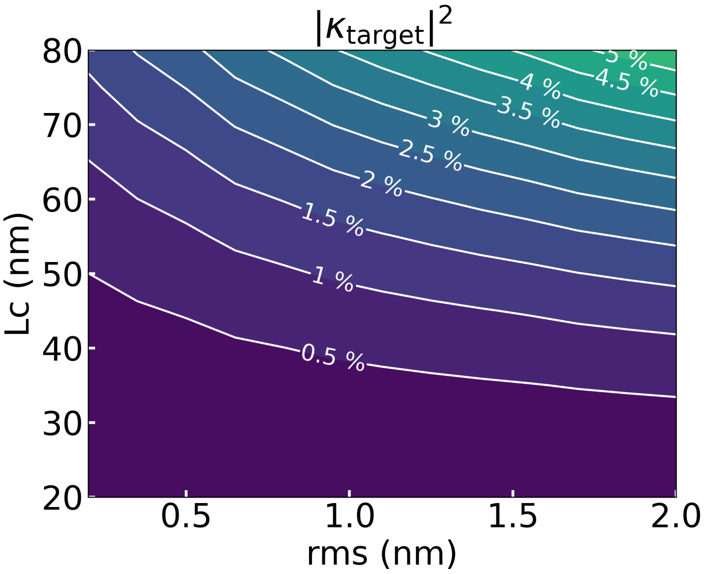

Figure 4.11: Target coupling coefficient to reach an escape efficiency of 99% with the given sidewall roughness.

Combining the escape efficiency constraint with these linewidth expressions yields the target coupling coefficient:

$$\kappa_{\text{target}} = \eta_{\text{target}} \frac{(1 - e^{-2\alpha L}) + |b|^2}{1 - \eta_{\text{target}}}. \tag{4.8}$$

This relationship reveals that achieving high escape efficiency requires increasingly strong coupling as losses and backscattering increase, as shown in Fig. 4.11.

From the target coupling coefficient, we derive the corresponding quality factors: $\Gamma_C^{\text{target}} = |\kappa_{\text{target}}|^2 \cdot \text{FSR}$ and $\Gamma_L^{\text{target}} = \Gamma_C^{\text{target}} + \Gamma_{\text{loss}} + \Gamma_{\text{back}}$. The quality factors follow as $Q_X = \omega_0 / \Gamma_X$ for $X \in \{\text{loss}, \text{back}, C\}$.

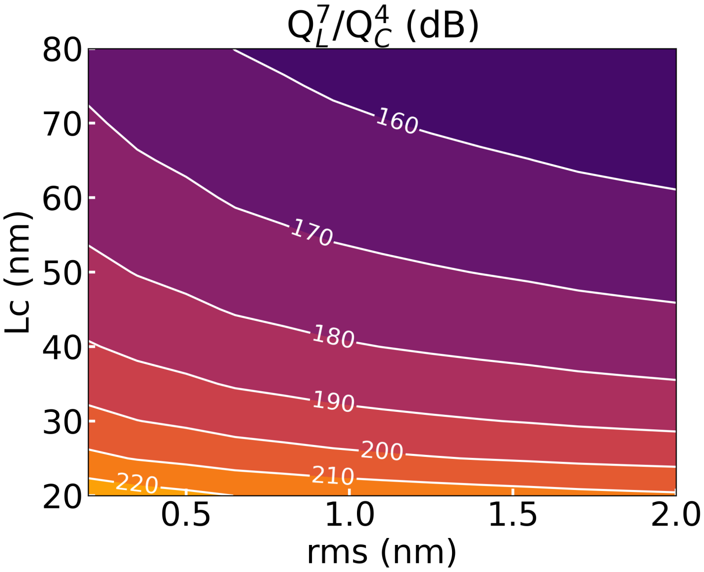

Figure 4.12: Figure of merit Θ, defined as a ratio between loaded and coupling quality factors. The higher this ratio, the higher will be the generation rate.

Substituting these expressions into the generation rate formula Eq. (4.5), and assuming identical resonances for simplicity, enables calculation of the optimal quality factor ratio $\Theta(\eta, \sigma, L_c) = Q_L^{\text{target }7} / Q_C^{\text{target }4}$, which represents the figure of merit for achieving the desired escape efficiency given fixed roughness parameters. This is illustrated in Fig. 4.12 as a function of roughness parameters. As expected, a smaller roughness leads to lower losses and higher Θ, which implies higher generation rates.

4.3.3 Waveguide Geometry

All this treatment was done at a fixed radius of 200 nm. However, smaller radii lead to increased scattering and losses, leading to smaller quality factors. On the other hand, they increase the confinement and the overall rate.

We fix the roughness parameters: rms = 1 nm and $L_{\text{coh}} = 50$ nm, and we fix a maximum target coupling coefficient of $\kappa = 2\%$, which is twice the value that we would derive in a straight waveguide. Based on our quality factor analysis, this limits the tolerable bending losses to 0.9 dB/m, which is twice the value that one would have in a straight waveguide with this roughness.

For each waveguide cross-section, we select the minimum viable radius that allows for losses below 0.9 dB/m, to maximize spatial confinement, enhance nonlinearity through reduced effective area, and increase the free spectral range for experimental convenience.

Using the calculated minimum radius for each geometry, we evaluate the complete figure of merit, namely the expected generation rate, by substituting all optimized parameters into Eq. (4.5). The resulting generation rate per unit pump power reveals the optimal trade-offs between the competing design objectives. We show this predicted generation rate in Fig. 4.13 across our design space, by assuming a pump power of 1 mW. The analysis suggests that the best performance should be achieved with high waveguides and radii of around 30 μm. The dependence on the width is less critical. Despite their higher nonlinearity, narrow waveguides are slightly disfavoured due to their increased sidewall scattering losses. However, this effect is small and might be balanced out by the fact that larger coupling coefficients are more easily achieved with narrower waveguides.

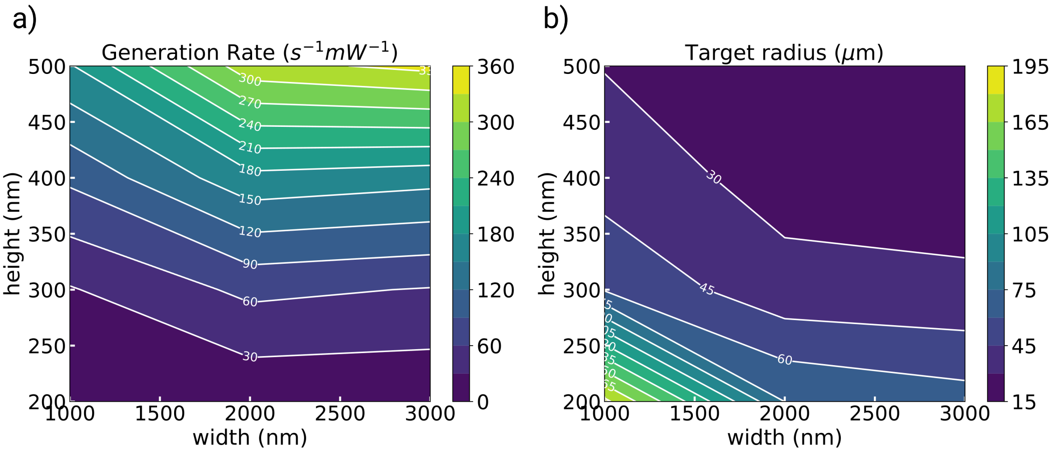

Figure 4.13: (a) Expected generation rates per milliwatt pump power and (b) corresponding target radius at which this rate is achieved.

This systematic optimization methodology demonstrates how fundamental material and geometric constraints, combined with application requirements, can guide the choice of practical design parameters. The approach can be readily adapted to other applications by modifying the figure of merit while maintaining the same underlying framework.

4.4 Conclusion

In this chapter, we addressed the optimization of photonic integrated architectures for quantum light generation, focusing on the interplay between material properties, waveguide geometry, and device performance. Most of these features, if taken singularly, are well understood. However, the problem of accounting for all of them in a practical design is still open.

We began by discussing the selection of the material platform, emphasizing the trade-offs between nonlinearity, losses, and fabrication compatibility. After choosing silicon nitride on silica as the preferred material, we used the Ansys Lumerical finite difference element simulator to systematically analyze the platform dispersion engineering, propagation losses, backscattering, and nonlinear coefficients as functions of the waveguide dimensions. To model the losses induced by sidewall roughness, we introduced in our simulation two absorption layers with a complex refractive index at the waveguide sidewalls. This allowed us to study the impact of curvature on the total waveguide loss. Combining these insights with the scattering matrix theory from Chapter 1, we investigated how the increased loss and backscattering in bent waveguides influence the quality factor and resonance splitting of a ring resonator as a function of its bending radius.

Finally, we introduced an application-driven design optimization strategy, tailoring the discussion to high-purity heralded single-photon generation, which is a key application of the Mach-Zehnder resonant interferometric coupler described in Chapter 3. Our approach began by identifying critical target metrics for the process, namely the extraction efficiency and generation rate. Leveraging the insights from our earlier analysis of losses, backscattering, dispersion, and nonlinearity, we derived the optimal parameters for the system. Given fixed values for the coupling coefficient and sidewall roughness (constrained by fabrication limitations), we determined the maximum tolerable loss, which in turn defined the target quality factors. For each waveguide width and height, we then calculated the corresponding nonlinear parameter and the minimum radius compatible with the tolerable losses. Using these parameters and the analytical results from Chapter 2, we computed the expected pair generation rate and identified the optimal cross-section that maximizes it.

While this analysis focused on low-gain single-pump spontaneous four-wave mixing in ring resonators with rectangular waveguides, the strategy is broadly adaptable to other nonlinear processes and geometries. The first step is to identify parameters constrained by technological or fundamental requirements, such as escape efficiency, sidewall roughness, and coupling coefficient. From these, through finite difference element simulations, one can derive initial constraints on the platform (e.g., maximum tolerable loss and ring quality factors). Finally, by defining a process-specific metric (e.g., generation rate), one can optimize the remaining free parameters within a reduced parameter space.

Chapter 5

Bound States in a Resonant Interferometric Coupler

In Chapter 3, we explored how the quality factor control provided by a Mach-Zehnder resonant interferometric coupler enables the optimization of squeezed light generation. In that context, we worked with overcoupled resonances to achieve a high extraction efficiency. The same platform allows the exploration of the opposite regime: complete uncoupling, where a resonant mode is perfectly confined in the main ring despite its frequency lying within the continuum of radiating modes that are supported by the bus waveguide. Such an uncoupled mode constitutes in effect a Bound State in the Continuum (BIC).

Notably, thanks to the reconfigurable resonant conditions of the MZ-RIC, one can generate photon pairs with the signal in a radiating mode and the idler in the BIC mode, thus making the properties of the BIC directly accessible in a realistic experiment. In this chapter, we theoretically investigate this kind of BIC-enhanced SFWM process. We begin by defining BICs and reviewing their fundamental properties. Then, based on the asymptotic field theory, we develop a theoretical framework for calculating photon-pair generation rates in BIC-enhanced configurations. Finally, we discuss practical implementation strategies for realizing BICs through the MZ-RIC architecture.

5.1 Bound States in the Continuum

BICs are resonant modes that lie within the continuous frequency range of radiating states in an open system and yet remain perfectly confined without coupling to the radiating channels [132, 133]. They can be classified according to their underlying physical mechanism.

- Symmetry-protected BICs arise when the confined and radiating modes belong to different symmetry classes that are orthogonal to each other [134]. For instance, antisymmetric modes in structures with in-plane symmetry cannot couple to symmetric plane waves propagating as radiation channels [133].

- Fabry-Perot BICs form when two cavities act as perfect reflectors only at some discrete resonant frequencies, trapping waves between them while transmitting all the other frequencies [132, 133].
- Friedrich-Wintgen, or accidental, BICs occur when destructive interference suppresses radiation through all available channels at specific parameter values, often manifesting near the avoided crossings of resonances [135, 132, 133].
- Separable BICs exist in systems that can be decomposed into a number of subsystems. If bound states are supported in each of the subsystems, then the tensor product of these states will remain localized in the higher-dimensional system even when its eigenvalue lies within a continuous spectrum of radiating modes [132].

The distinction between these mechanisms is not always sharp, as the same physical system may support BICs through different mechanisms at different points in the parameter space.

The concept of BICs was first introduced theoretically by von Neumann and Wigner in 1929 as a curiosity arising in quantum electronic systems [136]. BICs have since been identified across many diverse physical systems, both quantum [137, 138] and classical [132].

These studies hold substantial interest for both fundamental and applied reasons. From a fundamental perspective, BICs challenge conventional understanding of wave confinement and provide insights into the topological properties of a system [139]. From an applications standpoint, the light confinement with high quality factors can, in principle, enhance light-matter interactions. In photonics, this is desirable for lasing with reduced thresholds [140, 141], sensing [142, 143], enhanced nonlinear processes [144, 145, 146], and low-loss optical waveguiding [147].

While true BICs represent ideal states with infinite quality factors and zero linewidth, any perturbation breaking the exact conditions for a BIC, whether through structural asymmetry, material losses, fabrication imperfections, or intentional symmetry breaking, produces a state with a finite quality factor [133]. This kind of states is often called quasi-BIC, and typically maintains a strong field localization and a high quality factor, which gets higher as the conditions approach those of the BIC. Since true BICs are completely decoupled from radiating waves, they are invisible in scattering experiments and cannot be excited or accessed. For this reason, experimental observations and practical applications invariably involve quasi-BICs, while the BIC properties are only extrapolated as a limit of the quasi-BICs.

5.2 BIC-enhanced SFWM: a Toy Model

We start by neglecting the specific geometry of the MZ-RIC, assuming it behaves as a simple lossless ring resonator point coupled to a bus waveguide with a frequency-dependent coupling coefficient $\kappa(\omega)$. Under these hypotheses, one can easily consider the case in which $\kappa(\omega) = 0$ in a small range around the BIC frequency ω_{BIC} and $\kappa(\omega)$ is finite at all the other frequencies. The resulting field distribution is shown in Fig. 5.1: at the pump and signal frequencies, only the asymptotic field exists, and it is finite both in the ring and in the waveguide. At the BIC frequency, the asymptotic field propagates only through the waveguide, while the BIC mode is confined in the ring. It is important to notice that an infinite quality factor does not necessarily correspond to an infinite field. If no light is generated directly in the ring, the field in the BIC mode remains zero regardless of the power of the injected light.

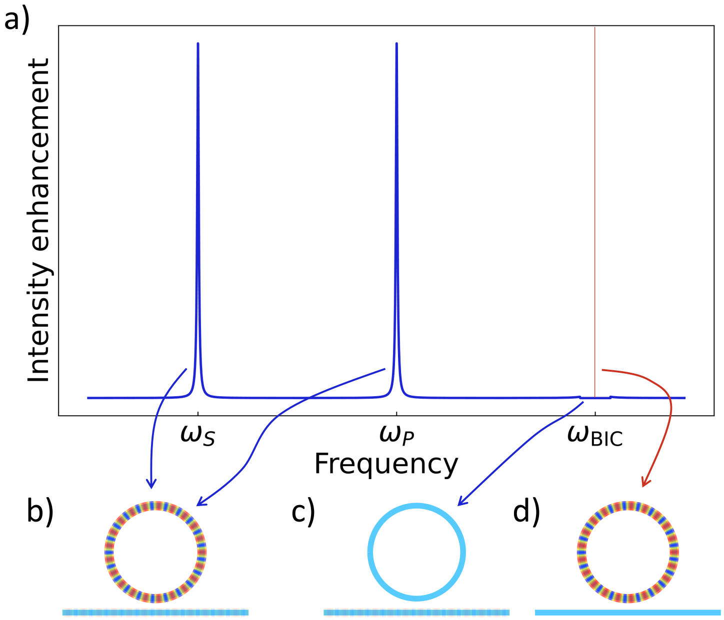

Figure 5.1: (a) Field enhancement of a ring resonator with the coupling coefficient of the BIC resonance posed artificially to zero. The red line indicates the BIC mode with zero linewidth. (b-d) Field distributions on resonance. For the signal and pump resonance, the field injected from the outside is partly coupled into the ring and partly transmitted (b); at the BIC frequency, the asymptotic-in field does not couple into the ring (c), while any light generated directly in the BIC mode remains confined there (d).

Building on the asymptotic-field theory discussed in Chapter 2, we study a single-pump SFWM process generating light directly in the BIC mode, with the pump and signal tuned at two coupled ring resonances. Since the BIC is not a radiative mode, the standard asymptotic fields do not form a complete basis anymore, as they can only describe fields that are injected or extracted from the structure. We extend the theory to include bound modes and write the displacement field operator as

$$\mathbf{D}(\mathbf{r}) = \sqrt{\frac{\hbar\omega_{\mathrm{BIC}}}{2}}\mathbf{D}^{\mathrm{BIC}}_{\omega_{\mathrm{BIC}}}(\mathbf{r})\hat{b}_{\omega_{\mathrm{BIC}}} + \int_0^\infty \mathrm{d}\omega\,\sqrt{\frac{\hbar\omega}{2v_g}}\hat{a}_\omega \mathbf{D}^{\text{asy-in}}_\omega(\mathbf{r}) + \text{H.c.}, \tag{5.1}$$

where $\hat{b}_{\omega_{\mathrm{BIC}}}$ is the annihilation operator associated the BIC, $\hat{a}_\omega$ the one associated to an asymptotic-in field, v_g is the group velocity, and $\mathbf{D}^{\mathrm{BIC}}_{\omega_{\mathrm{BIC}}}$ and $\mathbf{D}^{\text{asy-in}}_\omega(\mathbf{r})$ are the displacement fields associated to the corresponding modes. Here we stress that $\hat{b}_{\omega_{\mathrm{BIC}}}$ is dimensionless while $\hat{a}_\omega$ has the units of $s^{1/2}$. We also point out that $[\hat{b}_{\omega_{\mathrm{BIC}}}, \hat{a}_\omega] = 0$, even when $\omega = \omega_{\mathrm{BIC}}$, because the BIC does not couple to the radiative modes.

Here, for simplicity, we assume that the transverse field profile $\mathbf{d}(\mathbf{r}_\perp, \zeta)$ in the ring resonator is identical to that of the channel waveguide, except for the field direction, which changes in the plane according to the direction of the ring waveguide. For the asymptotic modes, one can write

$$\mathbf{D}^{\text{asy-in, ring}}_\omega(\mathbf{r}) = \frac{i\,\kappa(\omega)}{1-\sigma(\omega)e^{ik(\omega)L}}\,\frac{\mathbf{d}(\mathbf{r}_\perp, \zeta)}{\sqrt{2\pi}}\,e^{ik(\omega)\zeta}, \tag{5.2}$$

where k is the wavevector component in the propagation direction ζ along the resonator, and L is the resonator's length. For the bound mode, one has

$$\mathbf{D}^{\text{BIC, ring}}_{\omega_{\mathrm{BIC}}} = N_{\mathrm{BIC}}\mathbf{d}(\mathbf{r}_\perp, \zeta)\mathrm{e}^{ik(\omega_{\mathrm{BIC}})\zeta}, \tag{5.3}$$

where N_{BIC} is a normalization factor to be determined. To do that, we impose the field normalization condition

$$\int d\mathbf{r}\frac{\mathbf{D}^{\text{BIC, ring}\;*}_{\omega_{\mathrm{BIC}}}(\mathbf{r})\mathbf{D}^{\text{BIC, ring}}_{\omega_{\mathrm{BIC}}}(\mathbf{r})}{\varepsilon_0\varepsilon_r}\,\frac{v_p(\mathbf{r}_\perp;\omega_{\mathrm{BIC}})}{v_g(\mathbf{r}_\perp;\omega_{\mathrm{BIC}})} = 1. \tag{5.4}$$

Consequently, since $\mathbf{d}(\mathbf{r}_\perp, \zeta)$ is normalized to 1, we find

$$1 = \int d\mathbf{r}_\perp \frac{\mathbf{d}^*(\mathbf{r}_\perp, \zeta)\mathbf{d}(\mathbf{r}_\perp, \zeta)}{\varepsilon_0\varepsilon_r}\,\frac{v_p(\mathbf{r}_\perp;\omega_{\mathrm{BIC}})}{v_g(\mathbf{r}_\perp;\omega_{\mathrm{BIC}})}\int_0^L d\zeta N^2_{\mathrm{BIC}} = 1\cdot N^2_{\mathrm{BIC}}L, \tag{5.5}$$

from which

$$N_{\mathrm{BIC}} = \sqrt{\frac{1}{L}}, \tag{5.6}$$

$$\mathbf{D}^{\text{BIC, ring}}_{\omega_{\mathrm{BIC}}}(\mathbf{r}) = \frac{\mathbf{d}(\mathbf{r}_\perp, \zeta)}{\sqrt{L}}\,e^{ik(\omega_{\mathrm{BIC}})\zeta}. \tag{5.7}$$

The expression of the BIC Eq. (5.7) describes a field enhancement that depends only on the resonator length and is associated with a normalized energy. On the contrary, the asymptotic field Eq. (5.2) has a frequency-dependent intensity enhancement and is associated with a normalized flux density, which is more suitable to describe a propagating wave.

We now consider the case in which the nonlinear interaction involves three asymptotic fields (two for the pump and one for the signal frequency) and a BIC as the idler frequency. We start with the usual nonlinear Hamiltonian Eq. (1.45) and, by keeping only the term associated with SFWM, we obtain

$$\begin{aligned}\hat{\mathscr{H}}^{(\mathrm{SFWM})} &= -\int \mathrm{d}\omega_1 \mathrm{d}\omega_3 \mathrm{d}\omega_4 \sqrt{\omega_1\omega_{\mathrm{BIC}}\omega_3\omega_4}\, S_\perp\, \mathcal{J}(\omega_1,\omega_{\mathrm{BIC}},\omega_3,\omega_4) \\ &\times\ \hat{a}^\dagger_{\omega_1}\hat{b}^\dagger_{\omega_{\mathrm{BIC}}}\hat{a}_{\omega_3}\hat{a}_{\omega_4} + \mathrm{H.c.},\end{aligned} \tag{5.8}$$

with

$$S_\perp = \frac{\hbar^2\gamma_{\mathrm{NL}}}{2\pi^2\omega_P}, \tag{5.9}$$

and

$$\begin{aligned}\mathcal{J}(\omega_1,\omega_{\mathrm{BIC}},\omega_3,\omega_4) &= \sqrt{\frac{2\pi v_g}{L}}\frac{i\,\kappa(\omega_1)}{1-\sigma(\omega_1)e^{ik(\omega_1)L}}\frac{i\,\kappa(\omega_3)}{1-\sigma(\omega_3)e^{ik(\omega_3)L}} \\ &\times\ \frac{i\,\kappa(\omega_4)}{1-\sigma(\omega_4)e^{ik(\omega_4)L}}L,\end{aligned} \tag{5.10}$$

where we assumed a coherence length much larger than the physical length of the resonator. Here, Eq. (5.9) differs from Eq. (2.53) by a factor of 2 because the BIC and signal modes are distinguishable.

In the limit of a small generation probability per pulse, the biphoton wavefunction can be written as

$$\begin{aligned}\phi(\omega_1,\omega_{\mathrm{BIC}}) &= \frac{2i\hbar}{\beta}\,\alpha_P^2\,\frac{\gamma_{\mathrm{NL}}}{4\pi}\frac{\sqrt{\omega_1\omega_{\mathrm{BIC}}}}{\omega_P}\int \mathrm{d}\omega_3\,\phi_P(\omega_3)\,\phi_P(\omega_1+\omega_{\mathrm{BIC}}-\omega_3) \\ &\times\ \sqrt{\omega_3(\omega_1+\omega_{\mathrm{BIC}}-\omega_3)}\,\mathcal{J}(\omega_1,\omega_{\mathrm{BIC}},\omega_3,\omega_1+\omega_{\mathrm{BIC}}-\omega_3),\end{aligned} \tag{5.11}$$

where $|\alpha_P|^2$ is the average number of pump photons per pulse, γ_{NL} is the nonlinear parameter, and again the factor $\sqrt{2}$ difference between Eq. (5.11) and Eq. (2.56) arises from the BIC-signal distinguishability.

We consider a pump pulse centred at ω_P that has the form

$$\phi_P(\omega) = \frac{1}{\sqrt{\pi\Delta\omega}}\mathrm{sinc}\left(\frac{\omega-\omega_P}{\Delta\omega}\right). \tag{5.12}$$

This corresponds to a top-hat function in time of duration $\Delta T = \frac{2}{\Delta\omega}$. In the limit of a pump that is spectrally much narrower than the ring resonances, we can write $\omega_3 \approx \omega_P$, $\omega_1+\omega_{\mathrm{BIC}}-\omega_3 \approx \omega_P$ [71]. Thus,

$$\mathcal{J}(\omega_1,\omega_{\mathrm{BIC}},\omega_3,\omega_1+\omega_{\mathrm{BIC}}-\omega_3) \approx \mathcal{J}(\omega_1,\omega_{\mathrm{BIC}},\omega_P,\omega_P),$$

and the biphoton wavefunction simplifies to

$$\begin{aligned}\phi(\omega_1,\omega_{\mathrm{BIC}}) &= \frac{2i\hbar}{\beta}\,\alpha_P^2\,\frac{\gamma_{\mathrm{NL}}}{4\pi}\frac{\sqrt{\omega_1\omega_{\mathrm{BIC}}}}{\pi\Delta\omega}\mathcal{G}(\omega_1,\omega_{\mathrm{BIC}},\omega_P,\omega_P)\\ &\quad\times\int \mathrm{d}\omega_3\,\mathrm{sinc}\left(\frac{\omega_3-\omega_P}{\Delta\omega}\right)\,\mathrm{sinc}\left(\frac{\omega_1+\omega_{\mathrm{BIC}}-2\omega_P}{\Delta\omega}\right)\\ &= \frac{i\hbar}{\beta}\,\alpha_P^2\,\frac{\gamma_{\mathrm{NL}}}{2\pi}\frac{\sqrt{\omega_1\omega_{\mathrm{BIC}}}}{\pi\Delta\omega}\mathcal{G}(\omega_1,\omega_{\mathrm{BIC}},\omega_P,\omega_P)\\ &\quad\times\pi\,\Delta\omega\,\mathrm{sinc}\left(\frac{\omega_1+\omega_{\mathrm{BIC}}-2\omega_P}{\Delta\omega}\right),\end{aligned}\tag{5.13}$$

where we used the fact that $\int d\omega\,\mathrm{sinc}(\omega-x)\,\mathrm{sinc}(\omega-y)=\pi\,\mathrm{sinc}(x-y)$.

Knowing that the biphoton wavefunction must be normalized as

$$\int_{-\infty}^{\infty} d\omega_1\,|\phi(\omega_1,\omega_{\mathrm{BIC}})|^2 = 1,\tag{5.14}$$

one can calculate the average number of photon pairs that are produced per pump pulse as

$$|\beta|^2 = \int_{-\infty}^{\infty} d\omega_1\,|\beta\,\phi(\omega_1,\omega_2)|^2.\tag{5.15}$$

Alternatively, one can consider the generation rate, defined as

$$\begin{aligned}\mathfrak{R} &= \frac{|\beta|^2}{\Delta T} =\\ &= \int_{-\infty}^{\infty} d\omega_1\,\frac{\Delta\omega}{2}\,|\beta\,\phi(\omega_1,\omega_{\mathrm{BIC}})|^2 =\\ &= \frac{\Delta\omega}{2}\frac{\hbar^2\gamma_{\mathrm{NL}}^2}{8\pi^2}\,\alpha_P^4\int_{-\infty}^{\infty} d\omega_1\,\omega_1\omega_{\mathrm{BIC}}|\mathcal{G}(\omega_1,\omega_{\mathrm{BIC}},\omega_P,\omega_P)|^2\\ &\times\ \mathrm{sinc}^2\left(\frac{\omega_1+\omega_{\mathrm{BIC}}-2\omega_P}{\Delta\omega}\right).\end{aligned}\tag{5.16}$$

We consider an average number of pump photons equal to $|\alpha_P|^2=\frac{\mathcal{E}_P}{\hbar\omega_P}$, with $\mathcal{E}_P$ the energy per pump pulse. In the narrow pulse limit, it is convenient to express this in terms of the pump power $\mathcal{P}_P=\frac{\mathcal{E}_P}{\Delta T}=\frac{\Delta\omega}{2}\mathcal{E}_P$. Consequently, one can write $|\alpha_P|^2 = \frac{2\,\mathscr{P}_P}{\hbar\,\omega_P\,\Delta\omega}$, and the pair generation rate is

$$\begin{aligned}
\mathfrak{R} &= \frac{\Delta\omega}{2}\frac{\hbar^2\,\gamma_{\mathrm{NL}}^2}{4\pi^2}\frac{4\,\mathscr{P}_P^2}{\hbar^2\,\omega_P^2\,\Delta\omega^2}\,\pi\Delta\omega\,(2\omega_P-\omega_{\mathrm{BIC}})\,\omega_{\mathrm{BIC}} \\
&\quad\times|\mathscr{J}(2\omega_P-\omega_{\mathrm{BIC}},\,\omega_{\mathrm{BIC}},\,\omega_P,\,\omega_P)|^2 \\
&= \frac{1}{2\pi}\left(\frac{\gamma_{\mathrm{NL}}\,\mathscr{P}_P}{\omega_P}\right)^2(2\omega_P-\omega_{\mathrm{BIC}})\,\omega_{\mathrm{BIC}}2\pi v_g L \\
&\quad\times\frac{\kappa^2(2\omega_P-\omega_{\mathrm{BIC}})}{|1-\sigma(2\omega_P-\omega_{\mathrm{BIC}})e^{ik(2\omega_P-\omega_{\mathrm{BIC}})L}|^2}\left(\frac{\kappa^2(\omega_P)}{|1-\sigma(\omega_P)e^{ik(\omega_P)L}|^2}\right)^2 \\
&= \frac{32v_g^3}{\pi L^3}\left(\frac{\gamma_{\mathrm{NL}}\,\mathscr{P}_P}{\omega_P^2}\right)^2\omega_{\mathrm{BIC}}2\pi v_g L\;Q_{\omega_P}^2 Q_{\omega_S} \\
&= \frac{64v_g^4}{L^2}\left(\frac{\gamma_{\mathrm{NL}}\,\mathscr{P}_P}{\omega_P^2}\right)^2\omega_{\mathrm{BIC}}\;Q_{\omega_P}^2 Q_{\omega_S} \qquad (5.17)
\end{aligned}$$

where we used the fact that

$$\lim_{\Delta\omega\to 0}\frac{1}{\pi\Delta\omega}\mathrm{sinc}^2\left(\frac{\omega_1+\omega_{\mathrm{BIC}}-2\omega_P}{\Delta\omega}\right)=\delta(\omega_1+\omega_{\mathrm{BIC}}-2\omega_P)$$

and we substituted the overlap integral Eq. (5.10), approximating the resonant field enhancement as

$$\frac{\kappa^2(\omega)}{|1-\sigma(\omega)e^{ik(\omega)L}|^2}\approx\frac{4v_g}{L\omega}Q_\omega,$$

with Q_ω the loaded quality factor of the resonance centred at frequency ω, which is equal to the coupling quality factor in this lossless scenario.

5.3 Truly Bound States in a Real Device

We now explicitly construct the asymptotic fields for MZ-RIC in Fig. 3.3. We set it in a configuration in which the length of the bus waveguide arm is $l = 3L$ and its coupling coefficients to the main ring $\kappa_A = \kappa_B = \kappa$, so that all the resonances are overcoupled, but one auxiliary resonance is tuned at the BIC frequency. We keep the ratio 3/4 between the auxiliary and main ring radii, as in the rest of the thesis, although other ratios can be used; we also keep κ_C as a free parameter. The resulting field enhancement and transmission are as in Fig. 3.4(b), where we consider the second and third resonances as signal and pump, respectively, and the fourth suppressed resonance as the BIC. Again, we neglect all the losses.

The BIC field is now distributed in the bus-waveguide arm of the Mach-Zehnder interferometer and in the auxiliary resonator. We write it as

$$\mathbf{D}_{\omega_{\mathrm{BIC}}}^{\mathrm{BIC,\,ring}} = N_{\text{MZ-RIC}}f_{\text{MZ-RIC}}\mathbf{d}(\mathbf{r}_\perp,\zeta)\mathrm{e}^{ik(\omega_{\mathrm{BIC}})\zeta}, \qquad (5.18)$$

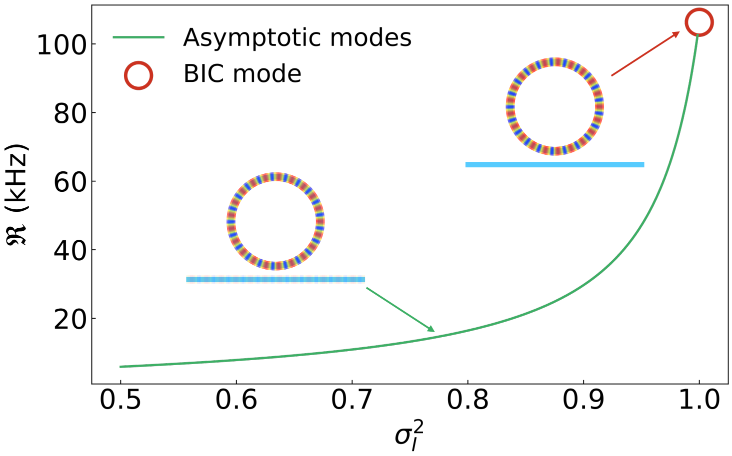

Figure 5.2: Calculated generation rate in a lossless ring resonator as a function of the self-coupling probability σ_I^2 of the idler resonance, with fixed pump and signal self-coupling probabilities $\sigma(\omega)^2 = 0.96$. The red circle is the generation rate of the BIC mode, which is exactly the limit of $\sigma_I = 1$. In this simulation we set $\gamma_{NL} = 1\ \mathrm{W}^{-1}\mathrm{m}^{-1}$, $\mathscr{P}_P = 1$ mW, $\omega_P = 1550$ nm, $L = 754$ µm, and $n_g = 2$.

where $f_{\text{MZ-RIC}}$ is a field enhancement factor defined as

$$f_{\text{MZ-RIC}} = \begin{cases} 1 & \text{in the left part of the main ring} \\ \sigma & \text{in the right part of the main ring} \\ i\kappa & \text{in the bus waveguide before the auxiliary resonator} \\ -i\kappa & \text{in the bus waveguide after the auxiliary resonator} \\ 0 & \text{elsewhere} \end{cases}, \tag{5.19}$$

where $\sigma = \sqrt{1-\kappa^2}$. Here, the fact that the field only changes its sign after the auxiliary ring resonator is due to the absence of losses and to the fact that this resonator is spectrally aligned with the BIC mode.

We point out that applying a scattering matrix theory to the BIC field Eq. (5.19) would result in an indeterminate equation for the fields at the input and output of the MZ-RIC. This is an essential feature of a Friedrich-Wintgen BIC: since the interaction region is not coupled to the outside, there are two linearly independent solutions for the fields in the structure. A straightforward way to choose these solutions is to take the first one as the BIC, with zero field outside the resonator, and the second as the asymptotic field of light injected in the structure and emitted to the output port without overlapping with the resonant field.

The normalization factor $N_{\text{MZ-RIC}}$ can be derived as in Eq. (5.4), but now we need to integrate over the whole structure. The result is

$$N_{\text{MZ-RIC}} = \sqrt{\left[1 + \frac{5}{2}\kappa^2 + \frac{\kappa_C^2}{(1-\sigma_C)^2}\right]^{-1}} \sqrt{\frac{1}{L}} := \sqrt{\frac{1}{L_{\text{eff}}}}, \tag{5.20}$$

where we defined an effective length containing the coupling-dependent prefactor. This effective length is always larger than the resonator's length.

The signal and pump states can be expressed as asymptotic fields:

$$\mathbf{D}_{\omega}^{\text{asy-in, ring}}(\mathbf{r}) = g(\omega)\, \frac{\mathbf{d}(\mathbf{r}_\perp, \zeta)}{\sqrt{2\pi}}\, e^{ik(\omega)\zeta}, \tag{5.21}$$

where $g_{\text{MZ-RIC}}$ is a field enhancement factor defined as

$$g(\omega) = \begin{cases} 1 & \text{at the input port} \\ \frac{i\kappa\sigma(1+t_C(\omega))}{1-\sigma^2+\kappa^2 t_C(\omega)} & \text{in the left part of the main ring} \\ \frac{i\kappa(1+t_C(\omega))}{1-\sigma^2+\kappa^2 t_C(\omega)} & \text{in the right part of the main ring ,} \\ -\frac{i\kappa^2(1+t_C(\omega))}{1-\sigma^2+\kappa^2 t_C(\omega)} & \text{iat the output port} \\ 0 & \text{elsewhere} \end{cases} \tag{5.22}$$

where

$$t_C(\omega) = \frac{\sigma_C - e^{i\phi_C(\omega)}}{1 - \sigma_C e^{i\phi_C(\omega)}}$$

is the transmission of the auxiliary resonator and $\phi_C(\omega) = \frac{3}{4}Lk(\omega)$, with κ the wavevector.

The nonlinear calculations are exactly as in the toy model of a single-resonator with a variable coupler, except that now the overlap integral $\mathcal{J}$ is

$$\begin{aligned} \mathcal{J}(2\omega_P - \omega_{\text{BIC}}, \omega_{\text{BIC}}, \omega_P, \omega_P) \;&=\; \sqrt{\frac{2\pi v_g}{L_{\text{eff}}}} \left(\frac{i\kappa(1+t_C(\omega_P))}{1-\sigma^2+\kappa^2 t_C(\omega_P)}\right)^2 \\ &\quad \times \frac{i\kappa(1+t_C(2\omega_P-\omega_{\text{BIC}}))}{1-\sigma^2+\kappa^2 t_C(2\omega_P-\omega_{\text{BIC}})}\sigma\frac{1+\sigma^2}{2}L. \end{aligned} \tag{5.23}$$

The resulting generation rate is

$$\begin{aligned} \mathfrak{R}_{\text{asymptotic MZ-RIC}} \;&=\; \frac{v_g L}{L_{\text{eff}}} \left(\frac{\gamma_{\text{NL}}\mathcal{P}_P}{\omega_P}\right)^2 (2\omega_P - \omega_{\text{BIC}})\, \omega_{\text{BIC}}\, \sigma \frac{1+\sigma^2}{2} \\ &\quad \times \left|\frac{i\kappa(1+t_C(\omega_P))}{1-\sigma^2+\kappa^2 t_C(\omega_P)}\right|^4 \left|\frac{i\kappa(1+t_C(2\omega_P-\omega_I))}{1-\sigma^2+\kappa^2 t_C(2\omega_P-\omega_I)}\right|^2. \end{aligned} \tag{5.24}$$

In this case, the trend is not immediately relatable to the resonance quality factor. However, Eq. (5.25) is a closed form for the rate in the presence of BICs in a real device. In such a system, it is possible to generate a finite number of photon pairs with one photon in the BIC mode and one in the signal radiating mode. One can thus detect the signal and analyze its spectral properties, reflecting the properties of the idler BIC mode. This constitutes a path to study bound states in the continuum without employing quasi-BIC modes.

5.4 Conclusion

In this chapter, we proposed the realization of bound states in the continuum using the Mach-Zehnder resonant interferometric coupler architecture introduced in Chapter 3. Similarly to what was presented there, here we harnessed the selective and tunable coupling conditions of our device to explore regimes of spontaneous four-wave mixing that are not accessible with a simple ring resonator. However, while in Chapter 3 we primarily used overcoupled resonances to generate and efficiently extract pure quantum states, here we completely uncoupled one resonance to produce a bound state in the continuum and study its behaviour from a fundamental perspective.

Before addressing the problem in the Mach-Zehnder resonant interferometric coupler, we briefly reviewed the fundamental properties of bound states in the continuum and their potential applications in quantum photonics. Then, as a first analysis, we considered a toy model with a spontaneous four-wave mixing process taking place in a simple lossless ring resonator having two coupled resonances that act as the pump and signal modes and one uncoupled resonance that acts as the idler mode. This configuration allowed the signal photons to remain detectable while preserving their correlations with the bound idler companion.

Building on the theoretical framework outlined in Chapter 2, we adapted the asymptotic-fields formalism to include non-radiative modes. With this extension, we could calculate the pair generation rates for the ring with an uncoupled idler. We proved that this rate remains finite and corresponds to the limit of a three-resonance ring system as the idler self-coupling coefficient approaches unity. Finally, we showed that, although the toy model of a simple ring resonator with a bound state is not physically realizable, a true bound state can be implemented in the Mach-Zehnder resonant interferometric coupler. The resulting spontaneous four-wave mixing pair generation rate remains finite even when the idler resonance is completely uncoupled, with an ideally infinite quality factor.

Chapter 6

Single-Photon Emission through a Sagnac Interferometer

In the previous chapters, we saw how a resonant interferometric coupler can provide enhanced control over the quantum light generated by SFWM in various contexts. We chose to study this particular parametric process for its relevance to quantum technologies. Yet, the possibility of harnessing resonances and interference for enhancing the quality of nonclassical states of light has a much broader extent. As an example, we now study a fundamentally different quantum phenomenon: spontaneous emission from a dipole, following our recent work [148].

Contrary to SFWM, dipole emission is a nonparametric process, where an excited two-level system directly transitions to its ground state through the emission of a photon. Its deterministic nature makes it suitable for generating single-photon states on demand without the need for heralding. Despite the differences, dipole emission in an integrated platform still can benefit from the light-matter interaction enhancement provided at a ring resonator's resonances [149, 150].

The theoretical framework underlying our analysis of dipole interaction with a ring resonator remains rooted in the asymptotic-field formalism introduced in Chapter 2. First, we recover the Purcell theory of cavity-enhanced emission in waveguides and ring resonators. Subsequently, we extend the treatment to backscattering-induced non-idealities, revealing, besides the expected emission rate reduction, the potential to harness the interference between counterpropagating modes for achieving directional control of the emitted light. These insights motivate our design of a Sagnac interferometer-based resonant interferometric coupler that deliberately exploits such interference for deterministic emission control. Though different from the MZ-RIC presented in Chapter 3, this Ring-Sagnac cavity can be regarded as a resonant interferometric coupler as well, which we call S-RIC.

6.1 Dipole Emitters for Single-Photon Generation

Single-photons are the simplest non-Gaussian quantum state of light and are essential for the realization of a wide range of protocols in quantum key distribution [151], quantum computing [152], and quantum metrology [153]. These applications demand sources capable of producing single photons on demand, with high emission rate, purity, and indistinguishability [154].

Several physical systems can act as quantum emitters for single-photon generation. In bulk photonics, one can use trapped atoms, ions or molecules, providing high purity, indistinguishability, and control [155]. In integrated photonics, quantum dots are well-established options, due to their high emission rates, on-demand operation, and compatibility with deterministic excitation schemes [156]. Another widely used family of emitters is colour centers, particularly nitrogen-vacancies and silicon-vacancies, which can operate at room temperature and combine with long-lived spin degrees of freedom, enabling applications in quantum memory and distributed entanglement.

These emitters are usually treated as two-level systems with a ground energy level $\mathcal{E}_g$ and an excited energy level $\mathcal{E}_e$. An external optical or electrical pulse is used to bring the system to its excited state. After a characteristic time, the dipole decays back to the ground state, emitting a photon at energy $\mathcal{E}_0 = \mathcal{E}_e - \mathcal{E}_g$. In this way, single-photon states with high purity can be generated on demand. In general, randomly oriented dipoles in a bulk medium of refraction index n have an isotropic emission with a generation rate of

$$\Gamma_0 = \frac{p^2 \omega_0^3}{3\varepsilon_0 \hbar \pi c^3}, \tag{6.1}$$

where p is the electric dipole moment of the emitter, ε_0 is the dielectric constant of vacuum, and ω_0 is the characteristic emission frequency, such that $\mathcal{E}_0 = \hbar\omega_0$.

To achieve higher brightness and a well-defined emission mode, the dipole is often embedded in an optical resonator. According to Purcell's law, a dipole aligned spectrally and spatially to a resonance has an enhanced emission rate of [148]

$$\Gamma_{\mathrm{Pur}} = \Gamma_0 \frac{3}{4\pi^2} \left(\frac{\lambda_0}{n}\right)^3 \frac{Q}{V_{\mathrm{eff}}}, \tag{6.2}$$

where λ_0 is the characteristic wavelength of the emitter in vacuum, n is the material refractive index, Q is the quality factor of the resonator, and V_{eff} is its effective mode volume. In Eq. (6.2) we can recognize two important contributions to the cavity enhancement: time confinement, which is expressed by the quality factor, and spatial confinement, which is related to the effective volume.

In practical applications, micropillar cavities have been widely used as bright and efficient single-photon sources, often combined with vertical emitters in a free-space configuration [157]. Alternatively, plasmonic cavities such as nanogaps between metallic nanospheres can confine light to extremely small volumes, leading to large Purcell enhancements and even strong coupling. However, these systems suffer from intrinsic losses and are not easily integrated into dielectric photonic platforms. Photonic crystal cavities offer much tighter integration and have demonstrated extremely high Purcell factors due to their low mode volumes and high quality factors [158]. Nevertheless, their fabrication can be demanding, and they are highly sensitive to nanofabrication imperfections, posing a challenge for reproducibility and scalability. In contrast, ring resonators can be easily interfaced with waveguides, and they offer a mature platform often compatible with standard CMOS fabrication processes [149, 150, 159]. These features make ring resonators a promising platform for scalable, integrated single-photon sources, especially when combined with quantum dots or colour centers.

Recent advances have demonstrated various approaches to achieve efficient collection and control of single-photon emission in integrated platforms. For instance, heterogeneous integration strategies have shown promise for coupling quantum emitters to low-loss waveguide networks [160], while chiral coupling mechanisms enable directional emission control through spin-momentum locking [161]. A careful design of the resonator can also provide configurability of the emission direction and spectrum [162, 163]. Building on these developments, our approach leverages interferometric control to achieve deterministic manipulation of both emission rate and output mode characteristics.

6.2 Emission Rate

As we discussed in Chapter 2, the quantization of the electromagnetic field in terms of asymptotic-in/-out modes provides a powerful and general framework to describe light-matter interactions in integrated photonic structures. This also holds when analyzing non-parametric processes, although other approaches have been succesfully applied in this field [164]. In the following, we apply the asymptotic fields formalism to calculate the generation rate of a dipole embedded in an integrated circuit. We describe the structure as a set of input/output channels with an interaction region where the dipole is located.

The interaction Hamiltonian can be expressed as [148]

$$\hat{\mathscr{H}}_I = \hat{\mathbf{p}} \cdot \hat{\mathbf{E}}(\mathbf{r}_0), \tag{6.3}$$

where $\hat{\mathbf{p}} = \mathbf{p}\,\hat{\sigma}_x$ is the dipole operator, with $\hat{\sigma}_x$ the Pauli matrix along the x direction, and $\hat{\mathbf{E}}(\mathbf{r}_0)$ is the electric field operator evaluated at the dipole position $\mathbf{r}_0 = (x_0, y_0, z_0)$. We write the electric field in terms of the asymptotic-in modes:

$$\hat{\mathbf{E}}(\mathbf{r}) = \sum_{j=1}^{N} \int_0^\infty dk \sqrt{\frac{\hbar\omega_k}{2}}\, \hat{a}_{j,k}\, \frac{\mathbf{D}_{j,k}^{\text{asy-in}}(\mathbf{r})}{\varepsilon_0 n^2(\mathbf{r})} + \text{H.c.}, \tag{6.4}$$

where N is the number of channels, $\mathbf{D}_{j,k}^{\text{asy-in}}(\mathbf{r})$ is the asymptotic-in mode field associated with channel j and wavector k, $\hat{a}_{j,k}$ is the destruction operator for that mode, and ω_k is the corresponding frequency. Under the rotating-wave approximation, only the terms responsible for photon creation in mode (j, k) contribute to the transition matrix element. The resulting Hamiltonian is [148]

$$\hat{\mathscr{H}}_I = \sum_{j=1}^{N} \int_0^\infty dk \sqrt{\frac{\hbar\omega_k}{2}}\, \hat{\sigma}_+ \hat{a}_{j,k} \frac{\mathbf{p} \cdot \mathbf{D}_{j,k}^{\text{asy-in}}(\mathbf{r}_0)}{\varepsilon_0 n^2(\mathbf{r}_0)} + \text{H.c.}, \tag{6.5}$$

where $\hat{\sigma}_+$ is the Pauli raising operator.

We consider spontaneous emission from the dipole. The initial state is $|i\rangle = |0\rangle \otimes |e\rangle$, where $|0\rangle$ denotes the vacuum state of the electromagnetic field and $|e\rangle$ is the excited state of the dipole. After the emission of one photon, the final state is $|f_{j,k}\rangle = |1_{j,k}\rangle \otimes |g\rangle$, describing the system with one photon in channel j with wavevector k and the dipole in its ground state $|g\rangle$. The corresponding energy difference is $\mathscr{E}_f - \mathscr{E}_i = \hbar(\omega_k - \omega_0)$, where ω_0 is the transition frequency of the dipole and ω_k is the frequency of the emitted photon. According to Fermi's golden rule, the emission rate to channel j is given by [148]

$$\begin{aligned} \Gamma_j &= \frac{2\pi}{\hbar} \int_0^\infty dk \left| \left\langle f_{j,k} \middle| \hat{\mathscr{H}}_I \middle| i \right\rangle \right|^2 \delta(\mathscr{E}_f - \mathscr{E}_i) =, \\ &= \frac{\pi}{\varepsilon_0^2 n^4(\mathbf{r})} \int dk\, \omega_k \left| \mathbf{p} \cdot \mathbf{D}_{j,k}^{\text{asy-in}*}(\mathbf{r}_0) \right|^2 \delta(\hbar\omega_k - \hbar\omega_0). \end{aligned} \tag{6.6}$$

For a narrowband emitter centered at ω_0, the dispersion relation can be expanded in Taylor series around ω_0 as

$$k(\omega) \approx k_0 + \frac{1}{v_g}(\omega - \omega_0), \tag{6.7}$$

where v_g is the group velocity and $k_0 = k(\omega_0)$. This allows us to simplify the Dirac delta function as $\delta(\hbar\omega_k - \hbar\omega_0) = \frac{1}{\hbar v_g}\delta(k - k_0)$. Thus, recalling that $\mathbf{D}^{\text{asy-in}*} = \mathbf{D}^{\text{asy-out}}$, the emission rate is

$$\Gamma_j = \frac{\pi\omega_0}{\varepsilon_0^2 n^4(\mathbf{r}_0)\hbar v_g} \left| \mathbf{p} \cdot \mathbf{D}_{j,k_0}^{\text{asy-out}}(\mathbf{r}_0) \right|^2. \tag{6.8}$$

The total emission rate is [148]

$$\Gamma = \sum_{j=1}^{N} \Gamma_j = \frac{\pi\omega_0}{\varepsilon_0^2 n^4(\mathbf{r}_0)\hbar} \sum_{j=1}^{N} \frac{1}{v_{g,j}} \left| \mathbf{p} \cdot \mathbf{D}_{j,k_0}^{\text{asy-out}}(\mathbf{r}_0) \right|^2, \tag{6.9}$$

where we allow for different group velocity dispersions in the N channels composing the structure.

In the following sections, we will apply this general formalism to analyze emission from a dipole coupled to some simple photonic integrated structures.

6.2.1 Dipole Emission in a Waveguide

We start by considering the simplest integrated photonic structure: a single-mode, lossless dielectric waveguide of length L, as depicted in Fig. 6.1. We assume that the dipole couples only to the guided mode of the structure. In this configuration, the asymptotic-in fields correspond to the solutions of Maxwell's equations for light travelling in the waveguide from the left (Port 1) or right (Port 2), namely a wave with a field profile $\mathbf{d}(x_0, y_0)$:

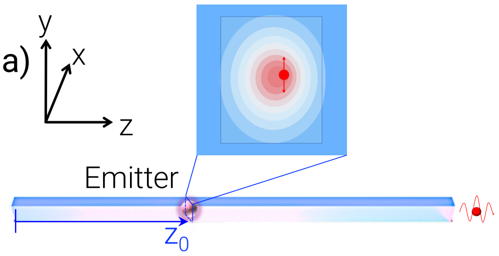

Figure 6.1: Sketch of a dipole embedded in a ridge waveguide. The inset shows the mode profile within the waveguide. Image taken from [148].

$$\mathbf{D}^{\text{asy-in}}_{1,k_0}(\mathbf{r}_0) = \frac{\mathbf{d}(x_0, y_0)}{\sqrt{2\pi}} e^{ik_0 z_0}, \tag{6.10}$$

$$\mathbf{D}^{\text{asy-in}}_{2,k_0}(\mathbf{r}_0) = \frac{\mathbf{d}(x_0, y_0)}{\sqrt{2\pi}} e^{ik_0 (L-z_0)}, \tag{6.11}$$

where z_0 is the distance of the dipole from Port 1.

For a dipole oriented along the displacement field, and using Eq. (6.8), the emission rate into each propagation direction is

$$\Gamma_{1,\text{wg}} = \Gamma_{2,\text{wg}} = \frac{p^2 \omega_0}{2\varepsilon_0^2 n^4(\mathbf{r}_0) \hbar v_g} \left|\mathbf{d}(x_0, y_0)\right|^2, \tag{6.12}$$

and the total emission rate is

$$\Gamma_{\text{wg}} = \frac{p^2 \omega_0}{\varepsilon_0 n^2(\mathbf{r}_0) \hbar v_g} \frac{|\mathbf{d}(x_0, y_0)|^2}{\varepsilon_0 n^2(\mathbf{r}_0)}. \tag{6.13}$$

It is convenient to introduce the effective area of the mode at the dipole position

$$A_{\text{eff}}(\mathbf{r}_0) = \frac{\varepsilon_0 n^2(\mathbf{r}_0)}{\mathbf{d}^2(x_0, y_0)}, \tag{6.14}$$

such that Eq. (6.13) can be rewritten as [148]

$$\Gamma_{\text{wg}} = \frac{p^2 \omega_0}{\varepsilon_0 n^2(\mathbf{r}_0) \hbar v_g} \frac{1}{A_{\text{eff}}(\mathbf{r}_0)}. \tag{6.15}$$

Equation Eq. (6.14) is a generalization of the commonly used effective area

$$\bar{A}_{\text{eff}} = \frac{\int \mathrm{d}\mathbf{r}\, \varepsilon(\mathbf{r})|\mathbf{E}(\mathbf{r})|^2}{\max[\varepsilon(\mathbf{r})|\mathbf{E}(\mathbf{r})|^2]},$$

which we recover in the assumption of a dipole located where the energy density of the electric field is maximum.

Compared to the emission rate in a bulk medium, given by Eq. (6.1), the bus waveguide provides an enhancement of [148]

$$\frac{\Gamma_{\text{wg}}}{\Gamma_0} = \frac{3}{4\pi}\left(\frac{\lambda_0}{n}\right)^2 \frac{n_g}{A_{\text{eff}}(\mathbf{r}_0)}, \tag{6.16}$$

where $n_g = c/v_g$ is the group index, and $\lambda_0 = 2\pi c/\omega_0$ is the emission wavelength in vacuum. This expression is analogous to the Purcell factor introduced in Eq. (6.2) for a resonant cavity. In the case of a waveguide, however, the spatial confinement is only two-dimensional rather than three-dimensional. As a consequence, the enhancement depends on an effective mode area $A_{\text{eff}}(\mathbf{r}_0)$ instead of an effective mode volume, and it scales quadratically rather than cubically with the wavelength. Another difference compared to the cavity case is that a waveguide does not provide true longitudinal or temporal confinement. For this reason, Eq. (6.16) does not depend on the quality factor, which in Eq. (6.2) accounted for the resonant time confinement effects. In contrast, in a waveguide, longer light-matter interaction times arise solely from the reduced propagation velocity of the guided mode. The group index n_g in Eq. (6.16) quantifies this slow-light effect.

Emission enhancement in a waveguide has been widely exploited in photonic crystal waveguides, where large n_g values can dramatically boost the emission rate through engineered dispersion. In semiconductor integrated circuits, n_g is smaller, and there is no sub-wavelength confinement; thus, the waveguide alone does not provide a sufficient enhancement. However, its role can not be neglected.

6.2.2 Beyond the Purcell Factor in a Ring Resonator

We now consider a dipole emitter embedded in a ring resonator side-coupled to a bus waveguide, as illustrated in Fig. 6.2. We adopt a cylindrical reference frame centred on the ring and define the dipole position $\mathbf{r}_0 = (\mathbf{r}_{0_\perp}, \zeta_0)$, where ζ_0 is the distance along the ring circumference from the coupling point to the bus waveguide. The ring supports two degenerate modes: one propagating counterclockwise (excited from Port 1) and one propagating clockwise (excited from Port 2). Due to the symmetry of the system, the two modes have the same longitudinal field distribution, which was derived in Eq. (1). Building on Eq. (1.14) and Eq. (6.4), we write the asymptotic-in fields of the two modes

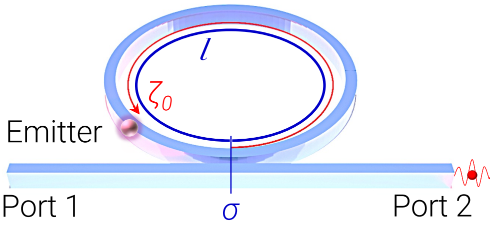

Figure 6.2: Sketch of a dipole embedded in a ring resonator. Image taken from [148].

at the dipole position as

$$\mathbf{D}^{\text{asy-in}}_{1,k_0}(\mathbf{r}_0) = \frac{i\kappa}{1-\sigma e^{ik_0L}} \frac{\mathbf{d}(\mathbf{r}_{0_\perp})}{\sqrt{2\pi}} e^{ik_0\zeta_0}, \tag{6.17}$$

$$\mathbf{D}^{\text{asy-in}}_{2,k_0}(\mathbf{r}_0) = \frac{i\kappa}{1-\sigma e^{ik_0L}} \frac{\mathbf{d}(\mathbf{r}_{0_\perp})}{\sqrt{2\pi}} e^{ik_0(L-\zeta_0)}, \tag{6.18}$$

where κ and σ are the cross- and self-coupling coefficients of the directional coupler connecting the ring to the bus waveguide.

According to Eq. (6.8) and assuming that the dipole is aligned with the field, the emission rate into each port of the bus waveguide is [148]

$$\Gamma_{1,\text{ring}} = \Gamma_{2,\text{ring}} = \left|\frac{\kappa}{1-\sigma e^{ik_0L}}\right|^2 \frac{p^2\omega_0}{2\varepsilon_0 n^2(\mathbf{r}_0)\hbar v_g} \frac{|\mathbf{d}(\mathbf{r}_{0_\perp})|^2}{\varepsilon_0 n^2(\mathbf{r}_0)}, \tag{6.19}$$

and the total emission rate to the bus waveguide is then

$$\Gamma_{\text{ring}} = \left|\frac{\kappa}{1-\sigma e^{ik_0L}}\right|^2 \Gamma_{\text{wg}}. \tag{6.20}$$

Here, we distinguish two contributions to the rate enhancement: the transverse confinement due to the waveguides and an additional longitudinal (and temporal) confinement introduced by the ring. The latter increases the generation rate by a factor $\left|\frac{\kappa}{1-\sigma e^{ik_0L}}\right|^2$, equal to the field enhancement of the resonator.

It is instructive to express this factor in terms of the quality factor of a resonance aligned to the emitter. In the high-finesse limit ($\sigma \approx 1$), the quality factor can be written as

$$Q = \frac{\omega_0 L}{2v_g}\frac{1}{1-\sigma}. \tag{6.21}$$

Near resonance ($e^{ik_0L} \approx 1$), we can approximate

$$\left|\frac{\kappa}{1-\sigma e^{ik_0L}}\right|^2 \approx \frac{2}{1-\sigma} = \frac{4v_gQ}{\omega_0 L}. \tag{6.22}$$

Consequently, Eq. (6.19) reduces to [148]

$$\Gamma_{\text{ring}}(\sigma \approx 1) = \frac{1}{2}\frac{3}{2\pi^2}\left(\frac{\lambda_0}{n}\right)^3 \frac{Q}{LA_{\text{eff}}(\mathbf{r}_0)}\Gamma_0. \tag{6.23}$$

By defining the effective mode volume $V_{\text{eff}} = A_{\text{eff}}L$, we recover the standard Purcell-enhanced emission rate of Eq. (6.2) for each emission mode of the structure.

6.2.3 Backscattering in Ring Resonators

The asymptotic field formalism not only rigorously reproduces the conventional Purcell result but also extends beyond it to capture non-idealities that arise in realistic integrated structures. Unlike the standard cavity theory, which assumes resonances with a Lorentzian lineshape, Eq. (6.20) remains valid for resonances that are non-Lorentzian, spectrally distorted, or detuned from the emitter's frequency. Moreover, this formalism can capture non-resonant contributions and interference effects that arise in more complex integrated structures. As an example, we now study the effects of backscattering in the ring resonator. Backscattering can arise from various imperfections in the ring, such as edge roughness [9, 130], fabrication defects [165], or even the dipole itself [166]. Here, we model backscattering as originating from a single localized scatterer located at position l_1 along the ring circumference, as illustrated in Fig. 6.3. The scatterer is characterized by a real reflection coefficient ρ and a transmission coefficient $\tau = \sqrt{1-\rho^2}$, where $|\rho|^2$ represents the probability of backscattering per round trip.

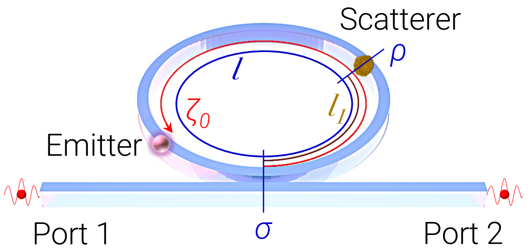

Figure 6.3: Sketch of a dipole embedded in a ring resonator with backscattering. Image taken from [148].

Unlike the simpler case discussed earlier, the clockwise and counterclockwise modes are now coupled through the scatterer. As a result, within the ring resonator, the asymptotic fields for the left and right ports are general superpositions of counter-propagating modes. Following the scattering matrix approach, we can write the asymptotic-in fields at the dipole position as

$$\mathbf{D}^{\text{asy-in}}_{j,k_0}(\mathbf{r}_0) = f^{(j)}_{k_0}(\zeta_0)\frac{\mathbf{d}(\mathbf{r}_{0_\perp})}{\sqrt{2\pi}},$$

where $j = 1, 2$ denotes the port, and $f_{k_0}^{(j)}(\zeta_0)$ describes the field enhancement at the dipole location, accounting for interference between clockwise and counterclockwise modes.

To derive these field enhancements, we consider the scatterer as a beam splitter with transmission amplitude τ and reflection amplitude $i\rho$. The scatterer couples the counterclockwise field propagating from the coupling point to the clockwise field, and vice versa. Following the scattering-matrix treatment of backscattering from Chapter 4, we obtain

$$f_{k_0}^{(1)}(\zeta_0) = \frac{i\kappa}{1-\sigma e^{ik_0L}}\left[\tau e^{ik_0\zeta_0} + i\rho\sigma e^{ik_0(2\zeta_1-\zeta_0)}\frac{e^{ik_0L}}{1-\sigma e^{ik_0L}}\right], \tag{6.24}$$

$$f_{k_0}^{(2)}(\zeta_0) = \frac{i\kappa}{1-\sigma e^{ik_0L}}\left[\tau e^{ik_0(L-\zeta_0)} + i\rho e^{ik_0(\zeta_0-2\zeta_1)}\frac{1}{1-\sigma e^{ik_0L}}\right]. \tag{6.25}$$

These expressions can be simplified by introducing the phase mismatch $\Delta = k_0(\zeta_0-\zeta_1)$, which represents the phase difference due to the separation between the dipole and the scatterer. After some algebra, we find [148]

$$f_{k_0}^{(1)}(\zeta_0) = \frac{i\kappa e^{ik_0\zeta_0}}{(1-\sigma e^{ik_0L})(1-i\rho e^{-2i\Delta})}\left[\tau - \tau\sigma e^{ik_0L} + \sigma^2 e^{ik_0L}(1-i\rho e^{-2i\Delta})\right], \tag{6.26}$$

$$f_{k_0}^{(2)}(\zeta_0) = \frac{i\kappa e^{ik_0(L-\zeta_0)}}{(1-\sigma e^{ik_0L})(1-i\rho e^{-2i\Delta})}\left[\tau - \tau\sigma e^{ik_0L} + e^{ik_0L}(1-i\rho e^{-2i\Delta})\right]. \tag{6.27}$$

From these expressions and Eq. (6.8), the emission rate into each port of the bus waveguide is [148]

$$\Gamma_{j,\mathrm{rb}} = \frac{p^2\omega_0}{2\varepsilon_0 n^2(\mathbf{r}_0)\hbar v_g}\frac{|\mathbf{d}(\mathbf{r}_{0_\perp})|^2}{\varepsilon_0 n^2(\mathbf{r}_0)}\left|f_{k_0}^{(j)}(\zeta_0)\right|^2, \tag{6.28}$$

and the total emission rate is

$$\Gamma_{\mathrm{rb}} = \Gamma_{1,\mathrm{rb}} + \Gamma_{2,\mathrm{rb}} = \frac{\Gamma_{\mathrm{wg}}}{2}\left(\left|f_{k_0}^{(1)}(\zeta_0)\right|^2 + \left|f_{k_0}^{(2)}(\zeta_0)\right|^2\right). \tag{6.29}$$

The parameter Δ determines both the total emission rate and the distribution of emitted photons between the two ports of the structure. When backscattering arises from random inhomogeneities in the fabrication process, Δ cannot be controlled. However, one can envision using nanofabrication to introduce intentionally designed reflectors in specific regions of the resonator structure [167]. In such cases, it becomes possible, in principle, to have some control over the emission properties.

It is useful to consider the case in which the dipole is resonantly coupled to the ring, when $k_0L = 2m\pi$ with $m \in \mathbb{N}$. In this case, the expressions simplify considerably, and the total emission rate becomes [148]

$$\Gamma_{\mathrm{rb}} = \Gamma_{\mathrm{wg}}\frac{\kappa^2}{(\rho^2+(\tau-\sigma)^2)^2}\left[(1+\sigma^2-2\tau\sigma)(1-\rho\sin 2\Delta) + \kappa^4\tau^2\right]. \tag{6.30}$$

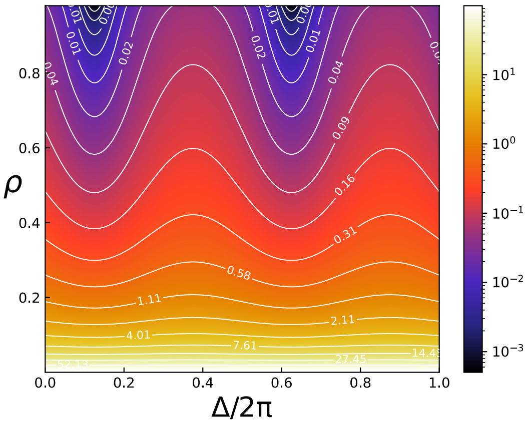

Figure 6.4: Emission rate in a ring resonator with backscattering as a function of the dephasing Δ between the dipole and the scatterer, and the scattering probability ρ. Image taken from [148].

The presence of backscattering dramatically impacts the emission rate, causing variations of several orders of magnitude depending on the relative positions of the dipole and the backscattering element, as shown in Fig. 6.4. This significant change in emission arises from the onset of standing waves within the resonator, resulting from the coupling of clockwise and counterclockwise propagating modes. Consequently, emission is either strongly enhanced or suppressed based on whether the dipole is located at a maximum or a node of these standing waves. This finding is coherent with the result by Dignam et. al. [168], who showed that in the presence of interference, the emission of a properly positioned emitter can be efficiently suppressed. Notably, emission can be entirely suppressed when $\Delta = \pi/4 + n\pi$, where $n \in \mathbb{N}$. As expected, when $\rho \to 0$, one retrieves the result for the backscattering-free ring discussed in the previous section.

Unlike the case with no backscattering, in general, the emission rates $\Gamma_{\text{rb},1}$ and $\Gamma_{\text{rb},2}$ from the left and right ports are different. These quantities, normalized to the emission rate in a simple waveguide, can be written as [148]

$$\frac{\Gamma_{\text{rb},1}}{\Gamma_{\text{wg}}} = \frac{\kappa^2}{2(\rho^2 + (\tau - \sigma)^2)^2} \left[(2\sigma(\sigma - \tau))(1 - \rho \sin 2\Delta) + \kappa^4 \tau^2\right], \tag{6.31}$$

$$\frac{\Gamma_{\text{rb},2}}{\Gamma_{\text{wg}}} = \frac{\kappa^2}{2(\rho^2 + (\tau - \sigma)^2)^2} \left[(2(1 - \tau\sigma))(1 - \rho \sin 2\Delta) - \kappa^4 \tau^2\right]. \tag{6.32}$$

In Fig. 6.5, we show the normalized dipole emission rate $\Gamma_{\text{rb}}/\Gamma_{\text{wg}}$ alongside the probabilities $P_j = \Gamma_{\text{rb},j}/\Gamma_{\text{rb}}$ of the photon exiting the left or right port of the structure as functions of the backscattering phase Δ. We consider a point dipole emitting at $\lambda_0 = 630$ nm, a ring of length $L = 300\pi\lambda_0 = 93.7$ µm, self-coupling parameter $\sigma = 0.98$, and reflectivity $\rho = 17 \times 10^{-3}$. It is evident that, even for a small backscattering probability per round trip,

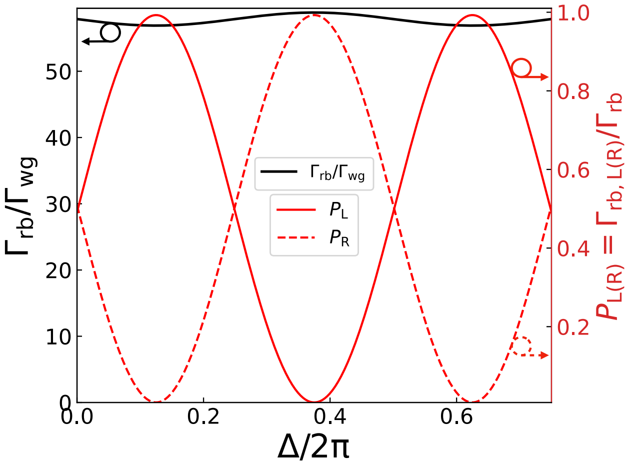

Figure 6.5: Black solid line (left): total emission rate. Red solid line (right): probability of emission from the left port. Red dashed line (right): probability of emission from the right port. The simulation parameters are emission wavelength $\lambda_0 = 630$ nm, ring length $L = 300\pi\lambda_0 = 93.7$ μm, self-coupling parameter $\sigma = 0.98$, and reflectivity $\rho = 17 \times 10^{-3}$. Image taken from [148].

where the overall dipole emission rate remains essentially independent of Δ, the presence of backscattering still significantly impacts the spatial distribution of the emitted light.

Due to the resonant field enhancement within the cavity, even a moderate backscattering can produce a significant modification of both the emission rate and the directional distribution of the emitted light. Therefore, such an effect must be carefully considered in the design and fabrication of single-photon sources based on dipole emission. On the other hand, the presence of two counter-propagating modes offers a new degree of freedom that might be harnessed to enhance the selectivity of the emission mode. In the following section, we will build on this finding to design and analyze a resonant interferometric coupler for deterministic single-photon generation in a specific output mode.

6.3 Tuning Emission Properties via a Sagnac Interferometric Coupler

As illustrated in Fig. 6.6, our designed system consists of a photonic molecule formed by an auxiliary ring (Aux) of radius R_a and a main ring (Main) resonator of radius R_m coupled to an integrated Sagnac interferometer of length l_s with a $50:50$ beam splitter at the output. The Main resonator hosts a single-photon emitter resonantly coupled to the Main ring and operating at the wavelength λ_0. We assume that the resonant frequencies of the resonators, as well as the interference at the output of the Sagnac interferometer, can be controlled using phase shifters, such as heaters or electro-optic modulators,

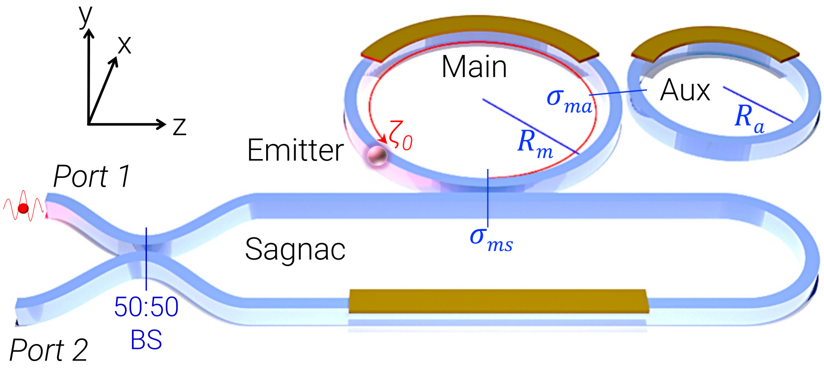

Figure 6.6: Sketch of a Sagac interferometric coupler. Image taken from [148].

depending on the material platform employed.

The Main ring is characterized by the coupling coefficient σ_{ms} to the Sagnac interferometer and σ_{ma} to the Aux ring, with corresponding cross-coupling coefficients $\kappa_{\mathrm{ms}} = \sqrt{1-\sigma_{\mathrm{ms}}^2}$ and $\kappa_{\mathrm{ma}} = \sqrt{1-\sigma_{\mathrm{ma}}^2}$. The Sagnac beam splitter has $\sigma_s = \kappa_s = 1/\sqrt{2}$.

At the dipole position $\mathbf{r}_0 = (\mathbf{r}_{0_\perp}, \zeta_0)$ within the Main ring, the asymptotic-in fields can be written as $\mathbf{D}^{\text{asy-in}}_{j,k_0}(\mathbf{r}_0) = f^{(j)}_{k_0}(\zeta_0)\frac{\mathbf{d}(\mathbf{r}_{0_\perp})}{\sqrt{2\pi}}$, where $j=1,2$ denotes the output port. Due to the presence of the Sagnac interferometer, regardless of which port the photon exits, the dipole always experiences a superposition of clockwise and counterclockwise fields. The field enhancements $f^{(j)}_{k_0}(\zeta_0)$ can be derived by solving the complete scattering problem. After defining the phase shifts per round trip in the Main and Aux rings as $\delta_m = k_0 L_m = 2\pi k_0 R_m$ and $\delta_a = k_0 L_a = 2\pi k_0 R_a$, and introducing the Sagnac phase shift $\delta_s = k_0 l_s$, we find [148]

$$f^{(1)}_{k_0}(\zeta_0) = \frac{\kappa_{\mathrm{ms}}}{\mathscr{D}}\left[-i\sigma_s C(\sigma_{\mathrm{ma}},\delta_a)e^{i(\delta_m+\delta_s)/2}e^{ik_0\zeta_0} - \kappa_s C^*(\sigma_{\mathrm{ma}},\delta_a)e^{-i(\delta_m-\delta_s)/2}e^{-ik_0\zeta_0}\right] \tag{6.33}$$

$$f^{(2)}_{k_0}(\zeta_0) = \frac{\kappa_{\mathrm{ms}}}{\mathscr{D}}\left[\kappa_s C(\sigma_{\mathrm{ma}},\delta_a)e^{i(\delta_m+\delta_s)/2}e^{ik_0\zeta_0} + i\sigma_s C^*(\sigma_{\mathrm{ma}},\delta_a)e^{-i(\delta_m-\delta_s)/2}e^{-ik_0\zeta_0}\right], \tag{6.34}$$

where we have defined

$$\mathscr{D} = 1 - \sigma_{\mathrm{ms}} C(\sigma_{\mathrm{ma}},\delta_a)e^{i\delta_m}, \tag{6.35}$$

and introduced the function

$$C(\sigma_{\mathrm{ma}},\delta_a) = \frac{1-\sigma_{\mathrm{ma}}e^{-i\delta_a}}{1-\sigma_{\mathrm{ma}}e^{i\delta_a}}. \tag{6.36}$$

From Eq. (6.9), the total emission rate is

$$\Gamma_{\mathrm{T}} = \frac{\Gamma_{\mathrm{wg}}}{2}\left(\left|f^{(1)}_{k_0}(\zeta_0)\right|^2 + \left|f^{(2)}_{k_0}(\zeta_0)\right|^2\right). \tag{6.37}$$

After some algebra, this can be written as

$$\Gamma_{\mathrm{T}} = \Gamma_{\mathrm{wg}} \frac{\kappa_{\mathrm{ms}}^2}{1 + \sigma_{\mathrm{ms}}^2 + \sigma_{\mathrm{ms}} \left[C(\sigma_{\mathrm{ma}}, \delta_a) e^{i\delta_m} + \mathrm{c.c.} \right]}. \tag{6.38}$$

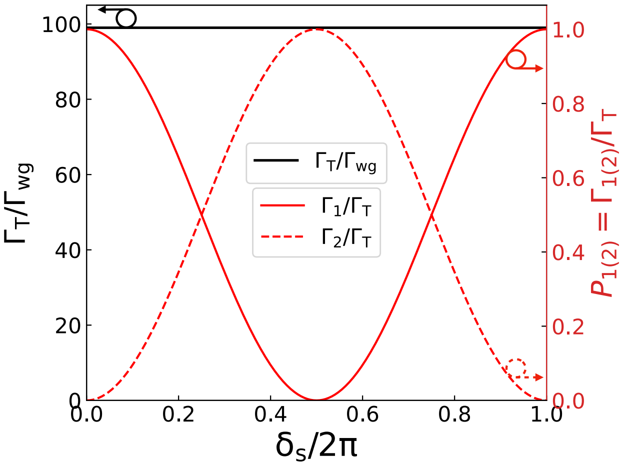

Figure 6.7: Black solid line (left): total emission rate. Red solid line (right): probability of emission from Port 1. Red dashed line (right): probability of emission from the right Port 2. Image taken from [148].

A remarkable feature of this expression is that the total emission rate Γ_{T} is independent of both the dipole position ζ_0 within the ring and the Sagnac phase shift δ_s. This independence arises from the symmetric coupling of the clockwise and counterclockwise modes through the Sagnac interferometer. The total rate depends only on the coupling strengths and the phase detunings of the Main and Aux rings. In the limit $\sigma_{\mathrm{ma}} \to 1$, where the Aux ring is effectively decoupled, Eq. (6.38) reduces to the single-ring result of Eq. (6.20).

The Sagnac interferometer enables control over the interference between emission into the clockwise and counterclockwise modes. As a result, the emitted photon is generally distributed unequally between Port 1 and Port 2. The probability of emission from the j-th port is given by [148]

$$P_j = \frac{\Gamma_j}{\Gamma_{\mathrm{T}}} = \frac{1}{2} \left[1 - \frac{(-1)^{j+1}}{2} \left(C(\sigma_{\mathrm{ma}}, \delta_a) e^{i(\delta_m + \delta_s + 2k_0\zeta_0)} - \mathrm{c.c.} \right) \right], \tag{6.39}$$

where $\Gamma_j = \Gamma_{\mathrm{wg}} |f_{k_0}^{(j)}(\zeta_0)|^2/2$ is the emission rate into the j-th port.

This expression reveals that the output distribution can be engineered by tuning structural parameters and phase shifts, enabling control over the emission intensity and directionality. In Fig. 6.7, we show the normalized dipole emission rate $\Gamma_{\mathrm{T}}/\Gamma_{\mathrm{wg}}$ and the normalized output probabilities P_j as functions of the Sagnac phase shift δ_s. We consider parameters $\lambda_0 = 630$ nm, $R_m = 158\lambda_0$, $R_a = R_m/2$, which yield $\delta_m = \delta_a = 2\pi$ and resonant operation. The self-coupling parameters are set as $\sigma_s = 1/\sqrt{2}$, $\sigma_{\mathrm{ms}} = 0.98$, and $\sigma_{\mathrm{ma}} = 0.7$.

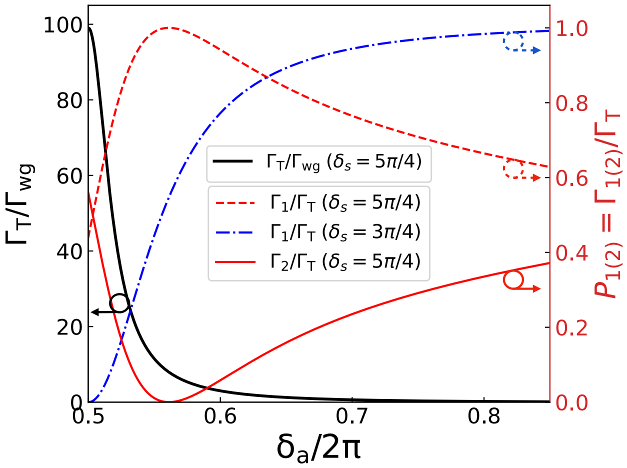

Figure 6.8: Effects of the Aux resonator dephasing δ_a. Black solid line (left): total emission rate. Red solid line (right): probability of emission from Port 1 when $\delta_s = 5\pi/4$. Red dashed line (right): probability of emission from Port 2 when $\delta_s = 5\pi/4$. Blue dashed-dotted line (right): probability of emission from Port 1 when $\delta_s = 3\pi/4$. Image taken from [148].

Assuming a Main ring radius of $R_m = 100\ \mu$m and an intrinsic quality factor $Q = 10^5$ limited only by propagation losses, the structure achieves an extraction efficiency of approximately 99%, as indicated by the nearly constant value of $\Gamma_T/\Gamma_{wg} \approx 100$. This high efficiency, maintained across all values of δ_s, reflects the strong enhancement of spontaneous emission, about two orders of magnitude greater than that of a simple waveguide, ensuring that the dipole primarily emits into the guided mode of the Main ring.

The Sagnac phase shift δ_s plays a crucial role in determining the photon's emission direction. When $\delta_s = 0$ or $\delta_s = 2\pi$, the photon always exits from Port 1, whereas for $\delta_s = \pi$, it exits from Port 2. By continuously tuning δ_s, it is possible to generate any coherent superposition of the photon exiting from the two ports. This tunability allows full control over the photon's path degree of freedom, without requiring knowledge of the dipole's precise longitudinal position within the ring.

Finally, we discuss how this structure can be used to control both the dipole emission rate and the output probability at each port by tuning the Aux ring phase shift δ_a. As illustrated in Fig. 6.8, by adjusting δ_a, one can selectively enhance or suppress the dipole's emission rate. This effect stems from the strong coupling between the Main and Aux resonators, which shifts the resonance frequency of the Main ring and thereby controls the dipole-mode interaction strength. When the coupling is strong and induces a full splitting of the Main resonance, the dipole becomes off-resonant with both hybrid modes, leading to a suppression of spontaneous emission. Conversely, when the Aux ring is far-detuned and effectively uncoupled, the dipole remains resonant with the Main ring, resulting in efficient photon emission.

The presence of the Aux resonator influences both the emission rate and the quantum state of the emitted photons, which, in the path degree of freedom, is determined by the probability of exiting from one of the two ports of the structure. By adjusting both the values of δ_a and δ_s, one can achieve the simultaneous control of the emission rate and the emission path. For example, by fixing $\delta_s = 5\pi/4$, the probability of having a superposition state of photons emitted is close to one and can be controlled by varying δ_a, while simultaneously suppressing the dipole emission. For $\delta_s = 3\pi/4$, the dipole emission is still suppressed by adjusting δ_a, while the photon emission probability from Port 1 is enhanced until it reaches unity.

6.4 Conclusion

In this final chapter, we introduced a second resonant interferometric coupler architecture based on a Sagnac interferometer. While the Mach-Zehnder resonant interferometric coupler, introduced in Chapter 3 and further analyzed in Chapter 5, was designed to selectively control resonance quality factors for squeezed light generation and bound states in the continuum, this chapter focused on a fundamentally different application: controlling spontaneous single-photon emission from a dipole embedded in a resonator. Here, we addressed the challenge of tailoring the emission direction and rate of the generated state. This was achieved by combining a ring resonator, providing the necessary field enhancement, with a Sagnac interferometer creating an interaction between counterpropagating modes.

We began by reviewing the principles of dipole emission in waveguides and ring resonators. Building on the asymptotic-fields formalism from Chapter 2, we not only recovered the well-known Purcell effect but also clarified the role of backscattering in modifying the generation rates.

We then extended our analysis to describe dipole emission in a ring resonator coupled to a Sagnac interferometer. We demonstrated how the Sagnac loop can enhance or suppress emission into desired channels, providing a versatile platform for engineering single-photon sources with tailored properties. An auxiliary resonator was then used to shift the resonances of the main ring and increase the control on the generation rate.

This work highlights the broad potential of resonant interferometric coupling strategies in quantum photonics, showcasing how different resonator architectures can address a variety of challenges in quantum light generation and manipulation.

Conclusions

In this thesis, we presented a theoretical framework for the design and modeling of integrated silicon nitride photonic circuits, with a focus on interferometric couplers as a tool to control the generation of nonclassical light in ring resonators. The work addressed two primary objectives: the generation of squeezed states and heralded single photons via spontaneous four-wave mixing, and the enhancement of single-photon emission from dipoles embedded in resonators.

We began by establishing a scattering matrix formalism to describe the classical properties of integrated photonic circuits, analyzing fundamental building blocks such as ring resonators, Mach-Zehnder interferometers, and Sagnac interferometers. The quantization of the electromagnetic field in nonlinear media was then examined, providing the necessary foundation to model quantum light generation in these systems.

Three complementary methods were presented to calculate squeezing levels, generation rates, and spectral correlations of the squeezed state produced by spontaneous four-wave mixing. After reviewing a Lorentzian treatment of ring resonances, ideal for high-gain nonlinear processes in high-finesse systems, and an Asymptotic-field decomposition, separating linear and nonlinear responses to yield analytical results in the low-gain regime even for split or noisy resonances, we developed a *local-fields method*. In this latter approach, we combined the advantages of the Lorentzian and Asymptotic methods, by decomposing the asymptotic fields describing each resonance into a spatially restricted local basis. In this framework, it was possible to improve the numerical accuracy in solving the system's equations of motion, enabling precise characterization of squeezing processes.

With these theoretical tools in hand, we addressed squeezing optimization by introducing a *Mach-Zehnder resonant interferometric coupler*, an architecture integrating two ring resonators and an Mach-Zehnder Interferometer to selectively control the quality factor of the device's resonances. In the low-gain regime, this selectivity allowed spectral tuning of heralded single photons, achieving purities up to 98.67%. In the high-gain regime, parasitic processes that would degrade the squeezing level were suppressed by splitting specific resonances, yielding highly squeezed states approaching 6.49 dB. Both these results surpass the fundamental limits of single-ring resonators.

Platform optimization was subsequently addressed, with a focus on heralded single-photon generation. Finite-difference time-domain simulations guided the choice of the optimal waveguide geometry, accounting for dispersion engineering, loss mitigation, and sidewall roughness effects. A systematic design methodology was developed to balance performance metrics such as nonlinearity, escape efficiency, and final generation rate, with fabrication constraints, providing a practical pathway for quantum light source implementation.

Beyond squeezed light generation, we adapted the Mach-Zehnder resonant interferometric coupler architecture to investigate bound states in the continuum. By tuning the coupler to uncouple one resonance while maintaining the others in the overcoupled regime, we demonstrated the feasibility of creating a bound state in this structure. This can be investigated through a spontaneous four-wave mixing experiment in which the idler is in the bound mode. We extended the asymptotic-field formalism to include non-radiative modes, allowing us to calculate the generation rate when the idler mode fell into a BIC. We showed that this rate matched the limit derived for radiative asymptotic fields in the absence of losses, confirming the robustness of the approach.

Shifting to single-photon emission from a dipole, we apply the asymptotic-field framework to move beyond conventional cavity QED treatments. Fabrication non-idealities, such as losses and backscattering, were incorporated naturally in our Fermi-golden-rule treatment. For greater tunability, we proposed the *Sagnac resonant interferometric coupler*, relying on the interference between clockwise and counterclockwise field in a Sagnac loop, to select the emission mode of the single photon. The addition of an auxiliary resonator further allowed tuning of the rates.

Together, these studies highlighted the versatility of interferometric couplers in tailoring light-matter interactions for quantum applications. By bridging theoretical modeling, numerical simulation, and device engineering, this we worked toward scalable, high-purity quantum light generation in integrated photonics.

Acknowledgments

First and foremost, I wish to thank my family and friends. Their unwavering support and sacrifices have been essential for completing this thesis. The closer they are to me, the more they have endured, and for that, I am deeply grateful.

I acknowledge my supervisor, Marco Liscidini, for his presence and the wealth of ideas that constantly pushed our research. His ability to create opportunities for national and international collaboration generated some of the richest experiences in my life.

Along with him, I want to mention all the members of our group in Pavia: Alessia Stefano, Diego Maragnano, Luca Zatti, Francesco Malaspina, Amideddin Mataji Kojouri, Tommaso Perani, Vincenzo Macrì, and Matteo Piccolini. In particular, the mutual support with Diego, Alessia, and Luca was invaluable throughout my academic experience. Luca was the first to work on the squeezing and platform optimization calculations and supported me in taking these works forward. The sharp insights and coding skills of Francesco were crucial in understanding many features of the Mach-Zehnder resonant interferometric coupler. Vincenzo brought his expertise in spontaneous emission and how to extend the tools we knew in that realm.

I am deeply grateful to Michael Sloan and John Sipe from the University of Toronto for their work on modelling high-gain squeezing through the local modes, in which I had the honour to collaborate. Thanks also to the other members of the group: Christian Drago, Colin Vendromin, Samuel Fontaine, Milica Banic, Jasper Kranias, Amirali Atrli, Alistair Duff, and Jason Kattan.

My sincere thanks go to Xanadu Quantum Technology for providing the samples of the Mach-Zehnder resonant interferometric coupler, their proprietary Python package for calculating squeezing levels, and the many insightful discussions that enriched our understanding of the main topics explored in this thesis.

I would like to acknowledge Paula Pagano, Massimo Borghi, and Federica Moroni for their experimental work and feedback, which were essential in understanding the potential and limitations of the Mach-Zehnder resonant interferometric coupler.

I am grateful to Professors Marc Dignam and Costantino De Angelis for their careful review of this thesis and their thoughtful suggestions.

Besides my group, many professors and students at the University of Pavia provided invaluable help and feedback on this thesis: Davide Rinaldi, Emanuele

Tumbiolo, Giuseppe Conte, Antonio Mazzarone, Gaia Candreva, Federica De Domenico, Luigi Frau, Lorenzo Marti, Noemi Tagliavacche, Giuliano Coppola, Dario Tona, Annalara Ferrara, Prof. Daniela Rebuzzi, Prof. Lucio Claudio Andreani, and Prof. Claudio Dappiaggi.

Finally, since I lived and worked for three months in Toronto while completing my Ph. D., I want to acknowledge the land on which that city was built. For thousands of years it has been the traditional territory of the Wendat, the Seneca, the Anishnaabeg, the Haudenosaunee, and most recently, the Mississauga, and the Métis. These Nations have inhabited and cared for the land and never ceeded it until today. Many diverse Indigenous and Settler peoples have taken their home in this territory in recent years, and they have been invited into the "Dish With One Spoon" treaty, binding to share and protect the land in the spirit of peace, friendship, and respect. I am grateful for the opportunity to have been a guest on this land.

Bibliography

[1] Stewart E. Miller. “Integrated Optics: An Introduction”. In: *Bell System Technical Journal* 48.7 (1969), pp. 2059–2069. DOI: `https://doi.org/10.1002/j.1538-7305.1969.tb01165.x`.

[2] Nicholas C. Harris et al. “Large-scale quantum photonic circuits in silicon”. In: *Nanophotonics* 5.3 (2016), pp. 456–468. DOI: `doi:10.1515/nanoph-2015-0146`.

[3] Chao Xiang, Warren Jin, and John E. Bowers. “Silicon nitride passive and active photonic integrated circuits: trends and prospects”. In: *Photon. Res.* 10.6 (June 2022), A82–A96. DOI: `10.1364/PRJ.452936`.

[4] Ken-Ichi Sato et al. “Prospects and challenges of optical switching technologies for intra data center networks”. In: *J. Opt. Commun. Netw.* 14.11 (Nov. 2022), pp. 903–915. DOI: `10.1364/JOCN.467726`.

[5] Lanxuan Zhang et al. “Investigation and demonstration of a high-power handling and large-range steering optical phased array chip”. In: *Opt. Express* 29.19 (Sept. 2021), pp. 29755–29765. DOI: `10.1364/OE.434067`.

[6] W. Bogaerts et al. “Programmable photonic circuits”. In: *Nature* 586 (2020), pp. 207–216. DOI: `https://doi.org/10.1038/s41586-020-2764-0`.

[7] E. Pelucchi et al. “The potential and global outlook of integrated photonics for quantum technologies.” In: *Nat Rev Phys* 4 (2022), pp. 194–208. DOI: `https://doi.org/10.1038/s42254-021-00398-z`.

[8] W. Luo et al. “Recent progress in quantum photonic chips for quantum communication and internet.” In: *Light Sci Appl* 12 (2023), p. 175. DOI: `https://doi.org/10.1038/s41377-023-01173-8`.

[9] W. Bogaerts et al. “Silicon microring resonators”. In: *Laser & Photonics Reviews* 6.1 (2012), pp. 47–73. DOI: `https://doi.org/10.1002/lpor.201100017`.

[10] Andrea Melloni et al. “Ring-resonator filters in silicon oxynitride technology for dense wavelength-division multiplexing systems”. In: *Opt. Lett.* 28.17 (Sept. 2003), pp. 1567–1569. DOI: `10.1364/OL.28.001567`.

[11] M. Sumetsky. "Optimization of optical ring resonator devices for sensing applications". In: *Opt. Lett.* 32.17 (Sept. 2007), pp. 2577–2579. DOI: `10.1364/OL.32.002577`.

[12] Sasikanth Manipatruni et al. "Ultra-low voltage, ultra-small mode volume silicon microring modulator". In: *Opt. Express* 18.17 (Aug. 2010), pp. 18235–18242. DOI: `10.1364/OE.18.018235`.

[13] J. Silverstone et al. "Qubit entanglement between ring-resonator photon-pair sources on a silicon chip." In: *Nat Commun* 6 (2015), p. 7948. DOI: `https://doi.org/10.1038/ncomms8948`.

[14] Davide Grassani et al. "Micrometer-scale integrated silicon source of time-energy entangled photons". In: *Optica* 2.2 (Feb. 2015), pp. 88–94. DOI: `10.1364/OPTICA.2.000088`.

[15] Z. Lu et al. "High-performance silicon photonic tri-state switch based on balanced nested Mach-Zehnder interferometer." In: *Sci Rep* 7 (2017), p. 12244. DOI: `https://doi.org/10.1038/s41598-017-12455-8`.

[16] Md Samiul Alam et al. "Net 220 Gbps/λ IM/DD Transmssion in O-Band and C-Band With Silicon Photonic Traveling-Wave MZM". In: *Journal of Lightwave Technology* 39.13 (2021), pp. 4270–4278. DOI: `10.1109/JLT.2021.3074096`.

[17] Abu Naim R. Ahmed et al. "High-efficiency lithium niobate modulator for K band operation". In: *APL Photonics* 5.9 (Sept. 2020), p. 091302. ISSN: 2378-0967. DOI: `10.1063/5.0020040`.

[18] Folkert Horst et al. "Cascaded Mach-Zehnder wavelength filters in silicon photonics for low loss and flat pass-band WDM (de-)multiplexing". In: *Opt. Express* 21.10 (May 2013), pp. 11652–11658. DOI: `10.1364/OE.21.011652`.

[19] Matteo Cherchi. "Design scheme for Mach-Zehnder interferometric coarse wavelength division multiplexing splitters and combiners". In: *J. Opt. Soc. Am. B* 23.9 (Sept. 2006), pp. 1752–1756. DOI: `10.1364/JOSAB.23.001752`.

[20] Michael Reck et al. "Experimental realization of any discrete unitary operator". In: *Phys. Rev. Lett.* 73 (1 July 1994), pp. 58–61. DOI: `10.1103/PhysRevLett.73.58`.

[21] William R. Clements et al. "Optimal design for universal multiport interferometers". In: *Optica* 3.12 (Dec. 2016), pp. 1460–1465. DOI: `10.1364/OPTICA.3.001460`.

[22] Jianwei Wang et al. "Multidimensional quantum entanglement with large-scale integrated optics". In: *Science* 360.6386 (2018), pp. 285–291. DOI: `10.1126/science.aar7053`.

[23] B Culshaw. "The optical fibre Sagnac interferometer: an overview of its principles and applications". In: *Measurement Science and Technology* 17.1 (Nov. 2005), R1. DOI: `10.1088/0957-0233/17/1/R01`. URL: `https://dx.doi.org/10.1088/0957-0233/17/1/R01`.

[24] Hamed Arianfard et al. "Sagnac interference in integrated photonics". In: *Applied Physics Reviews* 10.1 (Feb. 2023), p. 011309. DOI: `10.1063/5.0123236`.

[25] Matthias Fink et al. "Entanglement-enhanced optical gyroscope". In: *New Journal of Physics* 21.5 (May 2019), p. 053010. DOI: `10.1088/1367-2630/ab1bb2`. URL: `https://dx.doi.org/10.1088/1367-2630/ab1bb2`.

[26] Z. Zhu et al. "Sagnac interference in integrated photonics". In: *Nanophotonics* 12.15 (2023), pp. 2695–2718. DOI: `10.1515/nanoph-2023-0301`.

[27] Y. Xu, J. Liu, et al. "Quantum-enhanced Sagnac gyroscopes on integrated photonic platforms". In: *Phys. Rev. Applied* 21.2 (2024), p. 024011. DOI: `10.1103/PhysRevApplied.21.024011`.

[28] J.-P. Chen et al. "Twin-field quantum key distribution with a Sagnac loop". In: *Nature Photonics* 16 (2022), pp. 803–810. DOI: `10.1038/s41566-022-00995-2`.

[29] A. Fedrizzi et al. "A wavelength-tunable fiber-coupled source of narrowband entangled photons". In: *Optics Express* 15.23 (2007), pp. 15377–15386. DOI: `10.1364/OE.15.015377`.

[30] P. Vergyris, R. Ramirez-Alarcon, et al. "High-brightness entangled photon source based on a Sagnac interferometer". In: *Optics Letters* 45.5 (2020), pp. 1273–1276. DOI: `10.1364/OL.389020`.

[31] Y. Ruan, L. Wang, et al. "Integrated Sagnac loop reflectors for photonic circuits". In: *Optics Express* 30.13 (2022), pp. 23219–23230. DOI: `10.1364/OE.455629`.

[32] Leonard Mandel and Emil Wolf. *Optical Coherence and Quantum Optics*. Cambridge, UK: Cambridge University Press, 1995.

[33] Michael G. Raymer. "Quantum theory of light in a dispersive structured linear dielectric: a macroscopic Hamiltonian tutorial treatment". In: *Journal of Modern Optics* 67.3 (2020), pp. 196–212.

[34] Mark Hillery and Leonard Mlodinow. "Quantized fields in a nonlinear dielectric medium: a microscopic approach". In: *Physical Review A* 55.1 (1997), pp. 678–689.

[35] Nicolás Quesada and John E. Sipe. "Why you should not use the electric field to quantize in nonlinear optics". In: *Optics Letters* 42.17 (2017), pp. 3443–3446.

[36] Max Born and Leopold Infeld. “On the quantization of the new field equations I”. In: *Proceedings of the Royal Society of London. Series A, Mathematical and Physical Sciences* 147.862 (1934), pp. 522–546.

[37] Mark Hillery and Leonard D. Mlodinow. “Quantization of electrodynamics in nonlinear dielectric media”. In: *Physical Review A* 30.4 (1984), pp. 1860–1865.

[38] Naveen A. R. Bhat and John E. Sipe. “Hamiltonian treatment of the electromagnetic field in dispersive and absorptive structured media”. In: *Physical Review A* 73.6 (2006), p. 063808.

[39] Lukas G. Helt, Marco Liscidini, and John E. Sipe. “How does it scale? Comparing quantum and classical nonlinear optical processes in integrated devices”. In: *J. Opt. Soc. Am. B* 29.8 (Aug. 2012), pp. 2199–2212. DOI: `10.1364/JOSAB.29.002199`.

[40] N. Quesada et al. “Beyond photon pairs—nonlinear quantum photonics in the high-gain regime: a tutorial”. In: *Adv. Opt. Photon.* 14.3 (Sept. 2022), pp. 291–403. DOI: `10.1364/AOP.445496`.

[41] C. C. Gerry and P. L. Knight. *Introductory Quantum Optics*. 2005.

[42] Earle Hesse Kennard. “Zur Quantenmechanik einfacher Bewegungstypen”. In: *Zeitschrift für Physik* 44.4 (1927), pp. 326–352.

[43] Carlton M Caves. “Quantum-mechanical noise in an interferometer”. In: *Physical Review D* 23.8 (1981), pp. 1693–1708.

[44] Ulrik L Andersen et al. “30 years of squeezed light generation”. In: *Physica Scripta* 91.5 (Apr. 2016), p. 053001. DOI: `10.1088/0031-8949/91/5/053001`.

[45] RE Slusher et al. “Observation of squeezed states generated by four-wave mixing in an optical cavity”. In: *Physical Review Letters* 55.22 (1985), pp. 2409–2412.

[46] RM Shelby et al. “Broad-band parametric deamplification of quantum noise in an optical fiber”. In: *Physical Review Letters* 57.6 (1986), pp. 691–694.

[47] Lu-An Wu et al. “Generation of squeezed states by parametric down conversion”. In: *Physical Review Letters* 57.20 (1986), pp. 2520–2523.

[48] Moritz Mehmet et al. “Observation of strong twin-beam intensity correlations in a four-wave mixing scheme with frequency-degenerate pump beams”. In: *Optics Express* 15.22 (2007), pp. 14366–14372.

[49] Avik Dutt et al. “On-chip optical squeezing”. In: *Physical Review Applied* 3.4 (2015), p. 044005.

[50] Takahiro Kashiwazaki et al. “Over-8-dB squeezed light generation by a broadband waveguide optical parametric amplifier toward fault-tolerant ultra-fast quantum computers”. In: *Applied Physics Letters* 122.23 (2023), p. 234003.

[51] Yizhen Zhao et al. "Near-degenerate quadrature-squeezed vacuum generation on a silicon-nitride chip". In: *Physical Review Letters* 124.19 (2020), p. 193601.

[52] Vivek D Vaidya et al. "Broadband quadrature-squeezed vacuum and nonclassical photon number correlations from a nanophotonic device". In: *Science Advances* 6.39 (2020), eaba9186.

[53] Yichen Shen et al. "Strong nanophotonic quantum squeezing exceeding 3.5 dB in a foundry-compatible Kerr microresonator". In: *Optica* 12.3 (Mar. 2025), pp. 302–308. DOI: `10.1364/OPTICA.542968`.

[54] Yue Zhang et al. "Squeezed light from a nanophotonic molecule". In: *Nature Communications* 12.1 (2021), p. 2233.

[55] Junaid Aasi et al. "Enhanced sensitivity of the LIGO gravitational wave detector by using squeezed states of light". In: *Nature Photonics* 7.8 (2013), pp. 613–619.

[56] Giuseppe Marino et al. "Spontaneous photon-pair generation from a dielectric nanoantenna". In: *Optica* 6 (Nov. 2019), pp. 1416–1422. DOI: `10.1364/OPTICA.6.001416`.

[57] Catxere A Casacio et al. "Quantum-enhanced nonlinear microscopy". In: *Nature* 594.7862 (2021), pp. 201–206.

[58] J Eli Bourassa et al. "Blueprint for a scalable photonic fault-tolerant quantum computer". In: *PRX Quantum* 2.3 (2021), p. 030325.

[59] Han-Sen Zhong et al. "Quantum computational advantage using photons". In: *Science* 370.6523 (2020), pp. 1460–1463.

[60] Lars S Madsen et al. "Quantum computational advantage with a programmable photonic processor". In: *Nature* 606.7912 (2022), pp. 75–81.

[61] Peter J. Mosley et al. "Heralded Generation of Ultrafast Single Photons in Pure Quantum States". In: *Phys. Rev. Lett.* 100 (13 Apr. 2008), p. 133601. DOI: `10.1103/PhysRevLett.100.133601`. URL: `https://link.aps.org/doi/10.1103/PhysRevLett.100.133601`.

[62] Hiroo Azuma, William J. Munro, and Kae Nemoto. "Heralded single-photon source based on superpositions of squeezed states". In: *Phys. Rev. A* 109 (5 May 2024), p. 053711. DOI: `10.1103/PhysRevA.109.053711`.

[63] Yi-Ru Chen et al. "Generation of heralded optical cat states by photon addition". In: *Phys. Rev. A* 110 (2 Aug. 2024), p. 023703. DOI: `10.1103/PhysRevA.110.023703`.

[64] M. Dakna et al. "Generating Schrödinger-cat-like states by means of conditional measurements on a beam splitter". In: *Phys. Rev. A* 55 (4 Apr. 1997), pp. 3184–3194. DOI: `10.1103/PhysRevA.55.3184`. URL: `https://link.aps.org/doi/10.1103/PhysRevA.55.3184`.

[65] Daniel J. Weigand and Barbara M. Terhal. “Generating grid states from Schrödinger-cat states without postselection”. In: *Phys. Rev. A* 97 (2 Feb. 2018), p. 022341. DOI: `10.1103/PhysRevA.97.022341`.

[66] Wim Bogaerts and Lukas Chrostowski. “Silicon Photonics Circuit Design: Methods, Tools and Challenges”. In: *Laser & Photonics Reviews* 12.4 (2018), p. 1700237. DOI: `https://doi.org/10.1002/lpor.201700237`.

[67] M. Kamandar Dezfouli et al. “Heisenberg treatment of pair generation in lossy coupled-cavity systems”. In: *Phys. Rev. A* 90 (4 Oct. 2014), p. 043832. DOI: `10.1103/PhysRevA.90.043832`.

[68] J.H. Eberly. “Schmidt analysis of pure-state entanglement”. In: *Laser Phys.* 16 (2006), pp. 921–926. DOI: `https://doi.org/10.1134/S1054660X06060041`.

[69] M. Liscidini, L. G. Helt, and J. E. Sipe. “Asymptotic fields for a Hamiltonian treatment of nonlinear electromagnetic phenomena”. In: *Phys. Rev. A* 85 (1 Jan. 2012), p. 013833. DOI: `10.1103/PhysRevA.85.013833`.

[70] Zhenshan Yang, Marco Liscidini, and J. E. Sipe. “Spontaneous parametric down-conversion in waveguides: A backward Heisenberg picture approach”. In: *Phys. Rev. A* 77 (3 Mar. 2008), p. 033808. DOI: `10.1103/PhysRevA.77.033808`.

[71] T. Onodera et al. “Parametric fluorescence in a sequence of resonators: An analogy with Dicke superradiance”. In: *Phys. Rev. A* 93 (4 Apr. 2016), p. 043837. DOI: `10.1103/PhysRevA.93.043837`.

[72] Milica Banic et al. “Two strategies for modeling nonlinear optics in lossy integrated photonic structures”. In: *Phys. Rev. A* 106 (4 Oct. 2022), p. 043707. DOI: `10.1103/PhysRevA.106.043707`.

[73] Luca Zatti, J. E. Sipe, and Marco Liscidini. “Generation of photon pairs by spontaneous four-wave mixing in linearly uncoupled resonators”. In: *Phys. Rev. A* 107 (1 Jan. 2023), p. 013514. DOI: `10.1103/PhysRevA.107.013514`.

[74] Z. Vernon et al. “Truly unentangled photon pairs without spectral filtering”. In: *Opt. Lett.* 42.18 (Sept. 2017), pp. 3638–3641. DOI: `10.1364/OL.42.003638`.

[75] J. B. Christensen et al. “Engineering spectrally unentangled photon pairs from nonlinear microring resonators by pump manipulation”. In: *Opt. Lett.* 43.4 (Feb. 2018), pp. 859–862. DOI: `10.1364/OL.43.000859`.

[76] M. Sloan et al. “High-gain squeezing in lossy resonators: An asymptotic-field approach”. In: *Phys. Rev. A* 111 (6 June 2025), p. 063502. DOI: `10.1103/PhysRevA.111.063502`. URL: `https://link.aps.org/doi/10.1103/PhysRevA.111.063502`.

[77] Andreas Christ et al. "Probing multimode squeezing with correlation functions". In: *New Journal of Physics* 13.3 (Mar. 2011), p. 033027. DOI: `10.1088/1367-2630/13/3/033027`.

[78] Xi-Lin Wang et al. "Experimental Ten-Photon Entanglement". In: *Phys. Rev. Lett.* 117 (21 Nov. 2016), p. 210502. DOI: `10.1103/PhysRevLett.117.210502`.

[79] Natalia Bruno et al. "Heralded amplification of photonic qubits". In: *Opt. Express* 24.1 (Jan. 2016), pp. 125–133. DOI: `10.1364/OE.24.000125`.

[80] Xing Ding et al. "On-Demand Single Photons with High Extraction Efficiency and Near-Unity Indistinguishability from a Resonantly Driven Quantum Dot in a Micropillar". In: *Phys. Rev. Lett.* 116 (2 Jan. 2016), p. 020401. DOI: `10.1103/PhysRevLett.116.020401`.

[81] Alessia Stefano, Luca Zatti, and Marco Liscidini. "Broadband spontaneous parametric downconversion in reconfigurable poled linearly uncoupled resonators". In: *Opt. Lett.* 49.17 (Sept. 2024), pp. 4819–4822. DOI: `10.1364/OL.533455`.

[82] Z. Vernon, M. Liscidini, and J. E. Sipe. "No free lunch: the trade-off between heralding rate and efficiency in microresonator-based heralded single photon sources". In: *Opt. Lett.* 41.4 (Feb. 2016), pp. 788–791. DOI: `10.1364/OL.41.000788`.

[83] Evan Meyer-Scott et al. "Limits on the heralding efficiencies and spectral purities of spectrally filtered single photons from photon-pair sources". In: *Phys. Rev. A* 95 (6 June 2017), p. 061803. DOI: `10.1103/PhysRevA.95.061803`.

[84] Bin Fang et al. "State engineering of photon pairs produced through dual-pump spontaneous four-wave mixing". In: *Opt. Express* 21.3 (Feb. 2013), pp. 2707–2717. DOI: `10.1364/OE.21.002707`.

[85] Ben M. Burridge et al. "Integrate and scale: a source of spectrally separable photon pairs". In: *Optica* 10.11 (Nov. 2023), pp. 1471–1477. DOI: `10.1364/OPTICA.491965`.

[86] Yingwen Liu et al. "High-spectral-purity photon generation from a dual-interferometer-coupled silicon microring". In: *Opt. Lett.* 45.1 (Jan. 2020), pp. 73–76. DOI: `10.1364/OL.45.000073`.

[87] J.M. Arrazola et al. "Quantum circuits with many photons on a programmable nanophotonic chip." In: *Nature* 591 (2021), pp. 54–60. DOI: `10.1038/s41586-021-03202-1`.

[88] H. Seifoory et al. "Degenerate squeezing in a dual-pumped integrated microresonator: Parasitic processes and their suppression". In: *Phys. Rev. A* 105 (3 Mar. 2022), p. 033524. DOI: `10.1103/PhysRevA.105.033524`.

[89] Marc M. Dignam and Marco Liscidini. “Modeling and optimization of pulsed-squeezed-state generation in a ring-resonator system”. In: *Phys. Rev. A* 112 (1 July 2025), p. 013710. DOI: `10.1103/f2y1-scgw`.

[90] Colin Vendromin and Marc M. Dignam. “Optimization of a lossy microring resonator system for the generation of quadrature-squeezed states”. In: *Phys. Rev. A* 102 (2 Aug. 2020), p. 023705. DOI: `10.1103/PhysRevA.102.023705`.

[91] Federico Andrea Sabattoli et al. “Suppression of Parasitic Nonlinear Processes in Spontaneous Four-Wave Mixing with Linearly Uncoupled Resonators”. In: *Phys. Rev. Lett.* 127 (3 July 2021), p. 033901. DOI: `10.1103/PhysRevLett.127.033901`.

[92] Alexander E. Ulanov et al. “Quadrature squeezing in a nanophotonic microresonator”. In: *arXiv preprint* (2025). arXiv: `2502.17337`. URL: `https://arxiv.org/abs/2502.17337`.

[93] Y. Long and J. Wang. “Optically-controlled extinction ratio and Q-factor tunable silicon microring resonators based on optical forces.” In: *Sci Rep* 4 (2014), p. 5409. DOI: `https://doi.org/10.1038/srep05409`.

[94] Y. Henry Wen et al. “All-Optical Control of an Individual Resonance in a Silicon Microresonator”. In: *Phys. Rev. Lett.* 108 (22 June 2012), p. 223907. DOI: `10.1103/PhysRevLett.108.223907`.

[95] Sasikanth Manipatruni et al. “High-speed electro-optic control of the optical quality factor of a silicon microcavity”. In: *Opt. Lett.* 33.15 (Aug. 2008), pp. 1644–1646. DOI: `10.1364/OL.33.001644`.

[96] Long Chen, Nicolás Sherwood-Droz, and Michal Lipson. “Compact bandwidth-tunable microring resonators”. In: *Opt. Lett.* 32.22 (Nov. 2007), pp. 3361–3363. DOI: `10.1364/OL.32.003361`.

[97] Cale M. Gentry et al. “Tailoring of Individual Photon Lifetimes as a Degree of Freedom in Resonant Quantum Photonic Sources”. In: *Conference on Lasers and Electro-Optics.* Optica Publishing Group, 2016, JTu5A.17. URL: `https://opg.optica.org/abstract.cfm?URI=CLEO_SI-2016-JTu5A.17`.

[98] Hossam Shoman et al. “Compact wavelength- and bandwidth-tunable microring modulator”. In: *Opt. Express* 27.19 (Sept. 2019), pp. 26661–26675. DOI: `10.1364/OE.27.026661`.

[99] Paula L. Pagano et al. “Selective Linewidth Control in a Micro-Resonator With a Resonant Interferometric Coupler”. In: *Journal of Lightwave Technology* 43.12 (2025), pp. 5731–5737. DOI: `10.1109/JLT.2025.3552182`.

[100] Michele Midrio et al. “Graphene–assisted critically–coupled optical ring modulator”. In: *Opt. Express* 20.21 (Oct. 2012), pp. 23144–23155. DOI: `10.1364/OE.20.023144`.

[101] Massimo Borghi et al. “Uncorrelated photon pair generation from an integrated silicon nitride resonator measured by time-resolved coincidence detection”. In: *Opt. Lett.* 49.14 (July 2024), pp. 3966–3969. DOI: `10.1364/OL.527965`.

[102] Alice Viola, Francesco Malaspina, and Marco Liscidini. “Squeezing enhancement by suppression of noise through a resonant interferometric coupler”. In: *Opt. Lett.* 49.19 (Oct. 2024), pp. 5611–5614. DOI: `10.1364/OL.532868`.

[103] Alice Viola et al. “Tailoring Spontaneous Four-Wave Mixing in a Ring Resonator with a Resonant Interferometric Coupler”. In: *2025 25th Anniversary International Conference on Transparent Optical Networks (ICTON)*. 2025, pp. 1–4. DOI: `10.1109/ICTON67126.2025.11125148`.

[104] Haoyang Wang et al. “Progress on Chip-Based Spontaneous Four-Wave Mixing Quantum Light Sources”. In: *Advanced Devices & Instrumentation* 5 (2024), p. 0032. DOI: `10.34133/adi.0032`.

[105] Galan Moody et al. “Chip-scale nonlinear photonics for quantum light generation”. In: *AVS Quantum Science* 2.4 (Oct. 2020), p. 041702. DOI: `10.1116/5.0020684`.

[106] Yuqing Jiao et al. “Indium Phosphide Membrane Nanophotonic Integrated Circuits on Silicon”. In: *physica status solidi (a)* 217.3 (2020), p. 1900606. DOI: `https://doi.org/10.1002/pssa.201900606`.

[107] M.A. Butt, B. Janaszek, and R. Piramidowicz. “Lighting the way forward: The bright future of photonic integrated circuits”. In: *Sensors International* 6 (2025), p. 100326. DOI: `https://doi.org/10.1016/j.sintl.2025.100326`.

[108] Houssein El Dirani et al. “Ultralow-loss tightly confining Si3N4 waveguides and high-Q microresonators”. In: *Opt. Express* 27.21 (Oct. 2019), pp. 30726–30740. DOI: `10.1364/OE.27.030726`.

[109] Nathalie Vermeulen et al. “Post-2000 nonlinear optical materials and measurements: data tables and best practices”. In: *Journal of Physics: Photonics* 5.3 (May 2023), p. 035001. DOI: `10.1088/2515-7647/ac9e2f`.

[110] Radhakant Singh et al. “Sputtered aluminum nitride waveguides for the telecommunication spectrum with less than 0.16 dB/cm propagation loss”. In: *Opt. Express* 32.26 (Dec. 2024), pp. 46522–46528. DOI: `10.1364/OE.538852`.

[111] Shiyang Zhu et al. “Aluminum Nitride Ultralow Loss Waveguides and Push-Pull Electro-Optic Modulators for Near Infrared and Visible Integrated Photonics”. In: *2019 Optical Fiber Communications Conference and Exhibition (OFC)*. 2019, pp. 1–3. URL: `https://ieeexplore.ieee.org/document/8696788`.

[112] Rui M. R. Pinto et al. “CMOS-Integrated Aluminum Nitride MEMS: A Review”. In: *Journal of Microelectromechanical Systems* 31.4 (2022), pp. 500–523. DOI: `10.1109/JMEMS.2022.3172766`.

[113] Debin Meng et al. “Kerr nonlinearity in TE/TM microring resonators on cubic silicon carbide-on-insulator platforms”. In: *Applied Physics Letters* 125.25 (Dec. 2024), p. 251106. DOI: `10.1063/5.0221324`.

[114] Peng Xing et al. “CMOS-Compatible PECVD Silicon Carbide Platform for Linear and Nonlinear Optics”. In: *ACS Photonics* 6.5 (2019), pp. 1162–1167. DOI: `10.1021/acsphotonics.8b01468`.

[115] F Smektala et al. “Chalcogenide glasses with large non-linear refractive indices”. In: *Journal of Non-Crystalline Solids* 239.1 (1998), pp. 139–142. DOI: `https://doi.org/10.1016/S0022-3093(98)00730-3`.

[116] M. Garrett et al. “Integrated microwave photonic notch filter using a heterogeneously integrated Brillouin and active-silicon photonic circuit”. In: *Nat Commun* 14 (2023), p. 7544. DOI: `10.1038/s41467-023-43404-x`.

[117] M. Heuck et al. “Heterodyne pump probe measurements of nonlinear dynamics in an indium phosphide photonic crystal cavity”. In: *Applied Physics Letters* 103.18 (Nov. 2013), p. 181120. DOI: `10.1063/1.4828355`.

[118] Domenico D’Agostino et al. “Low-loss passive waveguides in a generic InP foundry process via local diffusion of zinc”. In: *Opt. Express* 23.19 (Sept. 2015), pp. 25143–25157. DOI: `10.1364/OE.23.025143`.

[119] Anagha Kamath et al. “Controlled integration of InP nanoislands with CMOS-compatible Si using nanoheteroepitaxy approach”. In: *Materials Science in Semiconductor Processing* 182 (2024), p. 108585. DOI: `https://doi.org/10.1016/j.mssp.2024.108585`.

[120] K. Ooi et al. “Pushing the limits of CMOS optical parametric amplifiers with USRN:Si7N3 above the two-photon absorption edge”. In: *Nat Commun* 8 (2017), p. 13878. DOI: `https://doi.org/10.1038/ncomms13878`.

[121] Gustavo Grinblat et al. “Ultrafast sub–30-fs all-optical switching based on gallium phosphide”. In: *Science Advances* 5.6 (2019), eaaw3262. DOI: `10.1126/sciadv.aaw3262`.

[122] J. M. Chavez Boggio et al. “Dispersion engineered silicon nitride waveguides by geometrical and refractive-index optimization”. In: *J. Opt. Soc. Am. B* 31.11 (Nov. 2014), pp. 2846–2857. DOI: `10.1364/JOSAB.31.002846`.

[123] Lewis Hill et al. “Effects of self- and cross-phase modulation on the spontaneous symmetry breaking of light in ring resonators”. In: *Phys. Rev. A* 101 (1 Jan. 2020), p. 013823. DOI: `10.1103/PhysRevA.101.013823`.

[124] Johann Riemensberger et al. “Dispersion engineering of thick high-Q silicon nitride ring-resonators via atomic layer deposition”. In: *Opt. Express* 20.25 (Dec. 2012), pp. 27661–27669. DOI: `10.1364/OE.20.027661`.

[125] Herbert R. Philipp. “Optical Properties of Silicon Nitride”. In: *Journal of The Electrochemical Society* 120.2 (Feb. 1973), p. 295. DOI: `10.1149/1.2403440`.

[126] H. R. Philipp. “Silicon dioxide (SiO_2) glass”. In: *Handbook of Optical Constants of Solids*. Ed. by E. D. Palik. Vol. I. Academic Press, 1997, pp. 749–763.

[127] Xingchen Ji et al. “Methods to achieve ultra-high quality factor silicon nitride resonators”. In: *APL Photonics* 6.7 (July 2021), p. 071101. DOI: `10.1063/5.0057881`.

[128] Samantha Roberts et al. “Measurements and Modeling of Atomic-Scale Sidewall Roughness and Losses in Integrated Photonic Devices”. In: *Advanced Optical Materials* 10.18 (2022), p. 2102073. DOI: `https://doi.org/10.1002/adom.202102073`.

[129] Christopher G. Poulton et al. “Radiation Modes and Roughness Loss in High Index-Contrast Waveguides”. In: *IEEE Journal of Selected Topics in Quantum Electronics* 12.6 (2006), pp. 1306–1321. DOI: `10.1109/JSTQE.2006.881648`.

[130] Brent E. Little, Juha-Pekka Laine, and Sai T. Chu. “Surface-roughness-induced contradirectional coupling in ring and disk resonators”. In: *Opt. Lett.* 22.1 (Jan. 1997), pp. 4–6. DOI: `10.1364/OL.22.000004`.

[131] V. Shahraam Afshar, T. M. Monro, and C. Martijn de Sterke. “Understanding the contribution of mode area and slow light to the effective Kerr nonlinearity of waveguides”. In: *Opt. Express* 21.15 (July 2013), pp. 18558–18571. DOI: `10.1364/OE.21.018558`.

[132] Chia Wei Hsu et al. “Bound states in the continuum”. In: *Nature Reviews Materials* 1 (2016), p. 16048. DOI: `10.1038/natrevmats.2016.48`.

[133] Shereena Joseph et al. “Bound states in the continuum in resonant nanostructures: an overview of engineered materials for tailored applications”. In: *Nanophotonics* 10.17 (2021), pp. 4175–4207. DOI: `10.1515/nanoph-2021-0387`.

[134] Chia Wei Hsu et al. “Observation of trapped light within the radiation continuum”. In: *Nature* 499 (2013), pp. 188–191. DOI: `10.1038/nature12289`.

[135] H. Friedrich and D. Wintgen. “Interfering resonances and bound states in the continuum”. In: *Physical Review A* 32 (1985), pp. 3231–3242. DOI: `10.1103/PhysRevA.32.3231`.

[136] J. von Neumann and E. Wigner. “Über merkwürdige diskrete Eigenwerte”. In: *Physikalische Zeitschrift* 30 (1929), pp. 465–467.

[137] Nikola Prodanović et al. “Bound states in continuum: Quantum dots in a quantum well”. In: *Physics Letters A* 377.34 (2013), pp. 2177–2181. DOI: `https://doi.org/10.1016/j.physleta.2013.05.051`.

[138] Yaroslav V. Kartashov, Vladimir V. Konotop, and Lluis Torner. “Bound states in the continuum in spin-orbit-coupled atomic systems”. In: *Phys. Rev. A* 96 (3 Sept. 2017), p. 033619. DOI: `10.1103/PhysRevA.96.033619`.

[139] Nguyen Ha My Dang et al. “Realization of Polaritonic Topological Charge at Room Temperature Using Polariton Bound States in the Continuum from Perovskite Metasurface”. In: *Advanced Optical Materials* 10.6 (2022), p. 2102386. DOI: `https://doi.org/10.1002/adom.202102386`.

[140] Ashok Kodigala et al. “Lasing action from photonic bound states in continuum”. In: *Nature* 541 (2017), pp. 196–199. DOI: `10.1038/nature20799`.

[141] V. Ardizzone et al. “Polariton Bose–Einstein condensate from a bound state in the continuum”. In: *Nature* 605 (2022), pp. 447–452. DOI: `https://doi.org/10.1038/s41586-022-04583-7`.

[142] Filiz Yesilkoy et al. “Ultrasensitive hyperspectral imaging and biodetection enabled by dielectric metasurfaces”. In: *Nature Photonics* 13 (2019), pp. 390–396. DOI: `10.1038/s41566-019-0394-6`.

[143] E. Maggiolini et al. “Strongly enhanced light–matter coupling of monolayer WS2 from a bound state in the continuum”. In: *Nat. Mater.* 22 (2023), pp. 964–969. DOI: `https://doi.org/10.1038/s41563-023-01562-9`.

[144] Luca Carletti et al. “Giant Nonlinear Response at the Nanoscale Driven by Bound States in the Continuum”. In: *Phys. Rev. Lett.* 121 (3 July 2018), p. 033903. DOI: `10.1103/PhysRevLett.121.033903`.

[145] Kirill Koshelev et al. “Nonlinear metasurfaces governed by bound states in the continuum”. In: *ACS Photonics* 6 (2019), pp. 1639–1644. DOI: `10.1021/acsphotonics.9b00700`.

[146] Momchil Minkov, Dario Gerace, and Shanhui Fan. "Doubly resonant χ(2) nonlinear photonic crystal cavity based on a bound state in the continuum". In: *Optica* 6.8 (Aug. 2019), pp. 1039–1045. DOI: `10.1364/OPTICA.6.001039`.

[147] Zhenning Yu et al. "Photonic integrated circuits with bound states in the continuum". In: *Optica* 6 (2019), pp. 1342–1348. DOI: `10.1364/OPTICA.6.001342`.

[148] Vincenzo Macrì, Alice Viola, and Marco Liscidini. "Asymptotic-field approach for the control of dipole emission in integrated structures". In: *Phys. Rev. A* 112 (4 Oct. 2025), p. 043527. DOI: `10.1103/8fbs-z1sv`.

[149] Nir Rotenberg et al. "Small slot waveguide rings for on-chip quantum optical circuits". In: *Opt. Express* 25.5 (Mar. 2017), pp. 5397–5414. DOI: `10.1364/OE.25.005397`. URL: `https://opg.optica.org/oe/abstract.cfm?URI=oe-25-5-5397`.

[150] Łukasz Dusanowski et al. "Purcell-Enhanced and Indistinguishable Single-Photon Generation from Quantum Dots Coupled to On-Chip Integrated Ring Resonators". In: *Nano Letters* 20.9 (2020), pp. 6357–6363. DOI: `10.1021/acs.nanolett.0c01771`.

[151] D Stucki et al. "High rate, long-distance quantum key distribution over 250 km of ultra low loss fibres". In: *New Journal of Physics* 11.7 (July 2009), p. 075003. DOI: `10.1088/1367-2630/11/7/075003`.

[152] I. Aharonovich, D. Englund, and M. Toth. "Solid-state single-photon emitters. Nature Photon". In: *Nature Nanotech* 10 (2016), pp. 631–641. DOI: `https://doi.org/10.1038/nphoton.2016.186`.

[153] C. Couteau et al. "Applications of single photons in quantum metrology, biology and the foundations of quantum physics." In: *Nat Rev Phys* 5 (2023), pp. 354–363. DOI: `https://doi.org/10.1038/s42254-023-00589-w`.

[154] P. Senellart, G. Solomon, and A. White. "High-performance semiconductor quantum-dot single-photon sources". In: *Nature Nanotech* 12 (2017), pp. 1026–1039. DOI: `https://doi.org/10.1038/nnano.2017.218`.

[155] Andreas Reiserer and Gerhard Rempe. "Cavity-based quantum networks with single atoms and optical photons". In: *Rev. Mod. Phys.* 87 (4 Dec. 2015), pp. 1379–1418. DOI: `10.1103/RevModPhys.87.1379`. URL: `https://link.aps.org/doi/10.1103/RevModPhys.87.1379`.

[156] Peter Lodahl, Sahand Mahmoodian, and Søren Stobbe. "Interfacing single photons and single quantum dots with photonic nanostructures". In: *Rev. Mod. Phys.* 87 (2 May 2015), pp. 347–400. DOI: `10.1103/RevModPhys.87.347`. URL: `https://link.aps.org/doi/10.1103/RevModPhys.87.347`.

[157] C. Santori et al. “Indistinguishable photons from a single-photon device”. In: *Nature* 419 (2002), pp. 594–597. DOI: `https://doi.org/10.1038/nature01086`.

[158] D. P. Fussell and M. M. Dignam. “Quasimode-projection approach to quantum-dot–photon interactions in photonic-crystal-slab coupled-cavity systems”. In: *Phys. Rev. A* 77 (5 May 2008), p. 053805. DOI: `10.1103/PhysRevA.77.053805`.

[159] Y. Zhu et al. “A hybrid single quantum dot coupled cavity on a CMOS-compatible SiC photonic chip for Purcell-enhanced deterministic single-photon emission”. In: *Light Sci Appl* 14 (2025), p. 86. DOI: `https://doi.org/10.1038/s41377-024-01676-y`.

[160] M. Davanco et al. “Heterogeneous integration for on-chip quantum photonic circuits with single quantum dot devices”. In: *Nat Commun* 8 (2017), p. 889. DOI: `https://doi.org/10.1038/s41467-017-00987-6`.

[161] Lei Tang et al. “On-chip chiral single-photon interface: Isolation and unidirectional emission”. In: *Phys. Rev. A* 99 (4 Apr. 2019), p. 043833. DOI: `10.1103/PhysRevA.99.043833`.

[162] T. Malhotra et al. “Quasinormal mode theory and design of on-chip single photon emitters in photonic crystal coupled-cavity waveguides”. In: *Opt. Express* 24.12 (June 2016), pp. 13574–13583. DOI: `10.1364/OE.24.013574`.

[163] Peijun Yao and S. Hughes. “Controlled cavity QED and single-photon emission using a photonic-crystal waveguide cavity system”. In: *Phys. Rev. B* 80 (16 Oct. 2009), p. 165128. DOI: `10.1103/PhysRevB.80.165128`.

[164] Sofia Arranz Regidor et al. “Modeling quantum light-matter interactions in waveguide QED with retardation, nonlinear interactions, and a time-delayed feedback: Matrix product states versus a space-discretized waveguide model”. In: *Phys. Rev. Res.* 3 (2 Apr. 2021), p. 023030. DOI: `10.1103/PhysRevResearch.3.023030`.

[165] Will McCutcheon. “Backscattering in nonlinear microring resonators via a Gaussian treatment of coupled cavity modes”. In: *APL Photonics* 6.6 (June 2021), p. 066103. DOI: `10.1063/5.0044059`.

[166] Jia-Sheng Li et al. “Effect of Quantum Dot Scattering and Absorption on the Optical Performance of White Light-Emitting Diodes”. In: *IEEE Transactions on Electron Devices* 65.7 (2018), pp. 2877–2884. DOI: `10.1109/TED.2018.2830798`.

[167] Amir Arbabi et al. “Realization of a narrowband single wavelength microring mirror”. In: *Applied Physics Letters* 99.9 (Aug. 2011), p. 091105. DOI: `10.1063/1.3633111`.

[168] M. M. Dignam et al. “Spontaneous Emission Suppression via Quantum Path Interference in Coupled Microcavities”. In: *Phys. Rev. Lett.* 96 (10 Mar. 2006), p. 103902. DOI: `10.1103/PhysRevLett.96.103902`.